Optical Spectroscopy of Single Non-Polar InGaN Quantum Dots

Claudius C. Kocher

St. Hilda's College

University of Oxford

A thesis submitted for the degree of

Doctor of Philosophy

Hilary Term 2020

Abstract

Experimental investigations of single InGaN/GaN quantum dots grown on the non-polar $(11\bar{2}0)$ plane are presented.

The electrical driving of non-polar nitride quantum dots is demonstrated. Correlation measurements on a single dot prove single-photon emission with a second order correlation value of $g^2(0) = 0.18(18)$, taking into account the detector time response. The dot's emission exhibits a high degree of linear polarisation, in agreement with a study on 76 randomly chosen quantum dots. Current-dependent measurements reveal three biexciton-exciton pairs with a small binding energy of ± 3 meV, indicating dot heights below 5 nm. Electroluminescence of a single dot is demonstrated up to 130 K.

A lateral electric field is applied to quantum dots with the aim of estimating their lateral size and confining potential from linewidth broadening. A measurement on a single dot yields 6(1) nm and 28(3) meV. However, 60 other emission lines do not show a broadening, but their energy shifts allow to determine the magnitude of the in-built dipoles. As expected, these are small compared to those of polar InGaN dots, ranging between $-0.4\,$eÅ and $+0.3\,$eÅ. The existence of both parallel and anti-parallel dipoles is attributed to competition between the first and second order piezo-electric component. A mean in-built field of -3 kV/cm with a standard deviation of 11 kV/cm is deduced, demonstrating a reduction by more than two orders of magnitude compared to polar InGaN dots. Further observations are unexpected non-parabolic energy shifts, attributed to device fabrication issues, and similar shift behaviour of some emission lines in the same spectrum, attributed to multi-excitonic complexes and excited states.

A correlation method is used along with continuous laser excitation to measure the fast timescale of spectral diffusion of several dots. Only a part of a dot's linewidth is selected. One randomly chosen dot exhibits a spectral diffusion time of 860(160) ns at low excitation power. The inverse of the spectral diffusion time increases with increasing excitation power, in line with previous reports. Other quantum dots exhibit shorter, but also longer spectral diffusion times, up to 1170(50) ns. This is at least 3.5 times longer than for any previous measurement on a nitride dot.

To my grandmother Erika.

Acknowledgements

Firstly, I would like to express my gratitude to my supervisor Professor Robert A. Taylor. He was always very supporting, enthusiastic and quick at hand with a magic touch or good advice throughout the PhD. His admirable patience and good humour made working with him also enjoyable on a personal level. He allowed me great liberties in the planing of experiments. I also would like to thank him for reviewing this manuscript.

Second in command as postdoc, Dr Tim Puchtler went along all the way with thoughtful suggestions, ultra steady hands and helpful discussions. I will miss our inspiring after-pub talks when ideas were blooming in such large numbers we could not remember a single one the next day. Many thanks also to Tong, Stephen, Luke and the rest of the research group for a good time in the department and all the White Russians. I owe gratitude to my collaborators in Cambridge: Professor Oliver Rachel for her quick, thorough feedback, Dr Tongtong Zhu for the growing of samples and John Jarman for the fabrication of numerous kinds of devices. Many thanks to Luke and Florian for their knowledgable help on Labview and Phython problems. I was also very lucky to get the chance to learn some metal machining under the strict eyes of Matt in the student workshop, and get a quick helping hand from him and other metal workshop colleagues for the odd hole in an adapter plate.

I also would like to thank for a joint scholarship offered by the Clarendon Fund, the Oxford-Mary Frances and Philip Wagley fund and the Engineering and Physical Sciences Research Council, which enabled me to take up this DPhil position.

I would like to thank my friends and family who helped me along the way. In particular, my friend of the first Oxford (hostel) hour Pankaj, thank you for all the warm and reassuring lunch talks. Poojan, your flaming enthusiastic zeal is still inspiring me. Nipho, it was so good to have a rant together and a beer afterwards. Steve, thanks a lot for your thorough reading of this alien nonsense. Uncle Peter, thank you for your support with some electrical circuits. I also really need to thank my parents Dagmar-Maria and Thomas for their continued support which helped me along this way. Dear granny Erika, thank you for your care packets which regularly lifted up more than just my mood. Last but not least, I am indebted to my partner Rita for her continuous support and encouragement, particularly through the more difficult times of the PhD.

Commonly Used Abbreviations

AFM	Atomic force microscope
CCD	Charge-coupled device
CW	Continuous wave
EL	Electroluminescence
ELOG	Epitaxial lateral overgrowth
FSS	Fine structure splitting
MDE	Modified droplet epitaxy
PL	Photoluminescence
μPL	Micro-photoluminescence
FWHM	Full width at half maximum
HBT	Hanbury Brown and Twiss
IRF	Instrument response function
NA	Numerical aperture
PMT	Photomultiplier tube
Q2T	Quasi-two temperature (growth)
QCSE	Quantum confined Stark effect
QD	Quantum dot
QKD	Quantum key distribution
QW	Quantum well
TCSPC	Time-correlated single photon counting

List of Publications

B. P. L. Reid, C. C. Kocher, T. Zhu, F. Oehler, C. C. S. Chan, R. A. Oliver, and R. A. Taylor, "Non-polar InGaN quantum dot emission with crystal-axis oriented linear polarization" Appl. Phys. Lett. **106**, 171108, (2015).

C. C. Kocher, T. J. Puchtler, J. C. Jarman, T. Zhu, T. Wang, L. Nuttall, R. A. Oliver, and R. A. Taylor, "Highly polarized electrically driven single-photon emission from a non-polar InGaN quantum dot" Appl. Phys. Lett. **111**, 251108 (2017).

T. Wang, T. J. Puchtler, T. Zhu, J. C. Jarman, C. C. Kocher, R. A. Oliver, and R. A. Taylor, "Temperature-dependent fine structure splitting in InGaN quantum dots" Appl. Phys. Lett. **111**, 053101 (2017).

M. Li, F. Chen, C. C. Kocher, H. Zhang, S. Li, F. Huang, J. Zhang, and R. A. Taylor, "Near-Strain-Free GaN/AlGaN Narrow Line Width UV Light Emission with Very Stable Wavelength on Excitation Power by Using Superlattices" ACS Appl. Electron. Mater. **2**, 571-579 (2020).

Y. Park, A. Jana, C. W. Myung, T. Yoon, G. Lee, C. C. Kocher, G. Ying, V. Osokin, R. A. Taylor, and K. S. Kim, "Enhanced photoluminescence quantum yield of $MAPbBr_3$ nanocrystals by passivation using graphene" Nano Res. **12** (2020).

Y. Park, G. Ying, A. Jana, V. Osokin, C. Kocher, T. Farrow, R. Taylor, and K. Kim, "Coarse and fine-tuning of lasing transverse electromagnetic modes in coupled all-inorganic perovskite quantum dots", submitted to ACS Photonics.

C. C. Kocher, J. C. Jarman, T. Zhu, R. A. Oliver, and R. A. Taylor, "Decreased fast spectral diffusion of non-polar InGaN quantum dots", in preparation.

Contents

1 Introduction

Rapid advances in the growth of semiconductor materials in the 1980s and 1990s made it possible to realise structures akin to the well known particle in a box model. Confining a particle in a potential well leads to the quantisation of its energy levels. For example, solving the Schrödinger equation for a one-dimensional box of length L with infinitely high barriers containing a single particle with the mass m yields the energy levels $E_n = n^2h^2/8mL^2$ with the quantisation number $n \in \mathbb{N}$ [1, p. 89]. Experimentally, a confining potential can be created by enclosing a small semiconductor droplet in a matrix of a second semiconductor with a larger bandgap. In order to achieve the energy level quantisation, the relevant scale of the droplet is given by the de Broglie wavelength of the exciton of the enclosed semiconductor. In most semiconductors, this commonly amounts to a few nanometres [1, p. 334]. Restricting the motion of carriers in one direction yields a quantum well (QW), whereas when it is restricted in all three spatial dimensions, a quantum dot (QD) is obtained. This quantum confinement changes the energy dependence of the density of states (DOS) from a square root dependence for bulk material over a step-like DOS for a QW to a discrete DOS for a QD [1, p. 334]. For this reason, QDs are commonly called artificial atoms. Hence, they can be used to generate single photons within a certain wavelength window.

1.1 Applications of single photons

Single photons are a precious, versatile resource which enables a number of important applications. Perhaps the most prominent of these lies in the field of quantum key distribution (QKD) [2–5]. Using a single photon to encode and transmit information protects it against eavesdropping by universally valid laws of physics instead of relying on computationally hard problems [6, 7]. One example is the seminal BB84 protocol, one of the first QKD protocols, published in 1984 [2]. Information is encoded in the polarisation of single photons in two bases (e.g. horizontal/vertical and $\pm 45^\circ$). The sender (Alice) randomly selects one of the 4 states each time she sends a photon, and the receiver (Bob) detects them, also randomly, in one of the two bases. They then compare the bases they used through an authenticated classical channel, select those results for which they chose the same basis, and use this sequence as a one-time encryption key for a message. Interception (by evil Eve) and subsequent attempts to copy and resend the sequence will result in a drastically increased error rate due to the non-orthogonality of the states, ultimately because of the no-cloning theorem [8]. Alice and Bob can determine the error rate by comparing a part of their one-time key over the classical channel.

Although QKD has been conceptionally demonstrated using single-photon sources based on QDs [9, 10], highly attenuated laser pulses are often employed because of the ease of use [11]. As a result of the Poissonian statistics of laser light, a proportion of pulses contains multiple photons which can lead to information leakage to Eve. It was shown that the use of lower intensity laser decoy states along with higher intensity signal states can circumvent this problem [12, 13]. For example, recently, the transmission of a secure key bit rate of 10 MHz for a 1 GHz clock was demonstrated with a laser through a low 2 dB-loss fibre [14]. The transmission rate was limited by the speed of the various processing units. As 33% of the pulses were empty, and additionally a portion of the non-empty pulses was used for the purpose of security checks, a single-photon source

with a high source efficiency could outperform laser-based QKD up to a few GHz clock rate. The highest source efficiency achieved so far for a QD source was 74% [15].

For quantum communication over longer distances, problems arise caused by inevitable photon losses, since these cannot be compensated by classical amplification due to the no-cloning theorem [8]. Instead, quantum repeaters based on pairs of entangled photons could boost the communication range, though quantum memories would be needed to account for non-idealities, thus increasing the system complexity [16, 17]. Entangled photon pairs could also be used to interconnect multiple nodes, building a quantum internet [18, 19]. This substantially increases the demands on the properties of the single-photon sources: in addition to high single-photon purity, the entanglement between two emitted photons needs to be created. Although this is known to be highly sensitive to environmental changes during the emission process, recently, a 59% efficient source of polarisation-entangled photon pairs was demonstrated with a QD embedded in a bulls-eye cavity [20].

The concept of quantum computing has attracted a great deal of attention in the last decade, as it was shown to be highly advantageous in some important instances, for example in factoring of large numbers [21]. Photons are good candidates for qubits because they can travel long distances with low loss of coherence, and coding can be achieved in several degrees of freedom (e.g. polarisation, phase, time bin or path) [7]. A considerable hurdle to overcome is that the required interaction between qubits is weak in the case of photons. However, linear quantum computing presents a workaround. This combines single-photon inputs with linear passive optics such as beamsplitters, waveplates and phase shifters, and projective measurements [22]. Most implementing protocols are probabilistic in nature. A successful outcome is signalled through the detection of additional ancilla photons [23]. The system requirements are high with regard to the single-photon purity, the detection efficiency and the ability of photons to interfere with each other. For the latter, they need to be identical in all defining properties such as polarisation, wavelength, spatial mode and temporal shape, so that they

are indistinguishable. Estimations of the minimum requirements vary. One publication showed that the product of single-photon source efficiency and detector efficiency should be larger than 2/3 [24], or 0.5 in the case of entangled photons [25], assuming perfect single-photon purity and indistinguishability. Another study estimates that the threshold for performing simple entangling gates lies at 0.9 for the single-photon source efficiency and also the detector efficiency, while the single-photon purity benchmark value should be less than 0.07 [26]. As an example, in 2015, the successful implementation of several quantum protocols was demonstrated with a reconfigurable 6-mode solid state waveguide chip [23].

Before a full-blown quantum computer is achieved, quantum supremacy is likely to be demonstrated with a hardware-limited quantum computer. The so-called boson sampling was proposed to simulate the interference of n photons in a system of an m-mode interferometer ($m < n$) with subsequent measurement of the probabilistic output distribution [27, 28]. This is an example where quantum computing can outperform its classical counterpart given a sufficiently high number of input qubits. A recent boson sampling experiment used 20 single-photon channels obtained from a demultiplexed QD single-photon source feeding into a 60-mode interferometer. Classical prediction of the results already would have required a supercomputer to calculate the probability distribution within a reasonable time [28].

Another application of single-photon sources lies in the field of quantum metrology, focusing on the quantum-aided accuracy enhancement of measurements. For example, when a light source with classical photon statistics is used, the measurement of the absorption of materials is ultimately limited by shot noise. However, photon number states have a well-defined photon number and therefore, due to the Heisenberg uncertainty principle, exhibit a completely uncertain phase. This can be exploited to increase the absorption measurement accuracy below the classical limit for small absorption values. This requires a photon source with high single-photon purity and high single-photon source efficiency [29]. Another example of quantum enhanced sensing is the

increased phase sensitivity in a Mach-Zehnder interferometer employing an entangled NOON state ($|N0\rangle + |0N\rangle$, $n \in \mathbb{N}$). The minimum phase uncertainty is limited by the inverse of the photon number N, thereby beating the classical limit by $1/\sqrt{N}$ [30]. One way to generate NOON states is the interference of a coherent state with a single-photon state [31]. Near-coherent superpositions of Fock-states up to $n = 2$ have recently been generated with a QD source, demonstrating the capability of super-phase-resolution in a Mach-Zehnder interferometer [32].

1.2 Sources of single photons

QDs are not the only means of generating single photons. The process of spontaneous parametric down-conversion of laser light in a non-linear crystal is often used for the generation of entangled photon pairs. Alternatively, if one photon of each pair is detected, a heralded single-photon stream is created. However, the pair generation is random, such that several processes can occur simultaneously, spoiling the single-photon purity and indistinguishability [33]. Consequently, the laser power is usually kept low, and the resulting single-photon source efficiency is therefore also low.

Atoms and ions can naturally emit single photons with good coherence properties and their emission is stable. The emission energy depends on the individual element. However, the deterministic capturing and holding of atoms and ions in an ultra-low vacuum is a challenge. Furthermore, they tend on average to emit photons after a relatively long time, several tens of nanoseconds after excitation, the so-called lifetime, whereas to obtain a high single-photon emission rate, a shorter lifetime is desirable [7].

Emission from defects in solid state materials is a large field, with the prominent examples of SiC [34], ZnO [35], BN [36] and GaN [37]. Possibly the most thoroughly researched defect is the NV colour centre in diamond [38]. Most of the defects yield high emission rates and emit single photons up to room temperature. Their emission energies range between long wavelength visible light [38] and the near infrared [37]. For

the NV defect, emission enhancement through cavities has been demonstrated to mitigate the high refractive index hindering efficient outcoupling [38], as well as enhancing the proportion of photons emitted into the zero-phonon line, a value which for most defects is low due to strong phonon interaction [39–41]. Increasing the proportion of the zero-phonon intensity at the cost of the phonon mediated emission is desirable, since the latter has very poor indistinguishability properties. Most defects have the added drawback of being difficult to generate deterministically, and that electrical excitation for improved applicability is demanding [39].

Another group of single-photon emitters are colloidal QDs. Some are produced with a core-shell structure such as CdSe/ZnS [42] and CdSe/CdS [43]. Others such as lead halide perovskite QDs are not [44]. Their emission energy depends on the size of the particles, but generally lies within the visible range. Electrically excited single-photon emission up to room temperature has been demonstrated [45], as well as strong coupling to a plasmonic cavity [42]. Drawbacks are the relatively long lifetimes of up to tens of nanoseconds limiting the single-photon source efficiency [45] and the strong influence of the electric environment on the emission energy (spectral diffusion), which results in a broad linewidth [46], which would severely limit the indistinguishability.

Among the epitaxially grown QDs, group-III-arsenide dots are currently the most mature, since the material platform has gone through decades of industrial-scale research and development. In terms of single-photon purity [47], single-photon source efficiency [15, 48], indistinguishability [49, 50] and the generation of entangled photon pairs [20], high performance has been achieved, outperforming all other previously mentioned methods of generating single photons. For most of the reports, the QD emission wavelength ranges between 880-960 nm, but efforts are being made to match the low dispersion wavelength window at 1.3 μm, and the low absorption range at 1.55 μm of commercial glass fibres [51, 52]. The main drawback of arsenide QDs is that they rely on cryogenic operation because the confinement potential is relatively shallow and that the exciton binding energies are small such that these are easily exceeded even by

thermal excitations at the liquid nitrogen temperature of 77 K.

1.3 Nitride quantum dots

By contrast, group-III-nitride QDs have the potential to overcome this limitation and operate up to room temperature. This is because of larger band offsets, and larger exciton binding energies due to higher effective masses and lower dielectric constants [53]. Indeed, in the case of a GaN/AlGaN QD, single-photon emission has been demonstrated up to 350 K [54] and up to room temperature in case of an InGaN/GaN QD [55]. Furthermore, electrically excited single-photon emission has been demonstrated with InGaN/GaN QDs [55, 56]. The bandgap of nitride materials ranges from the deep UV with AlN (6.1 eV [57]) over the near UV with GaN (3.4 eV [58]) to the near infra-red with InN (0.7-0.9 eV [59, 60]). Intermediate values can be obtained through tertiary and quaternary compounds. Nitride dots are usually grown in the thermodynamically stable wurtzite phase. This non-centrosymmetric crystal structure gives rise to particularly strong in-built fields across heterostructures, along the crystal axis commonly used as growth direction. This in turn gives rise to the quantum confined Stark effect: the wavefunctions of the electrons and holes become separated by the field, resulting in a large dipole and a reduced emission rate. To mitigate this detrimental effect, efforts have been made to reduce the size of the dots [61, 62]. Another solution is to choose a growth plane perpendicular to the polar crystal plane, as this reduces the area of a QD exposed to the polar direction due to their flat shape (compare with the schematic sketch in Figure 2.3(a)). This approach is adopted in this thesis. Successful growth of InGaN/GaN QDs on non-polar planes led to the demonstration of single-photon emission up to 220 K [63], an increase in the emission rate by a factor of approximately 10 [64], and a strong linear polarisation degree [65, 66]. The latter effect is a consequence of a change in the hole energy level alignment due to anisotropic strain in the growth plane [66].

1.4 Thesis layout

In chapter 2, the particular features of nitride materials are explained in greater detail. Special attention is given to the influence of the quantum confinement and the growth plane on the energy levels, and to the resulting polarisation of the emitted light. In the last section, the second order correlation function is introduced which is used to distinguish between different categories of light, such as single-photon emission.

Chapter 3 is dedicated to the growth methods of the QDs samples used in this thesis, and the optical micro-photoluminescence setup. The considerations behind the setup assembly are explained. The different detection capabilities including spectrally-resolved, polarisation-resolved, time-resolved and second-order correlation function measurements are described in detail. Special attention is given to the newly built telecentric scanning system.

In chapter 4, the first demonstration of electrically excited non-polar InGaN QDs is presented. First, the current dependence of the emitted light is described. This leads to the identification of three biexcitons. The polarisation properties of a large number of QDs is then probed. This is followed by a demonstration of single-photon emission of a single QD at 4.5 K. Finally, the temperature dependence of this QD and a second dot is investigated.

Chapter 5 concentrates on the influence of a lateral electric field on the photoluminescence of single non-polar InGaN QDs. For a majority of dots, systematic shifts of emission lines are observed upon the application of an electric field. Firstly, the influence of the laser power on the energy shift is determined. Secondly, the energy shift of a larger number of QD emission lines is investigated for an electric field both parallel and perpendicular to the polar direction. A group of dots exhibits small dipole moments in comparison to polar InGaN quantum dots, as theoretically expected. The final section focuses on the electric field dependence of multiple emission lines occurring in one spectrum.

Chapter 6 investigates the implications of the reduced dipole moments of non-polar InGaN QDs for the coupling to the electrostatic environment. It is well known that the large dipole moments of conventionally grown nitride dots result along with charge carrier trapping in a linewidth broadening of time-integrated spectra. This process, known as spectral diffusion, crucially limits the attainment of highly indistinguishable photons. Correlation spectroscopy allows to determine the fast timescale of the spectral diffusion, which gives rise to a bunching feature. The excitation power dependence of this effect is investigated for a single QD. The correlation measurement is repeated for several other dots to obtain an overview of the spread of the fast spectral diffusion time.

In chapter 7, the achievements of this thesis are briefly summarised.

2 Properties of group III-nitride semiconductors

2.1 Crystal structure

Here we focus on group III-nitride semiconductors, to which we refer in the following as nitrides. These materials exist either in the thermodynamically metastable cubic zincblende phase or in the stable hexagonal wurtzite phase, which we are interested in as it is much easier to grow [67]. In the following, we restrict the discussion to nitride material grown in the wurtzite phase. In Figure 2.1(a), a unit cell of wurtzite GaN is highlighted. It has an orthorhombic shape, containing alternating layers of tetrahedrally coordinated atoms with an *ABAB* layer stacking. The unit cell parameters are the base lattice parameter a, the base angles of 60° and 120° and the lattice parameter c. The values for the three most common binary nitride materials are given in Table 2.1. Three unit cells combined together form the wurtzite hexagonal structure. In its schematic representation in Figure 2.1(b), the most relevant crystallographic planes and directions for this thesis are shown. They are commonly described by four-index Miller indices. The most important axis is the c-direction $[0001]$.

Examination of the unit cell shows that the barycentres of the N and group-III atoms do not overlap: the crystal structure lacks inversion symmetry. Since the electronegativity of N and group-III elements is different by a large amount, this distorts the sp^3-hybridised bonds, leading to a microscopic dipole along the c-direction and macroscop-

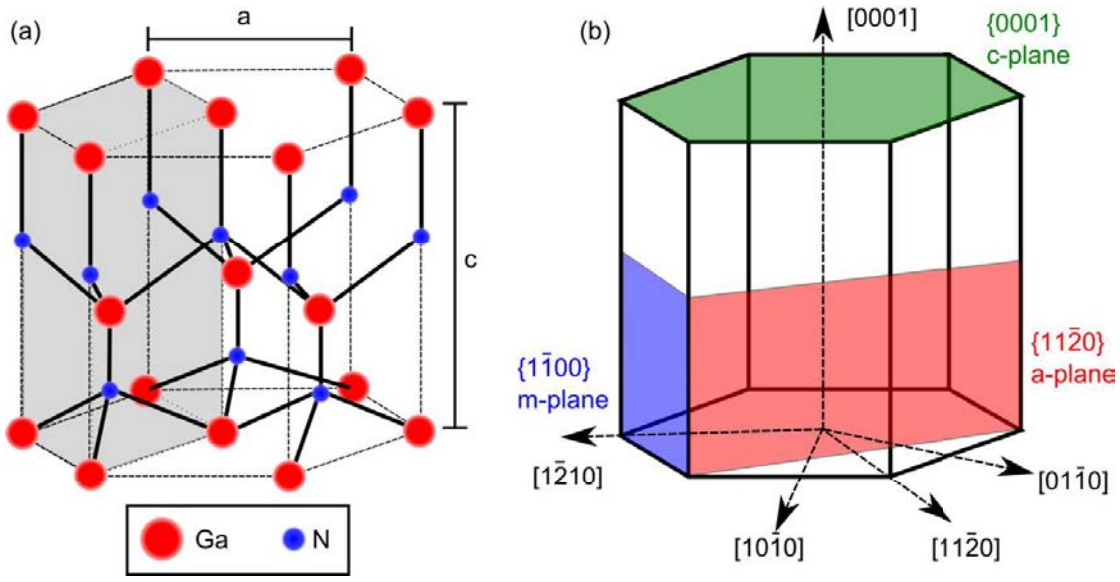

Figure 2.1: (a) A ball-and-sticks visualisation of the crystal structure of wurtzite GaN. The unit cell is highlighted in light grey. (b) Relevant crystallographic planes and directions in wurtzite nitride materials. Adapted from Ref. [68].

ically to an overall polarisation termed spontaneous polarisation [69]. Therefore, the *c*-direction is commonly referred to as a *polar* direction. Perpendicularly to it lie the *non-polar* *a*-direction $[11\bar{2}0]$ and *m*-direction $[1\bar{1}00]$. Additionally to the spontaneous polarisation, strain can cause piezoelectric polarisation by deforming the crystal structure further and changing the position of the N- and group-III-barycentres. The strength of the spontaneous polarisation of GaN is comparable to or larger than those of II-VI compounds. The piezoelectric constants of nitride materials are up to 10 times larger than those of other III-V or II-VI semiconductors [69]. The amount of piezoelectricity

Material	a (Å)	c (Å)
InN	3.545	5.703
GaN	3.189	5.185
AlN	3.112	4.982

Table 2.1: Unit cell parameters of the 3 common binary nitride materials. Adapted from Ref. [70].

generated depends on the amount of strain under which the material is. Since nitride material is commonly grown on sapphire, to which it has a lattice mismatch of up to 13.9% (depending on the growth orientation [71]), strain is commonly present in nitride materials. Therefore, the sum of spontaneous and piezoelectric polarisation can be very large.

2.2 Quantum confined Stark effect

In nitride heterostructures such as InGaN/GaN QWs, the step change in polarisation leads to interface charges. These result in large electric fields due to the large differences in polarisation. Fields thus generated in QWs or QDs can amount to several MV/cm [72–74]. These can significantly impact their emission properties. In particular, these lead to the quantum confined Stark effect (QCSE). It describes the influence of an electric field, be it in-built or externally applied, on the wavefunctions of a quantum confined nanostructure. An electric field tilts the energy levels of holes and electrons, such that these shift in opposite directions and are located in spatially different potential pockets. Consequences are a reduced emission rate since the electron-hole overlap is reduced and a red shift of the emission [75].

The Hamiltonian which describes the influence of an uniform electric field $\mathbf{F}$ on a quantum system can be expressed as the sum of the Hamiltonian for unperturbed system H_0 and the interaction of the electric dipole $\mathbf{p} = q\mathbf{R}$ with the field $H_{\text{tot}} = H_0 - \mathbf{F}\cdot\mathbf{R}q$, where $\mathbb{R}$ is the spatial vector between the charges. For energy shifts small compared to the emission energy, the influence of the electric field can be described by perturbation theory [76]. Therefore, if the unperturbed system has the eigenenergies E_0^n with the corresponding wavefunctions $|n\rangle$, the energy of the perturbed system can be approximated up to second order with the following equation.

$$E^n = E_0 - q\langle n|\mathbf{F}\cdot\mathbf{R}|n\rangle + q^2 \sum_{k\neq n} \frac{|\langle n|\mathbf{F}\cdot\mathbf{R}|k\rangle|^2}{E_0^n - E_0^k} \tag{2.1}$$

Since the expression $\langle n|q\mathbf{R}|n\rangle$ in the first perturbation term is the value of the dipole moment $\mathbf{p}$ of the unperturbed system, commonly called permanent dipole, it is clear that the linear energy shift due to this term is proportional to the projection of the dipole moment onto the direction of the field. If the dipole moment is parallel to the field, the transition energy decreases, whereas it increases when they oppose each other. The proportionality factor of the quadratic term is commonly called the polarisability α. For the system ground state, it can be seen that its sign is negative, since $E_0^1 - E_0^k < 0$. Therefore, this component will lead to a reduced emission energy. With above definitions, Equation (2.1) simplifies such that the energy shift of a system under the influence of an electric field relative to its unperturbed eigenenergy amounts to

$$\Delta E = E^n - E_0 = p_{||}F + \alpha_{||}F^2 \tag{2.2}$$

with the dipole moment component $p_{||}$ and the polarisability $\alpha_{||}$ in the direction of the field.

2.3 Band structure and emission properties

The band structure of nitrides depends significantly on the growth plane and on the degree of confinement. Starting from bulk GaN, we trace the changes over the band structure of GaN QWs to the energy levels of non-polar InGaN QDs. Additionally, the influence of the band or energy level structure on the polarisation of the emission is discussed. Most of the section is based on papers (co-) authored by the theoretical physicist Stefan Schulz.

2.3.1 Bulk

Wurtzite nitrides possess a direct bandgap at the Γ point in k-space. The conduction band is derived from the group-III atoms, which gives it s-like orbital character. The first

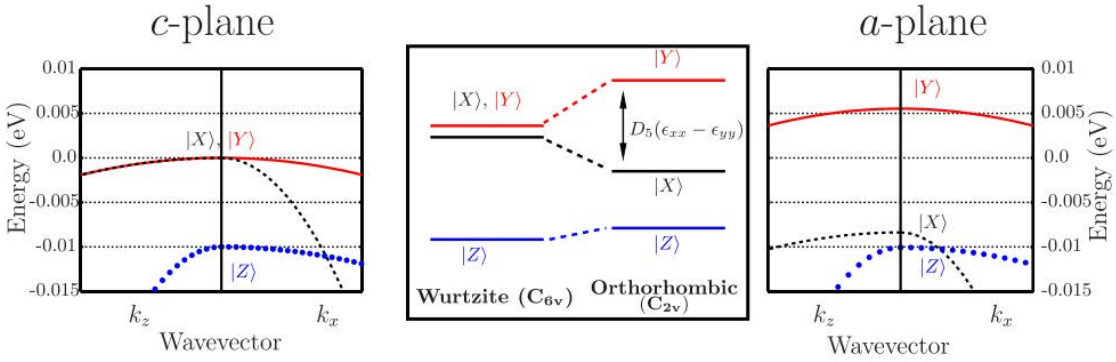

Figure 2.2: Schematic representation of the GaN bulk valence band structure near the Gamma point. (a) *c*-plane GaN without strain or spin-orbit coupling. (b) Schematic difference for the energy spacings at the Γ point for *c*- and *a*-grown GaN with strain. (c) *a*-plane GaN with strain. Adapted from Ref. [77].

3 valence bands however are derived from the N atoms, which gives them *p*-like orbital character [78]. In Figure 2.2(a), the band structure of *c*-plane bulk GaN is schematically shown. The 3 hole bands are not degenerate. The $|Z\rangle$ wavefunction derived from the atomic p_z orbital extending along $[c]$ is the only one influenced by the internal crystal field, which shifts the energy of the orbital to lower energy. The degeneracy of the top two bands is lifted due to spin-orbit coupling (not shown in the schematic). They have $|X \pm iY\rangle$ character[1]. The bands are commonly labelled *A*, *B* and *C* from the top. For unstrained polar GaN the energy splittings are $\Delta E_{AB} \approx 6\,\text{meV}$ and $\Delta E_{BC} \approx 21\,\text{meV}$ [79].

The situation changes when growth on the *a*-plane is considered. Under strain, the crystal structure changes from hexagonal to orthorhombic [77]. Then, the strain in the growth plane and -more importantly- in the *c*-plane is anisotropic. This leads to a larger splitting of the top two valence bands, proportional to the strain difference along $[a]$ and $[m]$. The $|Y\rangle$-like band is lifted in energy and the $|X\rangle$-like band is decreased in energy, see Figure 2.2(b). The top valence states are therefore unmixed into the pure $|X\rangle$, $|Y\rangle$- and $|Z\rangle$-like states.

To infer the degree of polarisation of the emitted light from the band structure, one

[1] In this subsection, we use the coordinate system which is oriented such that z is parallel to c, y to m, x to a, in contrast to later cited papers [66].

needs to consider the relative oscillator strengths. The valence band wave functions $|\Phi_i^{VB}\rangle$ can be given as a linear combination of $|X\rangle$-, $|Y\rangle$-,$|Z\rangle$-like states. Their prefactors c_i^{α} can be found by solving the Schrödinger equation and deconstructing the eigenvectors into the basis states. The optical polarisation selection rules can be determined by calculating the dipole matrix elements $d_{ij} = |\langle\Phi_i^{CB}|\mathbf{e}\cdot\mathbf{p}|\Phi_j^{VB}\rangle|$ with the normalised polarisation vector $\mathbf{e}$. Because the matrix elements $\langle S|p_\alpha|\alpha\rangle,\ \alpha \in \{X,Y,Z\}$ with $|\Phi_i^{VB}\rangle = |S\rangle$ can be taken equal, the relative oscillator strengths are equal to the squared magnitude of the prefactors c_i^{α}. For conventional growth methods, *c*-plane GaN is isotropically compressively strained in the growth plane. In this case, the oscillator strength for the interband transition between the conduction band and topmost valence band is the same for $|X\rangle$- and $|Y\rangle$-like states. Therefore the emission is circularly polarised.

However, conventionally grown *a*-plane GaN exhibits compressive strain in the growth plane, and tensile strain along the growth direction, thereby breaking the symmetry present in *c*-plane grown GaN. The relative oscillator strength of the $|Y\rangle$-like state is then by far the largest contribution to the interband oscillator strength between conduction and top valence band, as one would intuitively expect from the energetically large separation of $|Y\rangle$- and $|Z\rangle$-like band in Figure 2.2(c) [77]. As an example, emission from a 5 μm thick *a*-plane GaN layer grown on an *r*-sapphire substrate showed a degree of linear polarisation (DOLP) of approximately 0.8 [77]. The DOLP is calculated based on the maximum and minimum intensity obtained when rotating a linear polariser and monitoring its transmission [66].

$$DOLP = \frac{I_{\max} - I_{\min}}{I_{\max} + I_{\min}} \tag{2.3}$$

2.3.2 Quantum wells

Considering a QW system instead of a bulk material, the band alignment can be further altered by quantum confinement and additional strain. The former will lead to an en-

hanced separation between the bands as one can intuitively guess from the particle in the box model – the smaller the box, the larger the separation between the energy levels. That means the lowest hole band is further pushed away from the band edge. Therefore, in polar QWs the $|Z\rangle$-like band and in a-plane QWs the $|X\rangle$-like band are irrelevant [77]. A second important effect of the confinement is that bands with larger effective masses are shifted less than those with smaller ones, which is again intuitively clear from the particle in a box model where the energy is inversely proportional to the mass. One must be careful that the energy scale for holes is opposite to that of the electrons. So a shift to higher (hole) energy means a shift to lower (electron) energy in regard to the valence band maximum.

In a c-plane QW, a lateral compressive strain due to growth reduces the $|Z\rangle$-like band in energy further [77]. If the strain is isotropic, the top two bands remain in the $|X \pm iY\rangle$ configuration, leading to unpolarised emission. If it is anisotropic, they unmix such that polarised emission can be observed [80].

In the case of an a-plane QW, the strain along the growth direction is tensile and in the growth plane it is compressive, such that the spacing between the $|Y\rangle$-like state and the $|X\rangle$-like state increases even more [77].

The influence of the spin-orbit coupling on the relative oscillator strengths of transitions in an a-plane QW is interesting. Neglecting it results in a relative oscillator strength of unity for the $|Y\rangle$-like band, independent of strain or confinement effects. For negligible strain and quantum confinement, but finite spin-orbit coupling, the oscillator strengths for both the $|Y\rangle$- and $|Z\rangle$-like band amount to 0.5. The larger the strain and the stronger quantum confinement gets, the more increases the $|Y\rangle$-like band contribution [77]. The DOLP of both a-plane and m-plane InGaN QWs should be identical in theory. However, homoepitaxy on non-polar substrate growth planes results in different strain, such that an average DOLP of 0.7 and 0.9 was found experimentally for a-plane and m-plane InGaN QWs with the same setup, respectively [81]. Additionally, for a-plane InGaN QWs, a dip in the DOLP at higher energy was found, coinciding with a

longer lived component. Its origin is still under question. The hypothesis of indium clustering being the cause of it did not hold as clustering can be also found for higher indium-containing *m*-plane QWs [82].

2.3.3 InGaN quantum dots

In QDs, due to the additional lateral confinement compared to QWs, confinement effects play an even more prominent role, separating the energy levels further compared to QWs. For *c*-plane nitride dots, the top two bands are almost degenerate, therefore a perfectly in-plane centro-symmetric dot would not show linearly polarised, but circularly polarised emission. However, growth is always subject to imperfections (e.g. in the dot shape or the strain field or the indium distribution), such that the confinement potential will be asymmetric. This will lead to a splitting of the two top valence bands and consequently linearly polarised emission, without a fixed polarisation axis relative to the crystal structure [53, 83]. Two groups exploited this effect and intentionally engineered an anisotropic strain environment of *c*-plane InGaN dots through nano-structuring (stretched pyramids, elliptic nanopillars), realising linearly polarised emission aligned approximately along the intended axis with a mean $DOLP = 0.85$ and $DOLP = 0.72$, respectively [84, 85].

For *a*-plane nitride dots, the situation is different, since growth intrinsically leads to anisotropic strain in the *c*-plane, similar to *a*-plane QWs. Additionally, the confinement is stronger than in QWs, so that the first few excited states of InGaN QDs with an indium content of 15-25% are almost entirely $|Y\rangle$-like [66]. The QD shape plays an important role since any shape anisotropy changes the strength of quantum confinement, which in turn causes shifts in the energy of the states. For example, for a lens-shaped InGaN QD with a height of 3 nm and a round base with a diameter of 30 nm, $\mathbf{k}\cdot\mathbf{p}$ calculations yielded a DOLP of 0.96. Reducing the diameter in the *c*-direction increases the DOLP because the energy band of the $|Z\rangle$-like state exhibits in the *c*-direction a lower effective

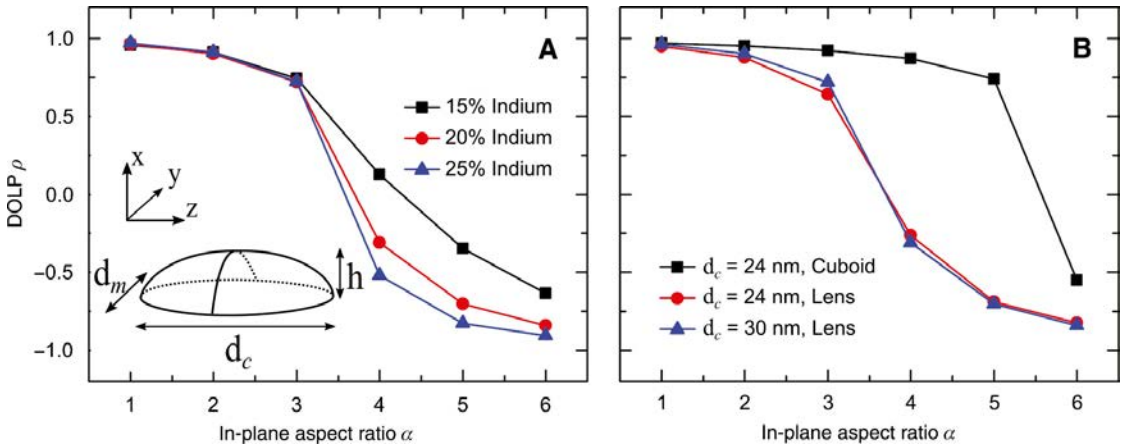

Figure 2.3: (a) Dependence of the calculated DOLP on the in-plane aspect ratio α of a lens-shaped a-plane InGaN QD. The diameter in the c-direction is fixed to $d_c = 30\,\text{nm}$, whereas $d_m = d_c/\alpha$ ranges between 30 nm and 5 nm. The QD height is fixed at 2.5 nm. The inset shows a schematic QD sketch with the coordinate system. (b) Dependence of the calculated DOLP on the in-plane aspect ratio of two lens-shaped dots with $d_c = 30\,\text{nm}$ and $d_c = 24\,\text{nm}$, and a cuboid shaped dot with $d_c = 24\,\text{nm}$. The height was fixed at 2.5 nm and the indium content 20%. Adapted from Ref. [66].

mass than those of the $|Y\rangle$-like state (compare Figure 2.2(c)). Therefore, the energy level of the $|Z\rangle$-like state is more strongly shifted to lower energies with respect to the valence band maximum and the energy distance between these states increases, as it is intuitively clear from the particle in a box model. In contrast, reducing the diameter in the m-direction leads to a reduction of the DOLP, because in this direction the $|Y\rangle$-like state exhibits a lower effective mass than the $|Z\rangle$-like state, therefore reducing the energy spacing between the states [66]. The results of the DOLP calculation are shown in Figure 2.3 as a function of the in-plane aspect ratio $\alpha = d_c/d_m$, with the lengths of the main axes d_i along the i-axis of the elliptic dot base. Panel (a) focuses on different indium contents between 15-25% and a fixed $d_c = 30\,\text{nm}$. Panel (b) compares a cuboid-shaped and a lens-shaped dot with two different fixed d_c. It can be seen that the QD DOLP is relatively robust against small shape anisotropies, different indium content and different sizes. In this study, the DOLP was slightly differently defined than in Equation (2.3): instead of taking the maximum/minimum intensity, the oscillator strength along

fixed axes was used[2]. Therefore, it can reach negative values if the oscillator strength of the $|Z\rangle$-like state becomes dominant. This change of the polarisation direction only occurs for large deformations $\alpha > 3$ for lens-shaped dots and even larger deformations $\alpha > 5$ for cubic QDs.

Experimentally, the very large majority of our *a*-plane InGaN QDs, grown with 2 different methods (see section 3.1), show linearly polarised emission along the *m*-direction, as predicted above, with a high average $DOLP \approx 0.9$ [66, 86].

Fine structure splitting

On a smaller energy scale, there exists another energy splitting regarding the excitonic emission of uncharged QDs: the fine structure splitting (FSS). It is caused by anisotropic electron-hole exchange interaction which can be enhanced through a broken symmetry such as a shape anisotropy. For arsenide dots, this results in two split bright states and two split dark states and changes the emission polarisation from circular to linear, which has been theoretically and experimentally verified. In particular, the lifting of the degenerate energy levels inhibits the generation of polarisation-entangled photon pairs via the biexciton-exciton cascade (a biexciton comprises two holes and two electrons) because the which-path information is given away by the difference in energy [87]. This situation is shown in Figure 2.4.

For *c*-plane nitride dots, group symmetry considerations lead to a wealth of bright levels [88]. Calculations based on a fully atomistic many-body framework including random alloy fluctuations yielded four bright states with the same polarisation properties, where the three lowest states clustered together and the energy separation to the higher state varied between 5 μeV to 25 μeV [53]. Experimentally, the FSS of *c*-plane InGaN QD-like localisations in a InGaN QW could only be observed for sideways collection at 4 K [88]. It varied between 100 μeV and 350 μeV at 5 K. No dependence on the emission energy could be identified, in contrast to arsenide QDs [89]. For *a*-plane

[2] $DOLP = (I_m - I_c)/(I_m + I_c)$

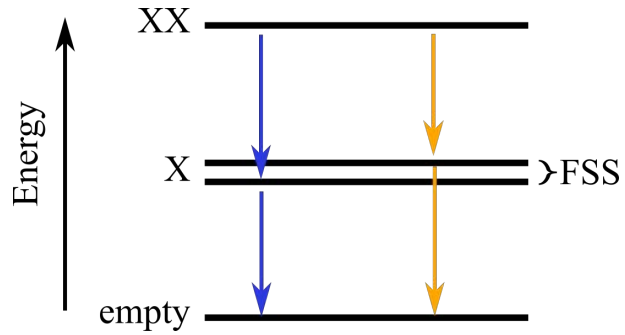

Figure 2.4: Sketch of the biexciton cascade. Emission from biexciton state (XX) to the exciton state (X) will result in two orthogonally linearly polarised (colour-coding) emission lines in the case of a non-negligible FSS common for nitride dots. The emission from the exciton state to an empty dot will also exhibit two linearly polarised lines. The FSS is overstated drastically for clarity's sake.

nitride dots, FSS ranging between 200 μeV and 800 μeV could be observed at 5 K, collecting perpendicular to the surface. Equally, no emission energy dependence was found [65,90]. With rising temperature, the FSS increases up to 10 meV at 200 K, along with the linewidth. So far, no theoretical description of the FSS has been published for non-polar nitride QDs.

The biexciton emission mirrors the FSS of the exciton emission, since the biexcitonic final decay state is the initial state of the exciton emission and the biexcitonic state exhibits no splitting due to pairs of anti-aligned electrons and holes, resulting in a total spin of zero [88]. For a charged QD, the two electrons (or holes) pair usually as well, such that there is no electron-hole interaction in first order. Therefore, one indication of charged QD transitions is the lack of a FSS [91].

2.4 Photon statistics

In order to assess if a source emits single photons, the second order correlation function $g^2(\tau)$ of the source needs to be evaluated. In its classical formulation it describes

correlations in the source intensity $I(t)$ for different delays τ, averaged over the time t.

$$g^2(\tau) = \frac{\langle I(t)I(t+\tau)\rangle}{\langle I(t)\rangle\langle I(t+\tau)\rangle} \tag{2.4}$$

This definition holds for stationary light sources. In general, light sources can be divided into three categories on the basis of the value $g^2(\tau = 0)$. For all of them, $g^2(\tau)$ will approach unity at infinitely long delay times, as light intensity fluctuations will then be uncorrelated. A first category consists of sources with random fluctuations, such as coherent light emitted by lasers well above the threshold. Since they emit photons at random times, the second order correlation function is equal to unity regardless of the delay time. In terms of the fluctuations in the photon number n within regularly spaced time intervals, coherent light sources exhibit Poissonian statistics, such that the standard deviation Δn is equal to their mean photon number $\bar{n}$.

In regard to the second order correlation function, sources with Poissonian statistics are commonly used as a dividing line to distinguish super-Poissonian and sub-Poissonian light sources. An example of the former one is thermal light. A single radiation mode will emit photons according to the Bose-Einstein distribution. Its photon number fluctuation amounts to $\Delta n = \sqrt{\bar{n}^2 + \bar{n}}$, which is larger than for Poissonian sources. The second order correlation function at zero delay computes to $g^2(0) > 1$, which is called bunching[3]. Super-Poissonian and Poissonian behaviour can be explained by classical physics. However, sub-Poissonian emission statistics $\Delta n < \sqrt{\bar{n}}$ are a sign of quantum behaviour [1]. In most cases, sub-Poissonian emission results in anti-bunching $g^2(0) < 1$. In quantum optics, the second order correlation function is redefined in the second quantisation picture and reads for a stationary source

$$g^2(\tau) = \frac{\langle a^\dagger(t)a^\dagger(t+\tau)a(t+\tau)a(t)\rangle}{\langle a^\dagger(t)a(t)\rangle} \tag{2.5}$$

[3]For a time bin $\Delta\tau$ much smaller than the coherence time τ_c of the thermal light source, one obtains $g^2(0) = 2$.

where $a^\dagger$ (a) are the photon creation (annihilation) operators [92]. At zero delay $\tau = 0$ the second order correlation function can be rearranged with the bosonic commutator $[a, a^\dagger] = 1$ in terms of the number operator $n = a^\dagger a$ to yield $g^2(0) = \langle n^2 \rangle - \langle n \rangle / \langle n \rangle^2$. For a Fock state $|n\rangle$ with n photons one obtains the result of $g^2(0) = 1 - 1/n$. This means that a single-photon source can be identified through $g^2(0) = 0$, whereas a twin photon state $|n = 2\rangle$ will yield $g^2(0) = 0.5$. Hence, the presence of single-photon emission is indicated by a measured value of $g^2(0) < 0.5$ [7, 93]. The experimental realisation of the measurement is described in subsection 3.2.6.

3 Samples and experimental setup

3.1 Sample growth

Nitride materials are most commonly grown by metal-organic vapour epitaxy (MOVPE), as opposed to the expensive and slow molecular beam epitaxy or the less accurate hydride vapour phase epitaxy. Conventional epitaxy methods used for the growth of Si or GaAs like the Czochralski or Bridgman growth methods cannot be applied to nitride materials because of their elevated melting temperatures. MOVPE involves epitaxial growth through chemical reactions of precursor gases at elevated temperatures and pressures. The metal-organic precursor gases used for the growth of GaN and InGaN are trimethylgallium ($Ga(CH_3)_3$) and trimethylindium ($In(CH_3)_3$). The source of nitrogen is ammonia (NH_3). The precursors are mixed with non-reacting carrier gases like N_2 and H_2. For doping, appropriate additional precursor gases are added [94].

The fabrications of QDs can be categorized into two main categories: a top-down approach and a bottom-up approach. The former involves the growth of a QW, which is then etched into sub-micron pillars. The pillar size then defines the lateral extent of the QD. This technique has been applied by a few groups to produce InGaN dots [56, 95]. The advantage is the deterministic location, drawbacks are increased fabrication complexity, additional non-radiative recombination centers provided by the sidewalls and that integration into more advanced optical structures such as photonic crystals is difficult. This can be achieved with the bottom-up random dot growth [55, 96]. Another technique consists of predefining masks leading to pillar- or pyramid-growth with the

formation of dots at the top, which may lead to the reduction of the dislocation density close to dots, but has also the aforementioned drawbacks [62, 97, 98].

The samples used in this thesis have been grown with the random bottom-up approach by Dr Tongtong Zhu in the group of Professor Rachel Oliver at the University of Cambridge (United Kingdom). For growth of QDs on the non-polar *a*-plane, two methods have been employed: the modified droplet epitaxy (MDE) method and the quasi-two-temperature (Q2T) method explained below. Both were carried out in a 6×2 inch Thomas-Swan close-coupled showerhead reactor, using *r*-plane $(1\bar{1}02)$ sapphire as substrates. The GaN buffer was grown under a temperature of approximatelz 1050 °C, a pressure of 100 Torr and a V/III ratio of approximately 60. For the InGaN growth with a nominal In content of 25%, the temperature was decreased to approximately 690 °C [99]. The samples were capped with another layer of GaN. The samples were then processed by John Jarman of the same group into devices like LEDs (see chapter 4) or lateral opposing Schottky contacts (see chapter 5), or dry-etched into randomly located pillars for enhanced light extraction (see an example picture Figure 3.1(b) and chapter 6). A table of the samples used in the experiments is given in the appendix (section 8.1). The unconventional choice of the non-polar growth plane comes at a cost of an increased density of dislocations [96], particularly of threading dislocations which proved detrimental to the emission of QDs [100]. To reduce their density, a technique called epitaxial lateral over-growth (ELOG) has been used for some samples. It involves the masking of the sample with approximately 100 nm thick SiO_2 stripes of a few microns width and distance aligned parallel to the *m*-direction, and then continued GaN growth under conditions promoting lateral over-growth. In parts of the over-grown area, the threading dislocation density could be reduced by two orders of magnitude [96]. In Figure 3.1(a) an optical microscope image of an ELOG sample is shown.

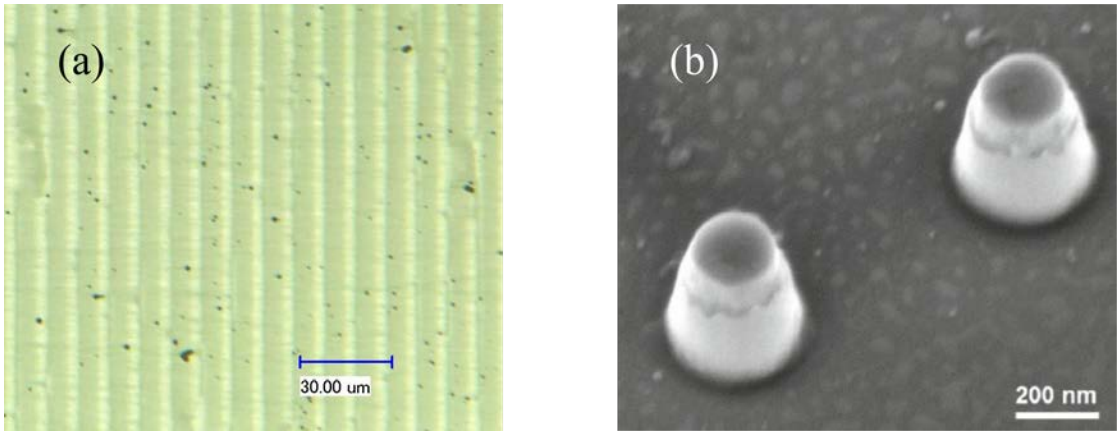

Figure 3.1: (a) Optical microscope image of an ELOG sample. (b) Scanning electron microscope image of single nanopillars, adapted from Ref. [66].

3.1.1 Modified droplet epitaxy growth

Droplet epitaxy is a common method used for the growth of arsenide QDs. Metallic droplets of the group-III element are deposited and then subjected to a flow of group-V material, reacting with it and crystallising out as III-V islands [101, 102]. For nitrides, this recipe has been modified. First, a few monolayers of InGaN are deposited. They are then annealed at the same temperature in an atmosphere without an active source of nitrogen, whereupon the InGaN layer breaks up at indium-rich positions and the deposition of small metallic In clusters can be observed. Subsequent overgrowth with GaN supports interdiffusion of Ga and N and crystallisation, thereby creating QDs [103]. This recipe has been developed for QD growth on polar GaN, though it works also for growth on the non-polar *a*-plane [96]. A special feature of this growth method is the broken-up thin InGaN layer acting as a QW.

3.1.2 Quasi-two-temperature growth

A second method of growing InGaN QDs has been specially devised for the *a*-plane. According to a detailed analysis of uncapped samples, the growth method is a hybrid between the island Vollmer-Weber growth and the strain-relaxation-driven Stranski-Krastanov growth [104]. The formation of nano-structures was prepared by depositing a

few monolayer thick InGaN layer capped with approximately 2 nm of GaN grown at the InGaN growth temperature of 680 °C. Next, a temperature ramp over 90 s to 860 °C in an atmosphere of nitrogen and ammonia was carried out. Then, a higher-quality cap of 8 nm GaN was grown using N_2 as carrier gas. Comparisons of atomic force microscope (AFM) measurements of uncapped samples show a much smoother surface obtained by the Q2T method compared to the MDE method [99, 105].

3.2 Micro-photoluminescence setup

The microphotoluminescence (μ-PL) setup was comprised of several laser sources being guided by fibres and an opto-mechanical system to the samples held in a helium-cooled cryostat. The photoluminescence (PL) was collected through the same objective used for excitation and could be analysed spectrally and temporally, with regard to polarisation and to the second order correlation function. Furthermore, two dimensional maps of the size of approximately $100 \times 100\,\mu\text{m}^2$ could be taken. The individual components of the systems are described below in detail. Particularities of each setup configuration used for the three different experimental projects are described in the individual chapters.

3.2.1 Laser excitation sources

Four different laser sources have been used. Mostly, a mode-locked Titanium-Sapphire laser (Mira 900, *Coherent*), pumped by a continuous wave (CW) intra-cavity doubled Nd-YAG laser (*Coherent* Verdi V8) was used. Its repetition rate was 76 MHz and it was used in ps-mode with a typical pulse duration of 1 ps. It was used at an approximate wavelength of 800 nm to excite QDs via the InGaN QW through two-photon absorption. The created carriers then relax non-radiatively to the QD ground state within a few femtoseconds. This excitation scheme has proven to be beneficial for the QD-to-QW ratio,

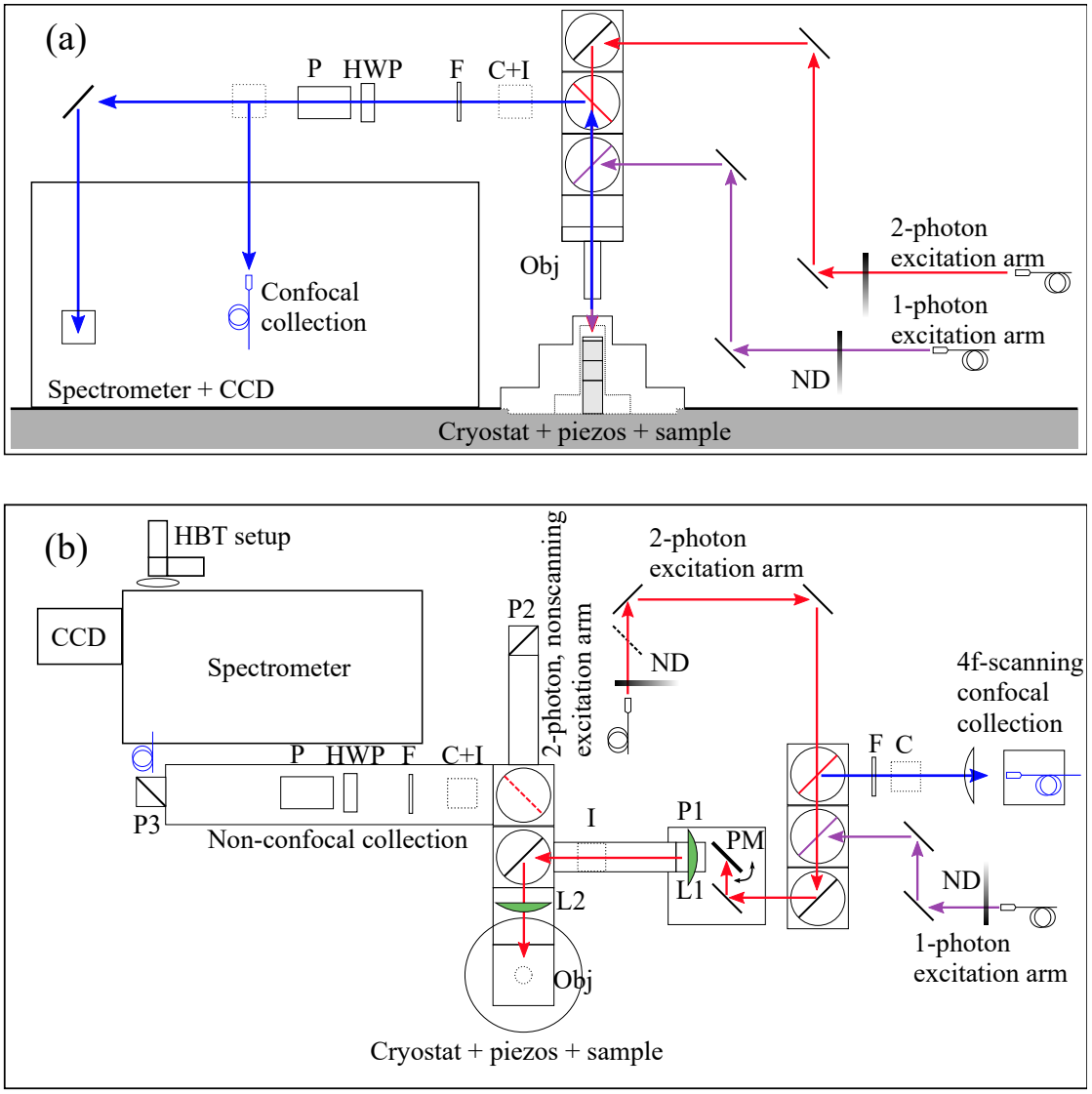

Figure 3.2: (a) Setup version 1, side view. The optical paths of the two-photon, one-photon excitation and the collection path are sketched by red, violet, blue coloured arrows, respectively. (b) Setup version 2, top view. The optical path is sketched for the setup in the 4f-scanning configuration (see subsection 3.2.4). For the sake of clarity, overlapping beam paths (arrows) are not shown, in contrast to (a), mostly the two-photon excitation path is shown. Abbreviations: ND neutral density filter wheel, Obj objective, I illumination, C camera, F filter to reduce excitation laser scatter, HWP half wave plate, P polariser, PM piezo mirror, L_i removable lens for the 4f scanning system, P_i periscope in setup version 2. Since the setup is in the state for 4f-scanning, the 25 μm-core multimode fibre collects the PL and sends it directly into the spectrometer. The lens used for free-space coupling is unmounted and not shown here.

reducing the QW signal in favour of the QD emission [106]. It has been shown through an autocorrelation measurement of a QD emission line that the absorption mechanism is simultaneous absorption of two photons via a virtual state [107]. A second mode-locked Titanium-Sapphire laser (Tsunami, *Spectra-Physics*) produced 100 fs pulses at a similar repetition rate. It was frequency-doubled with a commercial doubling system (Inrad 5-050 Ultrafast Harmonic Generation System) using an LBO crystal and was then used for pulsed one-photon excitation (in section 6.3) or for the determination of the instrument response function of time-resolving detectors. In chapter 6, one-photon CW excitation was extensively used, provided by a 405 nm laser diode. For the alignment of the telecentric 4f-scanning system described below in subsection 3.2.4, a CW 473 nm laser diode was also used. Since the opto-mechanical system was located on a vibration-damped table, the Titanium-Sapphire laser emission was coupled into single mode fibres, to avoid potentially dangerous changes of the beam path. Furthermore, the fibres spatially cleaned the laser spot to a close to Gaussian mode, enabling smaller focussing spot size on the sample.

3.2.2 Cryostat

A closed-cycle cryostat (AttoDRY 800, *Attocube*) in-built into a vibration-damped optical table was used. In order to exchange samples, the vacuum-tight cryostat lid and the heat shield needs to be removed. Under the heat shield, the cryostat contains 3 translation piezo positioners to move samples (2×ANPx101, 1×ANPz101, *Attocube*). They possess a large motion range of 4.2 mm, provided by the slip-stick technique. On top of the positioners, an adapter plate (called stub from here on) can be screwed on and off such that the samples can be fixed on it. A thermally conductive silver paste was used to glue the samples down. Between the top most positioner and the stub, a gold-plated copper plate is located and thermally connected through fine copper braids to the cold finger below the positioners. This copper plate also contains the sample heater and

sample temperature sensor. Along with a PID controller, a sample temperature range of 4.5 K to 300 K can be reached and stabilised. Electrical signals can be fed into the cryostat by means of 6 pairs of twisted wires ending in sockets in the bottom of the cryostat. The connection between the sockets and the sample was made via thin copper wires soldered to a PCB chip glued on the sample, next to the stub, and wedge-bonds from there to the sample (see section 4.2). In order to be able to feed high frequency signals into the cryostat, a larger cryostat lid and a larger heat shield was designed and made (see subsection 4.6.2). The connections between the feedthroughs in the lid and the sample have yet to be established. However, the lid can already be used for low frequency experiments, as it offers conveniently more space to accommodate wires connecting the sample and the twisted wire pairs, to avoid wires touching the positioners as this lead to quick, unexpected changes in the PL. More details about the cryostat can be found in the PhD thesis of Tong Wang [86, section 2.3.2].

3.2.3 Opto-mechanical system

Every PL system has an excitation and a collection arm, which - for systems with reflection geometry - are joined by a dichroic mirror or a beam splitter. For this setup, there are two excitation paths because the dichroic mirror corresponding to an excitation mode dictates whether the excitation beam is reflected off the dichroic mirror or transmitted. For two-photon excitation ($\lambda \approx 800\,\text{nm}$), a dichroic mirror is used that transmits the laser (down to approximately 660 nm). For one-photon excitation, a dichroic mirror is used that reflects the laser light (Di02-R405-25x36, *Semrock*). Additionally, the separation of excitation paths for largely different laser wavelengths allows the use of wavelength specific, highly reflective mirrors.

Furthermore, each excitation arm needs a periscope. This is because the cryostat is built into the optical table such that the excitation light is focused from above through a long-distance objective onto the sample. At this point, the beam path is at least 24 cm

above the table plane. Since the fibre outputs of the excitation laser light are located at a more secure height of 14 cm, each excitation path has to include a periscope.

The *Thorlabs* cage system was used to build the opto-mechanical part of the PL system, as it is easy to assemble and align. Mostly 30 mm components were used, however for the dichroic mirrors and the first part of the collection arm 60 mm components were used. In particular, the dichroic mirrors were mounted on 2 inch holders, which slotted into 60 mm cubes. The first version of the PL setup, created by Dr Tim Puchtler, is shown in Figure 3.2(a). The three cubes for the (dichroic) mirrors are assembled on the axis of the cryostat, with the two-photon excitation path above the one-photon path, because the 800 nm laser is transmitted through its dichroic mirror. This results in a maximum height of the setup of 46 cm. In the second version of the PL setup shown in Figure 3.2(b), in order to reduce vibrations originating from the height of the setup, the cubes were assembled in the plane of the table. To direct the light onto the axis of the focusing objective, an additional mirror was inserted between the cubes and the objective. The maximum height could be reduced to 28 cm. An additional change is the realisation of the 4f-scanning system, detailed in the next subsection. It branches off the one-photon excitation cube. In case the 4f-scanning system would need to be bypassed because of limited excitation power due to the large number of mirrors in the 4f-scanning system, the other output side of the cube could be used for one-photon excitation. A photo of the setup is shown in Figure 3.3.

On the (non-4f-scanning) collection side, the least possible number of mirrors was used to keep the loss of PL signal at a minimum, while maintaining enough degrees of freedom to couple the PL easily correctly into the spectrometer. This was realised with two mirrors. The remaining laser light, which is transmitted through the dichroic mirror, was filtered out with a suitable filter (FGS900M for two-photon excitation, *Thorlabs*; BLP01-405R-25 for one-photon excitation, *Semrock*). In the collection path, a broadband half wave plate (AHWP05M-600 *Thorlabs*) and a Glan-Laser polariser could be inserted before the periscope to measure the polarisation dependence of the PL. An

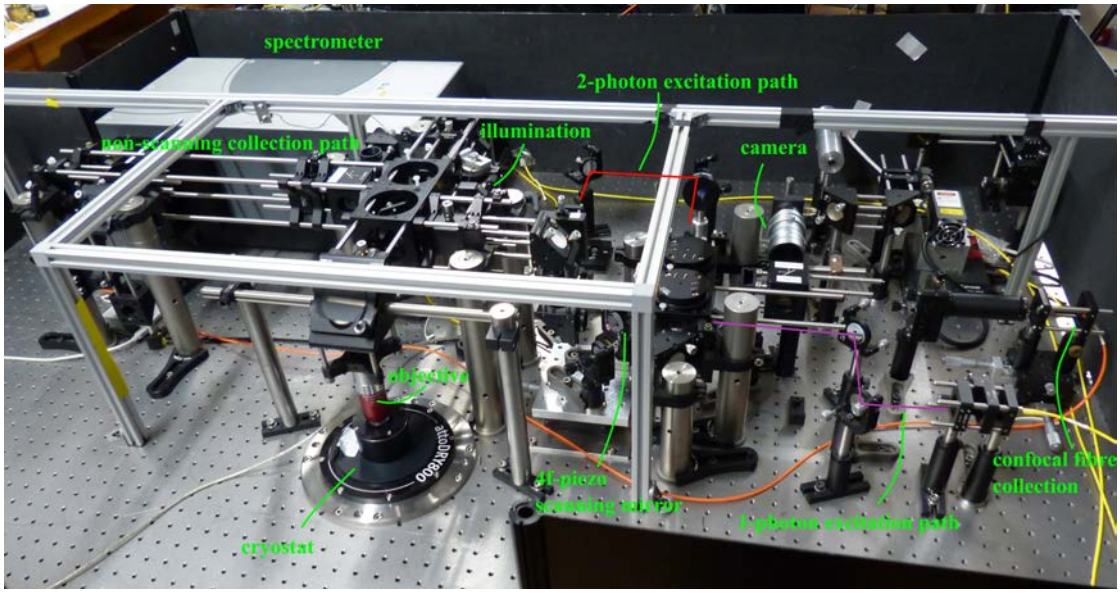

Figure 3.3: Photo of the setup version 2 in 4f-scanning configuration with the illumination glass-slide and the camera cube inserted. In the top right corner, the 405 nm and the 473 nm laser diodes including their fibre couplers can be seen.

adapter plate was designed and machined to allow the use of a computer-controlled *Physics Instruments* rotation stage to mount the half wave plate for automated polarisation measurements. It was found that a cube beam splitter should be used instead of a dichroic mirror to ensure that the setup does not change the PL polarisation state significantly. In Figure 3.4, the impact of the dichroic for the two-photon excitation on the PL polarisation is shown. For linearly p- or s-polarised light, it is minimal. However for polarisation angles in between, strong variations of both the degree of linear polarisation and also the polarisation angle can be seen over the wavelength, whereas for a cube beam splitter the distortions are much less. This is because of the relative phase shift after reflection between the s- and the p-component, which exhibits a complex wavelength dependence due to the many optical layers of the dichroic mirror. A 1.8 ° peak-to-peak oscillation in the polarisation angle originates from the non-perfect composite half wave plate.

The objective used for two-photon excitation was a long distance 100× *Mitutoyo* M Plan Apo NIR infinity corrected objective with a numerical aperture (NA) of 0.5 and

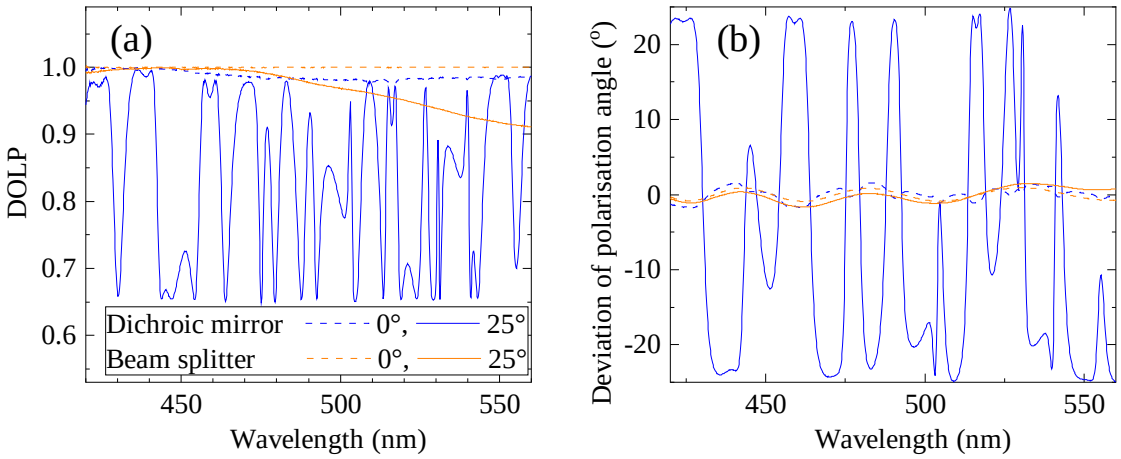

Figure 3.4: Setup polarisation properties with the dichroic mirror for two-photon excitation (blue) and a beam splitter cube (orange), probed with 100% linearly polarised white light. (a) Degree of linear polarisation for the probe light polarised at an angle of approximately 0 ° and 25 ° relative to the p-plane of the dichroic mirror/beam splitter. (b) Deviation of the maximum polarisation angle.

with the special property that the focal distance does not change for wavelengths between 480 nm and 1800 nm. For one-photon excitation, a 100× *Mitutoyo* M Plan Apo infinity corrected objective with a NA of 0.7 was used.

The sample surface could be seen with a camera when illuminated by a white light LED. In the non-confocal (non-4f-scanning) collection arm, both camera and illumination were spatially combined. In the 4f-scanning system, the illumination was positioned closer to the objective to enable maximum brightness, whereas the camera position was situated in the confocal collection path to reduce excitation laser scatter. To couple the elements into the optical bath, mirrors were used for the camera position and glass slides for the illumination positions.

3.2.4 Micro-photoluminescence mapping

In principle, the piezo positioners in the cryostat could be used to map the sample. However, the hysteresis intrinsic to piezo-electric positioners proved to be too strong and difficult to compensate. Instead, a so-called telecentric 4f-scanning system was

built outside of the cryostat. At the heart of it lies a mirror holder which can be tilted by a piezo positioner in two orthogonal directions (CONEX-AG-M100D, *Newport*). This sends the reflected laser beam away at a well-defined angle. It then meets a plano-convex lens, whose distance to the piezo mirror is equal to its focal length f. The beam is then (in general) focused off-axis and expands again. It is recollimated by a second plano-convex lens with the same focal length, which is twice the confocal distance away from the first lens. Finally, the beam hits the objective, which is again f away from the second lens. This arrangement means that the angle-change of the piezo-mirror is translated into an angle change of the beam when it hits the objective, with its position fixed on the objective aperture. The angled entrance of the beam into the objective then translates into a lateral change of the focus point of the objective on the sample. Since the angle change is maximally $\pm 0.76^\circ$, the paraxial approximation holds, such that a linear relation between angle and position on the sample can be assumed. Since the distance between the piezo mirror and the objective is $4f$, the total arrangement is called 4f-scanning system. PL emitted at the focus is then collected by the same objective and follows the same way as the excitation, and can be separated with a dichroic mirror. Since the piezo mirror holder has a very good accuracy and minimum step of 0.001° and a good bi-repeatability of 0.01°, maps can be taken without large hysteresis and QDs can be found again after a scan has finished.

When building the scanning system, the consideration for the focal length was that the shorter it is, the more stable the system is. Space restrictions yielded a minimum focal length of $f = 15\,\mathrm{cm}$. Unfortunately, this means that the second lens closer to the objective is also in the path of the non-scanning excitation path. Therefore, removable magnetic lens mounts were used. In order to bring the collected PL to the spectrometer, it is coupled into a multimode fibre because of ease, stability and to take advantage of confocal collection. A multimode fibre core diameter of $25\,\mu\mathrm{m}$ is chosen together with a achromatic lens with a focal length of $40\,\mathrm{mm}$ to collect the PL of an area of approximately $1\,\mu\mathrm{m}$ from the sample surface when one of the $100\times$ objectives is used.

In order to not further increase the number of mirrors, a carefully aligned mount with six degrees of freedom is used for the lens (K6XS, *Thorlabs*) and the fibre holder is mounted on two manual translation stages to move the fibre end parallel and perpendicular to the beam path. For a first alignment, the piezo scanning mirror was mounted together with a second mirror on two manual linear translation stages to be able to adjust the distance to the first lens while maintaining the alignment. In general, it was found that the best alignment accuracy is obtained by first aligning the 800 nm laser beam as it covers longer distances between mirrors, and then overlapping the 400 nm beam with it. To align the confocal collection, a laser is used with a wavelength above the one-photon dichroic transmission cut-off and below the two-photon dichroic reflection cut-off. A 473 nm CW diode laser was available.

A major obstacle to stable scanning proved to be the old air conditioner in the laboratory. Its periodic on-off-cycle led to a periodic change in the setup alignment over the course of a few minutes, resulting in drifts in the maps larger than the laser spot size. To circumvent this problem, a box was built to contain the whole table, with lids on top to access individual parts of the setup. This proved to be vital to buffer and dampen the temperature variations. The box excluded the cooling fan of the CCD in order to avoid increased heat input and strong convection inside the box.

Since optical systems with many components can be difficult to align very well, a calibration method is helpful. Here, this is demonstrated by means of a hexagonal array of pillars. It consisted of core-shell structures of multiple InGaN/GaN QWs with a pitch of 2 μm between pillars, fabricated by displacement Talbot lithography by the group of Dr Philip Shields at the University of Bath. A map of this sample taken with one-photon laser excitation at 405 nm at room temperature is shown in Figure 3.5(a), where the QW emission was integrated for each pixel. To determine the x- and y-calibration factors in order to be able to convert angle to distance, a *Python* script written by Luke Nuttall from our group was used. It fits the data with a grid to determine the pillar positions for later use and calculates the discrete two-dimensional Fourier transformation, shown in

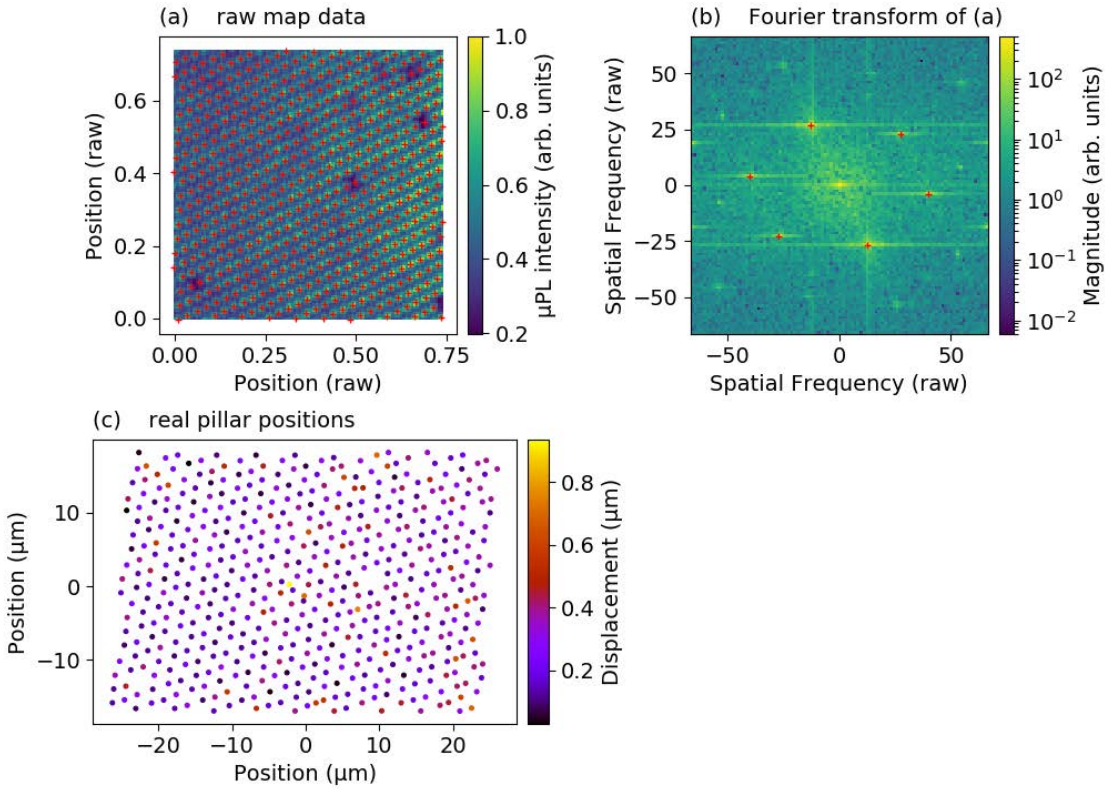

Figure 3.5: Calibration of the 4f scanning system. Figure generated by the program coded by Luke Nuttall, data acquisition by myself. (a) PL map with the objective $NA = 0.5$ on a regular pillar sample with a pitch of $2\,\mu$m. (b) 2D Fourier transformation of (a). (c) Corrected pillar positions.

Figure 3.5(b). A distorted hexagon is fitted to it. It turned out that also a shear factor was needed to explain its shape. This can be seen in panel (c), where the real pillar positions are plotted: The mapped area is a parallelogram instead of a rectangle. This is likely due to non-orthogonal mapping axes because of misalignment. Thus, for precise maps, it is helpful to use a calibration sample after each alignment of the scanning system.

3.2.5 Spectrally resolved detection

A Czerny-Turner spectrometer with a focal length of 0.5 m and an f-number of $f/6.5$ was used (Shamrock 500i, *Andor*). In the case of confocal collection, this was approximately matched by a $25\,\mu$m-core multimode fibre with an $NA = 0.1$, which is positioned directly in front of the spectrometer entrance slit. In the case of free space coupling, the

PL was focused into the spectrometer with a plano-convex lens $f = 50\,\text{mm}$ on a manual translation stage to adjust the distance to the input slit. The computer-controlled spectrometer has 3 reflection gratings on a turret: a coarse one with 600 l/mm and two fine ones with 1200 l/mm. The difference between the last two is that one has a blaze of 1200 nm for use in the infrared, whereas both other gratings have a blaze of 500 nm optimal for the blue-green InGaN emission. The mirrors are silver-coated. The detector is a Peltier cooled, 255 pixels high and 1024 pixels wide charge coupled device (CCD, iDus 420-BU, *Andor*), with optimised anti-reflection coatings for a wavelength window 400 nm to 500 nm with a quantum efficiency of over 90%. In order to achieve the best spectral resolution, the input slit of the spectrometer was usually set to $25\,\mu$m, matching the $26\,\mu\text{m}^2$-sized CCD pixels, yielding a resolution of 2.2 meV for the 600 l/mm grating and 0.73 meV for the 1200 l/mm grating at a wavelength of 450 nm. The acquisition of spectra was often carried out with a *Labview* program written by Luke Nuttall, which could also take 4f-scanning maps. I included an automated QD finding option interfacing with *Matlab*, an automated linear polarisation measurement with subsequent line fitting - also interfacing with *Matlab* - and the automated acquisition of spectra synchronised with the application of arbitrary voltage steps, using a GPIB-interfaced source-meter Keithley 236.

3.2.6 Time-correlated single photon detection

The spectrometer possesses of a flip mirror directly in front of the CCD, which can lead light close to the wavelength that corresponds approximately to the CCD pixel number 380 out of the spectrometer. This output has also a computer-controlled slit, which can be used to select a wavelength window for further studies. One might be interested for example how fast a photon is released from a QD after it was excited. Of course this can only be measured meaningfully for a larger number of photons, which is referred to as lifetime. In order to measure the arrival of single photons, time-correlated single

photon counting (TCSPC) has been developed. It works for faint light sources that are periodically excited, for example by a pulsed laser. A single photon detector, for example a photomultiplier tube (PMT), is used to measure the arrival of the photon. A special TCSPC card then determines how much later this signal arrived compared to the clock signal derived from the pulsed laser. It builds up a histogram which reveals with growing event numbers more and more precisely how fast and through how many channels the excited excitons decay. Here, a *Hamamatsu* H10720 PMT and a *PicoQuant* TimeHarp260 TCSPC card were used. The time resolution was approximately 270 ps. Further details about time-resolved measurement techniques can be found in reference [108].

In order to measure the second order correlation function introduced in section 2.4 in order to be able to tell if a stream of photons is made up of photons emitted one by one, an Hanbury Brown and Twiss (HBT) setup is used, consisting of a 50:50 unpolarising beam splitter (A10035 *Hamamatsu*, $T \approx R \approx 0.3$) and a single photon detector on each output. Their signals are processed by the TCSPC card essentially the same way as in the lifetime-measurement. Similarly, a histogram of coincidence counts, of events registered at one detector and events detected at the second detector, is built up over the time delay. A single photon cannot be detected at two location at the same time, therefore the value of the second order correlation function for a single-photon source will be zero. Recently, also a list of all detected photons can be saved, instead of just the histogram. This is the so-called time-tagged mode. The second order correlation function can then be calculated post measurement. For the measurements in chapter 6, the HBT setup was positioned at the output slit of the spectrometer. The PL was refocused on the PMTs by means of a biconvex lens with a focal length of 25 mm. For the HBT experiments in chapter 4, the spectrometer was bypassed to increase the number of counts on the PMTs, routing the light from the confocal collection, realised by a 5× objective and a 25 μm-core multimode fibre, by the latter to the HBT setup and collimating it with a screw-on lens. The spectral selection was achieved by placing two tunable bandpass

filters (TBP01-449/15-25x36, *Semrock*) with a sharp cut-off in the collection arm. To ensure that during a long HBT measurement the QD in question does not drift away, an optimisation script implemented in *Labview* by Luke Nuttall was used, employing the piezo positioners in the cryostat.

4 Electroluminescence studies of non-polar InGaN quantum dots

4.1 Introduction

Real world applications of QDs are very dependent on practicability. In this regard, electrical excitation represents a major improvement when compared to optical excitation because it reduces the equipment cost and enables a more compact and robust setup. In order to achieve electrical excitation, QDs are commonly sandwiched in a p-i-n diode. In nitride materials, achieving highly conducting p-doped layers is challenging. Nevertheless, several groups have reported successful electroluminescence (EL) of nitride QDs [55, 56, 109, 110]. However, only a few groups have demonstrated electrically driven single-photon emission in the blue spectral range [56, 95]. These groups used a restricted QW as a top-down engineered QD. Deshpande *et al.* employed a bottom-up grown, 30 nm-wide GaN nanopillar with a 2 nm-thin InGaN layer capped with GaN [95]. Pillars were dispersed on a substrate and a suitably positioned pillar was contacted with evaporated metal pads. Single photon emission was demonstrated with a second-order correlation function value at zero delay of $g^2(0) = 0.3(0.16)$ for a QD wavelength of 440 nm at a temperature of approximately 25K. The number in brackets is the value corrected for QW background. For a true single photon source, it should be zero and represents a technical check. However, one should bear in mind that this corrected value has no significance for practical applications, as the QW emission

cannot be separated from the QD emission at the same wavelength. The addition of an AlGaN hole blocking layer allowed for a value of $g^2(0) = 0.44(0.35)$ at 150 K with a QD emitting in the green colour range at 520 nm [112]. Note that room-temperature single-photon EL has been achieved with self-assembled InGaN QDs by Deshpande *et al.*, however in the amber colour range [55]. Zhang *et al.* followed a different, top-down approach, etching down a planar 2 nm-thin InGaN/GaN QW into 30 nm-wide nanopillars [56]. The sample was then planarised with spin-on-glass. Focusing on a single nanopillar yielded a value of $g^2(0) = 0.42(0.38)$ for a QD wavelength of 406 nm at 10 K.

However, both fabrication types come with the significant drawback of labour- and processing-intensive work. Furthermore, the nanopillar design does not allow for the integration into more advanced structures like photonic crystals. For these reasons, self-assembled InGaN QDs have been used here. Key results of this chapter are published here [113].

4.2 Sample and setup

QDs have been grown with the quasi Stranski-Krastanov method earlier described in subsection 3.1.2 as Q2T-growth. They were sandwiched in the intrinsic part of a p-i-n junction as shown in a schematic sketch in Figure 4.1. The 2 μm-thick GaN bottom layer was Si-doped with a concentration of $3 \times 10^{18}\,\mathrm{cm}^{-3}$. The p-doped GaN top layer had a thickness of 130 nm with a Mg dopant concentration of $3 \times 10^{19}\,\mathrm{cm}^{-3}$. To increase the QD density, 5 layers of QDs have been grown with an intermediate GaN thickness of 7.5 nm. The QD density is estimated to be approximately $1 \times 10^{8}\,\mathrm{cm}^{2}$ per layer. Electrical contacts were established with conventional UV photolithography. Ohmic contacts to the *n*-GaN were fabricated with a layer sequence of Ti/Al/Ti/Au with the thickness of 15/10/5/80 nm. To account for the low conductivity of *p*-GaN, a transparent current spreading layer made of Ni/Au with a thickness of 4.5 nm each was used. The

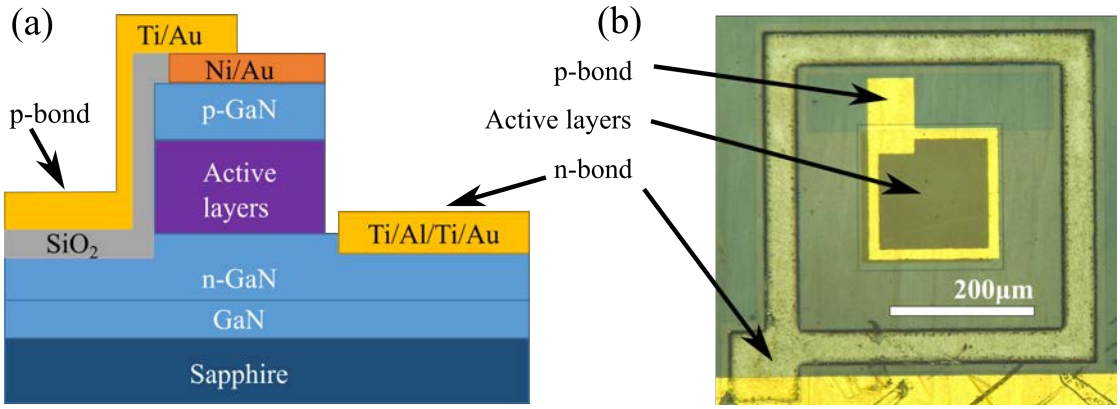

Figure 4.1: LED device. (a) Schematic. (b) Optical microscope image of the device used in this chapter.

Ohmic *p*-contact itself was fabricated with layers of Ti/Au with a thickness of 20/80 nm. The n-contacts were annealed at 710 °C for 2 min in a N_2 flow of 6 slpm (standard litres per min). The current spreading layer made of Ni/Au was annealed at 470 °C for 5 min in a N_2 flow of 5 slpm and O_2 flow of 2 slpm. The Ti/Au contact pads were not annealed. To enhance its mechanical stability a 200 nm-thick SiO_2 layer was used. Several device sizes and shapes were fabricated and wedge-bonded with an approximately 25 μm thick Al wire. The successfully employed device[1] had an active area of $180\times180\,\mu m^2$. An optical microscope image is shown in Figure 4.1(b).

Micro-EL measurements were performed with the first-version, confocal microscope setup described in Figure 3.2(a). The sample was glued with thermally conductive silver paste to a copper sample holder. A commercially available PCB chip[2] around it enabled electrical connections between DC cables feeding into the cryostat and the sample. To connect the PCB to the sample wedge-bonding was used with an approximately 25 μ-thick aluminium wire. A source-measure unit (Keithley 236) was used to excite the QDs held in a closed-cycle helium cryostat. The EL was collected with a high NA objective (NA= 0.5, 100× *Mitutoyo* Apo) and spatially filtered by focusing it with a 5× objective (*Mitutoyo* M plan Apo) into a multimode fibre with a 25 μm-diameter

[1] The yield was as follows: of 290 devices, 15 devices exhibited promising IV-curves in forward bias at room temperature. Of the 11 devices bonded, 1 showed EL at 4 K.
[2] Produced by AttoCube matching their sample holder.

core, corresponding to an approximately 1 μm-wide collection spot. The two-photon dichroic mirror was used to allow for two-photon excited PL. The EL was then spectrally characterised with the setup detailed in subsection 3.2.5, or spectrally filtered with two tilted bandpass filters and directed to the HBT setup detailed in subsection 3.2.6. The HBT channel bin width was set to the minimum with of 25 ps.

In Figure 4.2 the IV curve of the device is shown at 290 K and at 4.5 K. On a linear scale, a typical diode behaviour can be observed with low current under reverse bias and rapidly increasing current under forward bias. At 4.5 K, the onset voltage is larger as commonly observed due to a reduction in hole mobility and difficulty in activating acceptors [114, 115]. The forward bias regime of the room temperature curve has been fitted implicitly with the Shockley diode equation describing the current I through a pn-diode given an applied voltage V [116]

$$I = I_s \times \left(\exp\left(\frac{q(V - R_s I)}{n k_B T} \right) - 1 \right)$$

including a series resistance $R_s = 540(30)\,\Omega$ (contact resistivity $0.17\,\Omega\text{cm}^2$) and with a reverse bias saturation current $I_s = 39(4)$ nA, an ideality factor $n = 20.0(3)$, the Boltz-

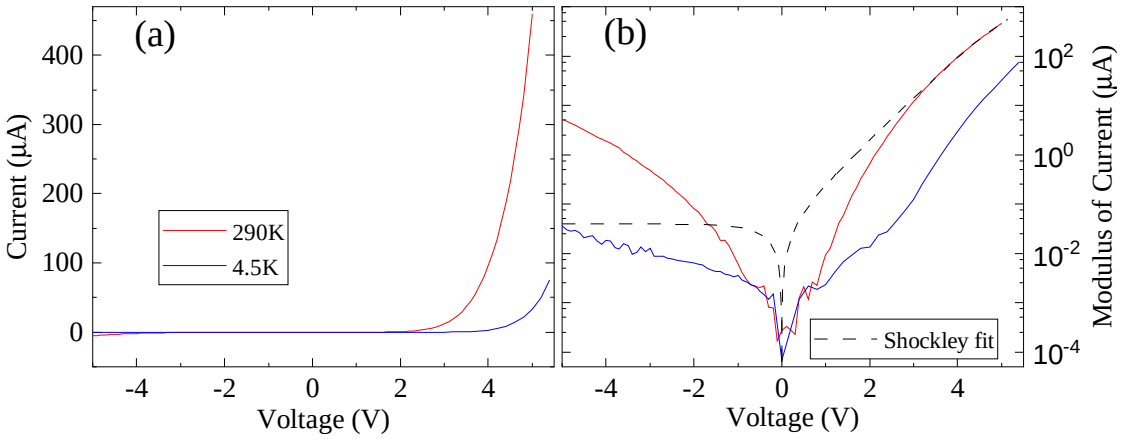

Figure 4.2: IV curve of the diode at 290 K and 4.5 K with a linear (a) and a logarithmic current scale (b). The dashed line is the best fit result to the high temperature forward bias data with the Shockley equation, yielding an ideality factor $n = 20$ and a series resistance $R_s = 540\,\Omega$.

mann constant k_B and the temperature T. The fit is plotted in Figure 4.2(b) on a semi-logarithmic scale. It is obvious that the fit does not agree with the IV curve apart from the high forward bias region, therefore the extracted fit parameters are only an indication and their uncertainty is much larger than the uncertainty given by the fit. In particular this applies to the ideality factor. Fitting the data with a decreasing upper limit of the forward bias results in ideality factors down to approximately 10. For an ideal diode n ranges between 1 and 2 due to competition between diffusion and recombination current [116]. However in nitride LEDs ideality factors in excess of 2 have been commonly observed in planar devices [115, 117] and also nanowire devices [118] and have been attributed to the additional influence of deep-level assisted tunnelling, moderately doped hetero-junctions and non-ideal metal-semiconductor contacts. Equally commonly, larger reverse bias currents than predicted by the Shockley equation were observed for nitride junctions [118–120]. This effect has been attributed to defect-assisted tunnelling or band-to-band tunnelling [120], which would fit the weak voltage dependence of the reverse bias leakage current. At 4.5 K there is an additional current at low forward bias visible in the semi-logarithmic presentation in Figure 4.2(b) whose origin is unclear. In previous reports the appearance of a low forward bias current component

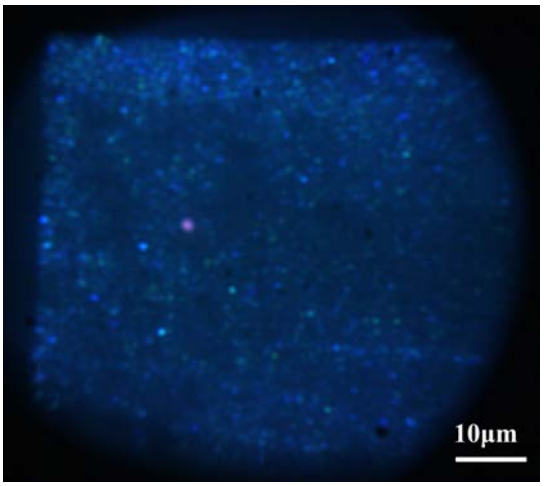

Figure 4.3: Camera photo of a corner of the device at a forward bias of 6 V. In the middle a red laser spot can be seen.

was shown to be non-radiative [119]. This fits with the results obtained here. Since the appearance of this current component makes it impossible to fit the data with the Shockley equation, the series resistance is estimated with a linear fit in the high forward bias regime to be five times larger than at room temperature, which is reasonable due to a reduced carrier mobility at 4.5 K.

In Figure 4.3 a camera image of the device driven at 6 V can be seen. It is obvious that the EL is not spatially uniform. The spottiness is likely to be due an inhomogeneous hole conductivity of p-GaN [121].

4.3 Spectral characterisation

In this section, the dependence of QDs and QW on the injection current is investigated. Three biexciton-exciton pairs were identified. Furthermore, the strong linear polarisation of both QD and background emission is studied.

4.3.1 Injection current dependence

Typical EL spectra taken at 4.5 K are shown in Figure 4.4 and 4.6. Narrow lines on top of a broad feature can be seen. The lines originate from single QDs, whereas the broad background stems from the QW.

QD line shifts

With increasing current, the lines can be observed to shift to both shorter and longer wavelengths and some also do not shift at all, as seen in Figure 4.4(b). A shift to shorter wavelengths can only occur if carriers confined in a QD experience an electrical field which is reduced. This results in a reduction of the QCSE and therefore a blue shift. One obvious source of an electrical field would be the in-built field, which is decreased through the forward bias. However, this is only true at below the onset of EL, at which

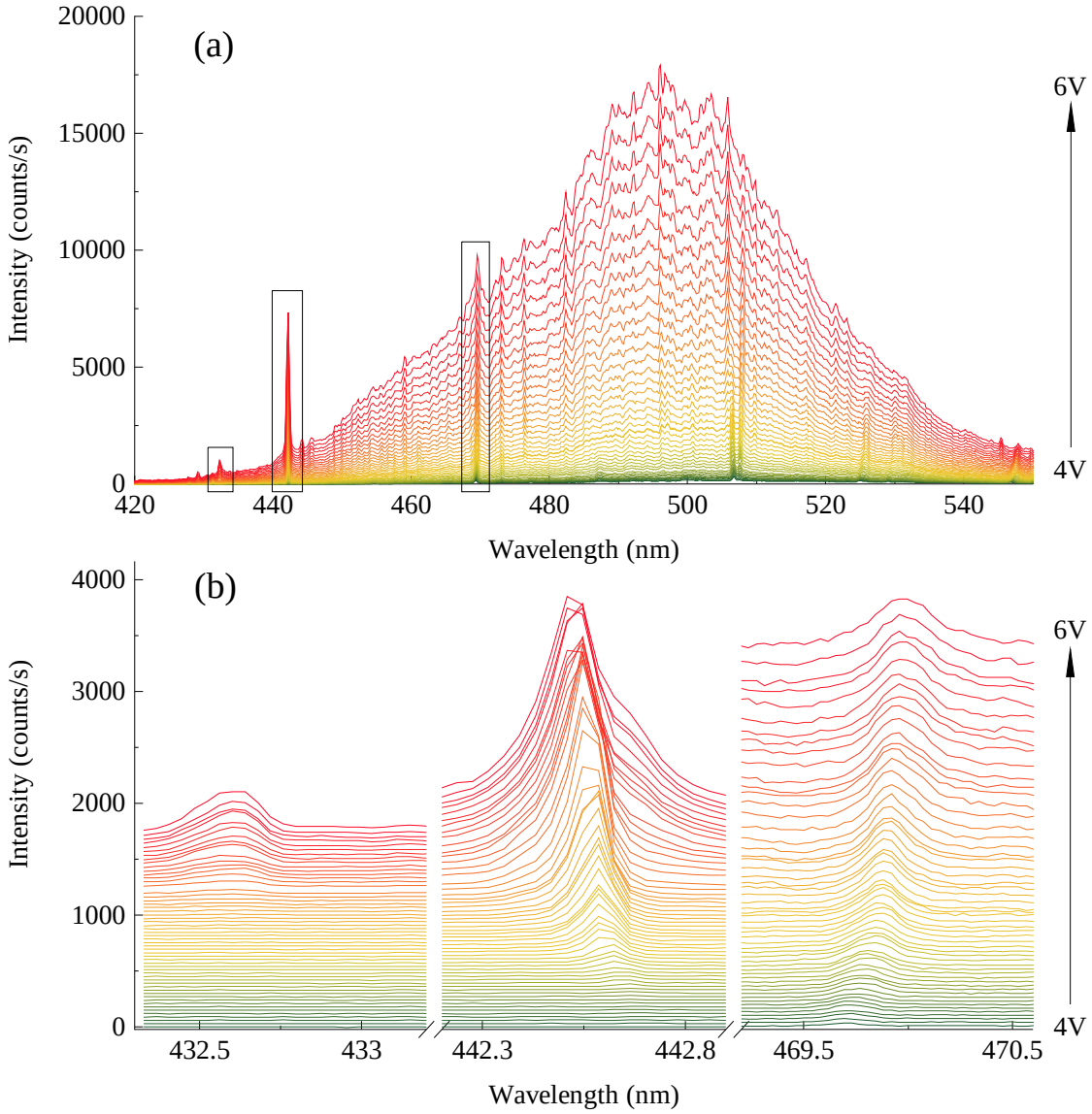

Figure 4.4: EL spectra at spot 1 with the forward bias ramping up from 4 V to 6 V with non-confocal collection. (a) Overview with 300 l/mm grating. The three marked lines are displayed in more detail in (b) using the 1200 l/mm grating and a constant stack offset of 10 counts/s for clarity.

point the bandstructure is approximately flat. This is the case at roughly 3.3 V, as a NextNano simulation of the device at 4 K showed. And the QDs appear only at higher voltages. There, the simulation shows an overall trend of an increasing field, but it depends crucially on the QW layer and its indium content. While the applied bias is likely to be the origin of the QD line shifts, one could also think that another mechanism might play a role. As $\mathbf{k} \cdot \mathbf{p}$ simulations of non-polar InGaN dots showed, there is an in-built

field along the *c*-direction due to the QD facets exposed to the polarisation discontinuity [122]. One could imagine that spatially anisotropic injection of predominantly one carrier type could lead to carriers accumulating close to a QD at for example a defect site, thereby generating an additional lateral electric field at the QD site. Depending on the relative position of the sites, this would reduce or enhance the in-built field, leading to a shift to shorter or longer wavelength, respectively. Spatially anisotropic injection is obvious from the spotty emission pattern in the micrograph depicted in Figure 4.3. Furthermore, at 4.5 K the conductivity of the p-GaN is much lower than that of the n-GaN, and so it is likely that more electrons than holes are injected into the active layer. Overall, the discussion shows that the QD wavelength dependence on the diode voltage is complex, and conclusions cannot be easily drawn from it.

Intensity dependence

The dependence of the intensity of the QD EL on the injection current can be studied however. To understand the context, it is useful to look at the behaviour of the QW first. An example is shown in Figure 4.5. In panel (a) the QW EL intensity L is plotted over the injection current I for several wavelengths. The emission did not contain bright QDs and was averaged over a 1 nm range. It can be seen that the curves are almost straight lines with a similar slope on a double-logarithmic scale. By comparison to the black dashed line with a slope of exactly 1, it is obvious that the intensity of the lowest wavelength range increases at first superlinearly, whereas the longer wavelengths initially increase sublinearly, before both settle for an almost linear increase in the higher current regime. This becomes clearer when dividing the measured EL intensity by the applied current, obtaining qualitatively the (external) efficiency of the diode as a function of injection current in Figure 4.5(b). At low currents the efficiency increases quickly. In the prominent ABC-model, this is attributed to the increasingly dominant radiative recombination over non-radiative Shockley-Read-Hall recombination where carriers are

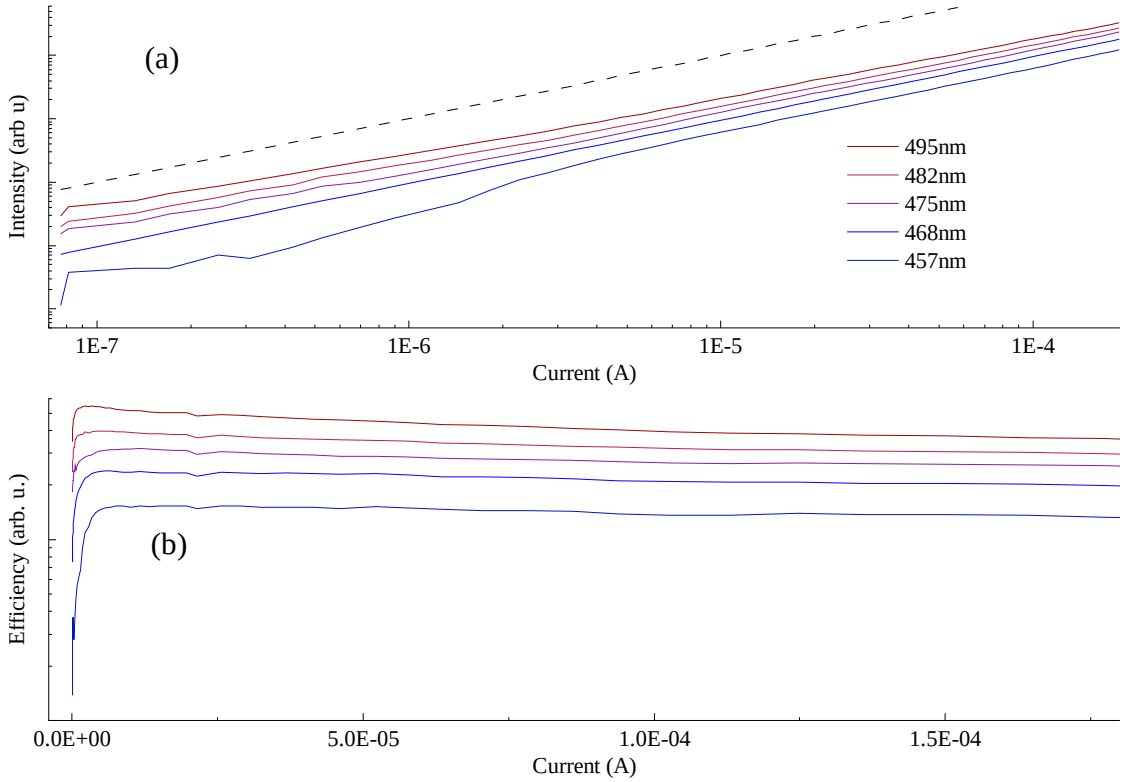

Figure 4.5: (a) EL intensity dependence on injection current density for several wavelengths averaged over 1 nm at spot 3, with non-confocal collection. The black dashed line with a slope of 1 is shown for comparison. (b) Efficiency dependence on current for the same wavelengths.

confined in deep traps [123]. For longer wavelengths the efficiency seems to peak at lower currents. This explains why a superlinear behaviour of the intensity was not observed at longer wavelengths within the measured current range. At higher currents, the efficiency stagnates for the shorter wavelength range and decreases for the longer ones. The longer the wavelength, the more the efficiency reduces. This is known as the efficiency droop, which is particularly strong in nitride LEDs [123–125]. Its origin has been much debated [123, 125]. Explanations most commonly involve Auger processes, but also carrier delocalisation, poor hole injection efficiency and carrier leakage from the active region. This explains the sublinear intensity behaviour at longer wavelengths and higher currents. With this knowledge we look at the relationship between QD intensity and current. Spectra taken at different currents above the highest efficiency peak current

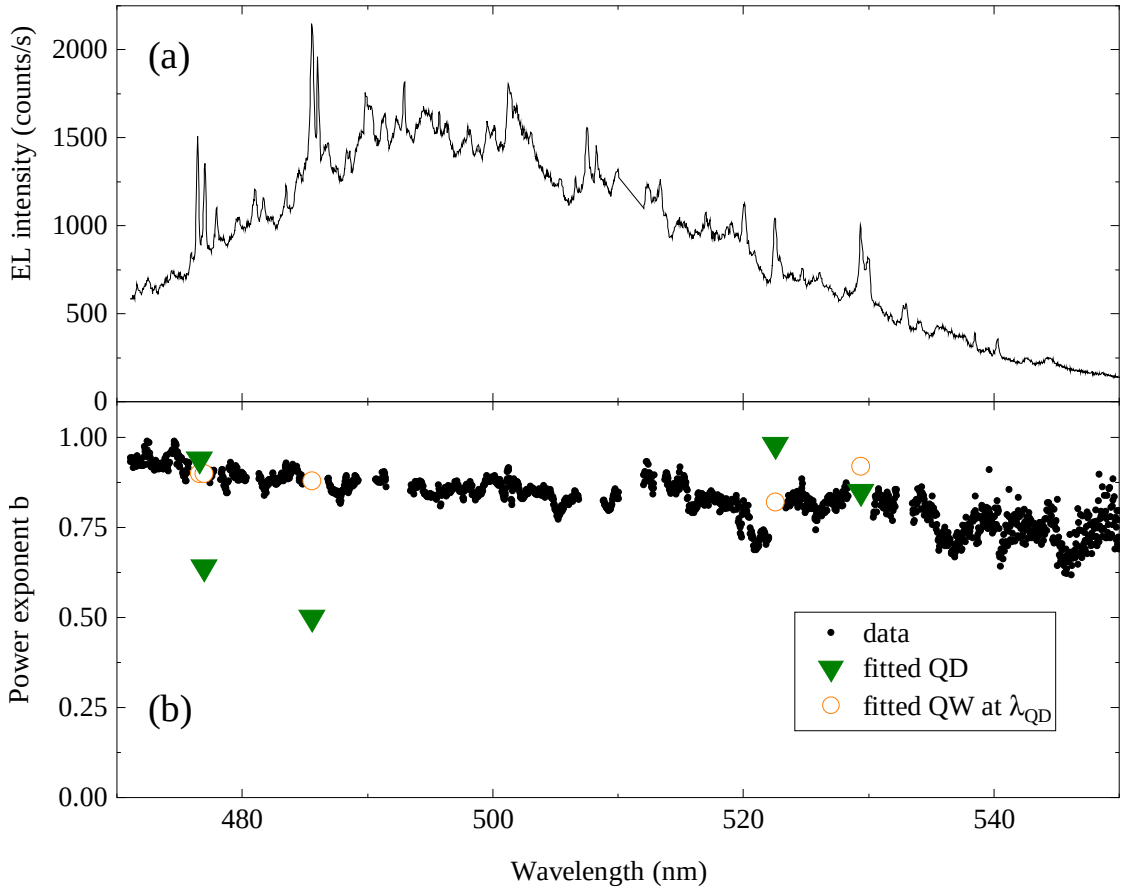

Figure 4.6: Excitation dependence at spot 3 with confocal collection. (a) Spectrum at a voltage of 5.4 V. (b) Power exponents as a function of wavelength of both QW and QD. The uncertainties do not exceed 10% and are omitted for improved readability.

were analysed for each wavelength except those that feature intense QDs lines. The integrated intensity and the spectrally underlying QW intensity of these dots was obtained with a Gaussian fit. To analyse the intensity as a function of current, the ABC model was not employed because of the higher complexity and the limited measured current range. Instead, a simple power law of the form $L = a \cdot I^b$ was used, fitting the data points at currents larger than the current for which the efficiency peaked. As discussed above, one would expect exponents close to 1, decreasing towards longer wavelength as the droop becomes more pronounced. This is exactly what we see in Figure 4.6(b) as a typical example. For the bright QDs visible in panel (a) the power exponent was extracted below saturation power. It should be noted that for some QDs the intensity-current re-

lation showed several abrupt changes, however this was not the case for the five QDs studied here. Two of the five QDs show a much lower power exponent compared to the spectrally close QW, whereas the other three align with the QW values. This sharp separation into two groups has also been observed at other positions on the sample. It might indicate that for some QDs the excitation efficiency is lower, for example due to surrounding potential barriers, or because non-radiative recombination is stronger. The second explanation is supported by a study on the influence of threading dislocations on the density of polar InGaN QDs [100]. The authors concluded that there was a positive correlation. This could mean that those dots form close to dislocations, which can act as non-radiative recombination centres if sufficiently nearby for tunnelling.

Biexcitons

In a more precise manner, through the study of the current dependence of QD emission lines, multi-excitonic complexes such as biexcitons can be identified. The knowledge of biexcitons can be useful to gain knowledge about the QD geometry [122]. Furthermore, in case of a vanishing biexciton binding energy, the biexciton-exciton emission cascade can be used to generate time reordered entangled photons [126]. Here, three biexciton-exciton pairs could be observed at different positions and identified by their correlated spatial appearance and intensity-current dependence. It is clear from the above discussion that the exponent of a biexciton (exciton) is expected to deviate from the ideal picture value of 2 (1), but nevertheless the biexciton power exponent should be twice the exciton exponent.

In Figure 4.7(a-c) the spectra of each exciton-biexciton pair are shown for several injection current values. The exciton emission wavelengths are 477 nm, 480 nm and 473 nm, respectively. The current dependence of the integrated exciton and biexciton intensities are plotted on a double logarithmic scale in Figure 4.7(d-f). The power exponent was extracted in the excitation range below the onset of saturation. It can be seen

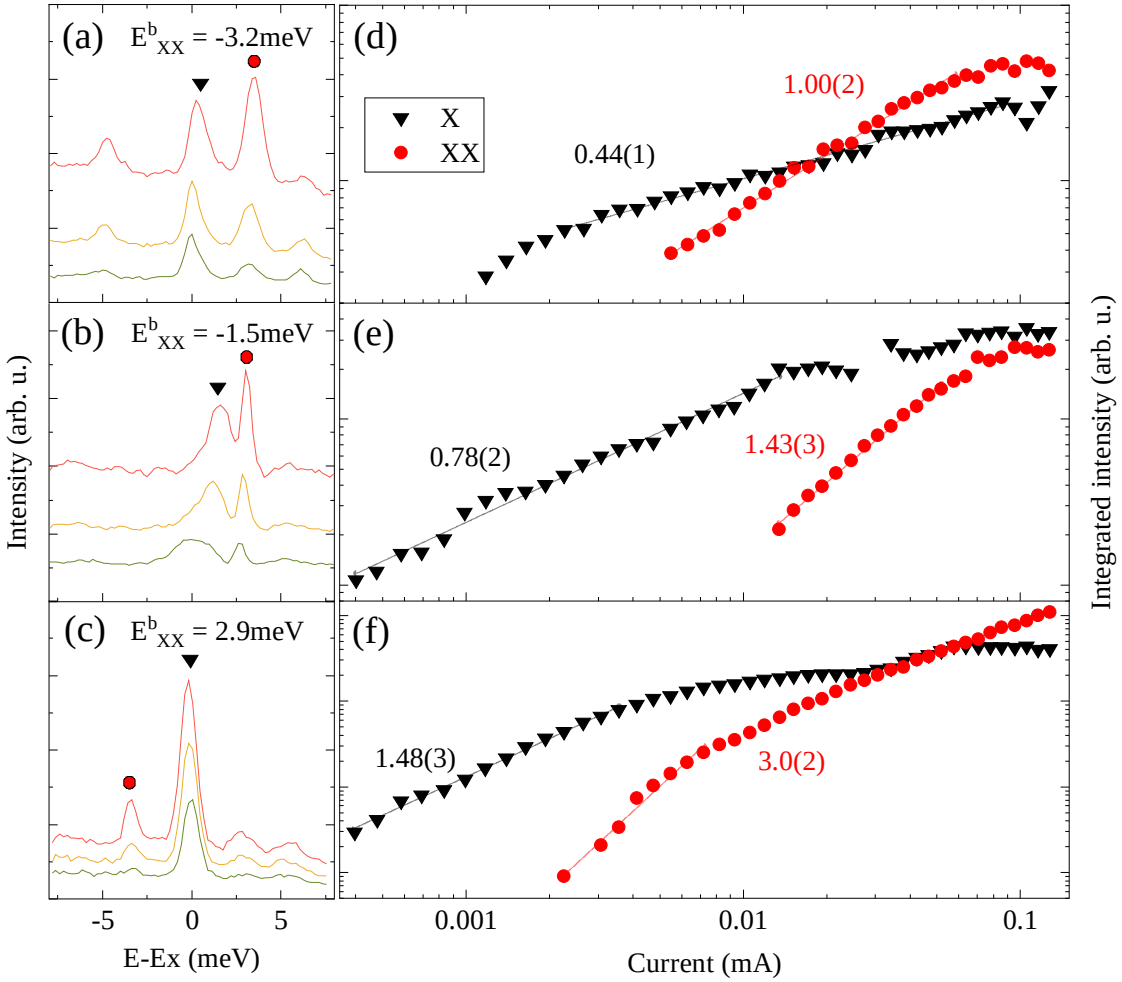

Figure 4.7: EL dependence of 3 biexcitons and their excitons at different spatial positions. In (a-c) the spectra are shown for three different injection current values. The intensity scale starts from zero. The injection current values were (a) 7 μA, 20 μA and 47 μA; (b) 15 μA, 31 μA and 47 μA; (c) 3.1 μA, 4.8 μA and 7.2 μA. In (d-f) the corresponding integrated intensities are shown as a function of injection current. The thick lines are linear regressions with the slopes given next to them.

that the ratio of the exponents of each exciton-biexciton pair is approximately 2 as expected. For the exciton in panel (f) the power exponent is larger than 1 which could be due to its early current onset and a locally stronger non-radiative Shockley-Read-Hall recombination, such that the excitation efficiency increases as the current rises. Polarisation measurements were conducted to determine the FSS of the exciton and biexciton lines to allow for further confirmation. However, no FSS could be detected due to con-

siderable wavelength changes during the measurements. This is likely to be a result of the enhanced spectral diffusion as compared to PL due to a higher number of carriers excited through electrical injection, as well as the long integration times needed to achieve a high enough signal-to-noise ratio for the low intensity polarisation component.

The emission energy difference between exciton E_{X} and biexciton emission E_{XX} results from Coulomb interaction between the electrons and holes inside the QD. In a simple Coulomb interaction model the biexciton binding energy can be expressed as [127]

$$E_{\mathrm{XX}}^{\mathrm{b}} = E_{\mathrm{X}} - E_{\mathrm{XX}} = -(2J_{eh} + J_{ee} + J_{hh}) \tag{4.1}$$

with the energies arising from the Coulomb interaction between the holes J_{hh}, the electrons J_{ee}, and electron and hole J_{eh}. The terms related to a single kind of carrier are positive, whereas J_{eh} is negative. The binding energies $E_{\mathrm{XX}}^{\mathrm{b}}$ lie between -3.2 meV and 2.9 meV. These are relatively small compared to typical *c*-plane InGaN QD biexciton binding energies. In the polar case, the strong in-built electrical field separates holes and electrons, thereby increasing the repellent terms J_{ee}, J_{hh} and decreasing the attractive one J_{eh} especially for larger QDs such that negative binding energies up to -41 meV could be found [111, 128–130]. In rare cases, small negative or even positive binding energies could be found, due to a small QD size [131–133].

For non-polar *a*-plane QDs, the in-built electric field is smaller as it only penetrates through the much smaller facets oriented along the *c*-direction, compared to the dot base area. Approximate self-consistent Hartree calculations show for a small QD height of 2.5 nm negative biexciton binding energies increasing in magnitude from -4 meV to maximum -17 meV with increasing QD base anisotropy (d_c/d_m =1 to 3) [122]. However these values are only a lower limit, as the calculation neglects weaker, though positive exchange and correlation terms. It should be noted that for a differently grown *a*-plane QD (MDE growth) a binding energy of $E_b = -36$ meV was found [64]. This could be the result of a larger QD height, enlarging the facets exposed to the polar direc-

tion and thereby increasing the in-built electric field as previously discussed. This was also qualitatively modelled with a 5 nm high QD with a slightly elliptical base plate of a size of approximately 30 nm [122]. The comparison between the measured biexciton binding energies against the theoretical calculations mentioned indicates qualitatively that the three QDs studied here should have a base anisotropy close to unity and exhibit a small height around approximately 2.5 nm. The small biexciton binding energy might enable time reordered entangled photons if a mechanism like electric fields or mechanic stress can be used to tune the binding energy to zero, as demonstrated for In(Ga)As QDs [134], thereby circumventing the need for a vanishing FSS to obtain entangled photon pairs [135].

4.3.2 Polarisation dependence

A high degree of polarisation of single photons is desirable for quantum cryptography schemes, as mentioned in section 1.1. Several groups reported on linearly polarised emission from InGaN QDs which was observed in PL [65, 66, 84, 85, 98, 111, 136, 137], EL [56, 95] and cathodoluminescence measurements [138]. Generally, nitride QWs and QDs grown on non-polar planes are expected and have been observed to emit linearly polarised light due to lifted valence band degeneracy caused by anisotropic strain (compare with section 2.3) [65, 66, 77, 81, 137, 139]. This can also happen in *c*-plane InGaN structures - provided that anisotropic strain engineering is done, be it intentional [84, 85] or not [56, 88, 98, 136, 138]. Note that all of these reports focus on light being collected parallel to the growth direction. But due to the valence band selection rules one can also observe polarised emission perpendicular to the growth direction for *c*-plane InGaN QDs or QD-like localisation centres in QWs [88, 95, 111]. However, this method neglects a large proportion of the emitted light and therefore reduces the collection efficiency [77, 140]. This is not a problem for non-polar nitride QDs as the emission perpendicular to the growth direction is negligible [66].

Not only the DOLP, but also the angle at which single photons are polarised is a prerequisite for quantum cryptography schemes, as the polarisation angle encodes the information to be transferred [2]. Only two groups examined the polarisation angle together with the DOLP for a larger number of InGaN QDs [84, 85]. While these reports on *c*-plane QDs used strain-engineering nanostructures, our QDs experience an intrinsically asymmetric strain due to growth on a non-polar plane. Therefore we expect our QDs to be aligned much more reliably to a crystal direction as our QDs are not influenced by unavoidable nanofabrication imprecision. In this subsection an estimation of the EL QD polarisation angle distribution width and also the mean QD DOLP is obtained.

Previous PL studies of our group established a high mean DOLP of 0.90(1) for *a*-plane QDs grown via MDE [66] and 0.87(1) for QDs grown via Q2T at 5 K [141], with the number in parenthesis being the standard error[3]. Even at 200 K, a mean DOLP of 0.77(1) has been observed despite thermalised occupation of higher hole states [141]. This behaviour is attributed to the dominant $|Y\rangle$-like character of the first few hole bands (compare with section 2.3). Furthermore, an alignment of the QD polarisation angles along a crystal direction had been established within $\pm 10^\circ$ [65, 66]. Theoretical calculations based on the $\mathbf{k}\cdot\mathbf{p}$ method by Patra and Schulz showed an alignment of the polarisation axis along the *m*-direction for an anisotropy of the base $d_c/d_m \leq 3$ [66]. However, for an anisotropy larger than 4 the polarisation axis aligns with the *c*-direction. This might explain differing results reported on *a*-plane QDs grown by similar methods: Reid *et al.* reported in 2015 an alignment along the *c*-direction [65], contrary to Wang *et al.* in 2017 who found an alignment along the perpendicular *m*-direction [66]. Additionally, the emission of InGaN QWs grown on the *a*-plane has been shown to be polarised along the *m*-direction due to strain produced through the heterostructure growth, albeit to a lower average degree of 0.7 [81].

[3] This is the standard deviation of the mean, equal to the standard deviation divided by the square root of the sample number.

Measurement and analysis procedure

Here the polarisation angle and degree for 76 *a*-plane QDs grown via the Q2T method has been measured in DC μ-EL. The setup version 1 described in subsection 3.2.3 was used. Additionally, in the collection arm a rotatable half wave plate (HWP) was used together with a fixed polariser behind it to project the polarised emission onto the polariser. This combination was used for several reasons. Firstly, the spectrometer has a non-trivial polarisation dependence which can be circumvented by fixing the polariser angle. Secondly, the rotation axis of the polariser mount does not coincide perfectly with the normal direction to its face, resulting in an angle-dependent beam deviation. This can lead to an intensity modulation because of the emission is not perfectly coupled into the fibre (or the spectrometer in case of non-confocal measurements[4]), leading to a deviation from Malus's law (Equation (4.2)) and therefore a biased polarisation angle and DOLP. Using a HWP instead reduces the problematic beam pointing change by a factor of approximately 20 since the HWP thickness amounts to only 1 mm compared to the 2 cm-thick polariser.

The data presented here is of preliminary nature because of later identified setup imperfections. An example of these is described in subsection 3.2.3 and shown in Figure 3.4. In brief, for certain wavelength ranges, the two-photon dichroic mirror acts like a HWP, rotating the polarisation angle by the angle difference between the luminescence polarisation and the p-plane of the mirror closest to the objective. Also, the DOLP is decreased by the setup for certain wavelength ranges. Both characteristics are stronger the larger the polarisation angle difference to the s/p-plane of the setup is. Here the sample was aligned such that the *m*-direction is at an angle of approximately 4° to the p-plane of the setup. This was determined by striations on the sample surface (visible in Figure 4.1(b)), observed with the optical microscope included in the setup. Therefore,

[4] In the non-confocal case, this will also change the position of the dispersed emission on the CCD, therefore introducing a small spectral shift. This could easily be mistaken as a fine structure splitting of the measured QD in question.

the data presented here holds as a lower bound for the DOLP and as a higher bound for the polarisation angle distribution.

All dots with a peak intensity of at least 200 counts/s observed with the 300 l/mm grating were measured with the higher resolution grating with 1200 l/mm. A driving voltage of 5 V was chosen as to predominantly excite excitons and not biexcitons. When searching for QDs by randomly scanning the sample, the polariser was taken out to avoid an angle selection bias. For each QD, spectra were taken in 5 ° steps over 180 °. Each spectrum was fitted with a Gaussian to extract the intensity, peak wavelength and QW intensity. A Gaussian was used because the observed emission width is expected to be dominated by spectral diffusion [142]. If the QD intensity was too weak at a particular angle, the spectrum at the particular angle was omitted. The resulting intensity of QD and QW was plotted over the polarisation angle and fitted according to Malus's law with two orthogonally polarised components with an intensity I_a, I_b and an angle offset Θ_0.

$$I(\Theta) = I_a \cdot \sin^2(\Theta - \Theta_0) + I_b \cdot \cos^2(\Theta - \Theta_0) \tag{4.2}$$

An example polarisation measurement is shown in Figure 4.8. In panel (a) the polarisation angle dependence of the spectra of a single QD is shown. In panel (b) the same dependence is shown for the integrated QD intensity and the QW intensity together with a Malus's fit. The QW polarisation angle $\Theta_0 = -5.3(3)$ ° is close to the *m*-direction, which corresponds here to 0 °, whereas the QD exhibits a larger angle of $\Theta_0 = -21(1)$ °. Since the intensity scales start from zero, one can also see that the DOLP of the QW is lower than that of the QW. To ensure that measurements of poor quality would not distort the distributions, dots with a Malus's fit with an adjusted $R^2 < 0.7$ were excluded. This was the case for 3 QDs, possibly caused by a strong slow-time scale spectral diffusion.

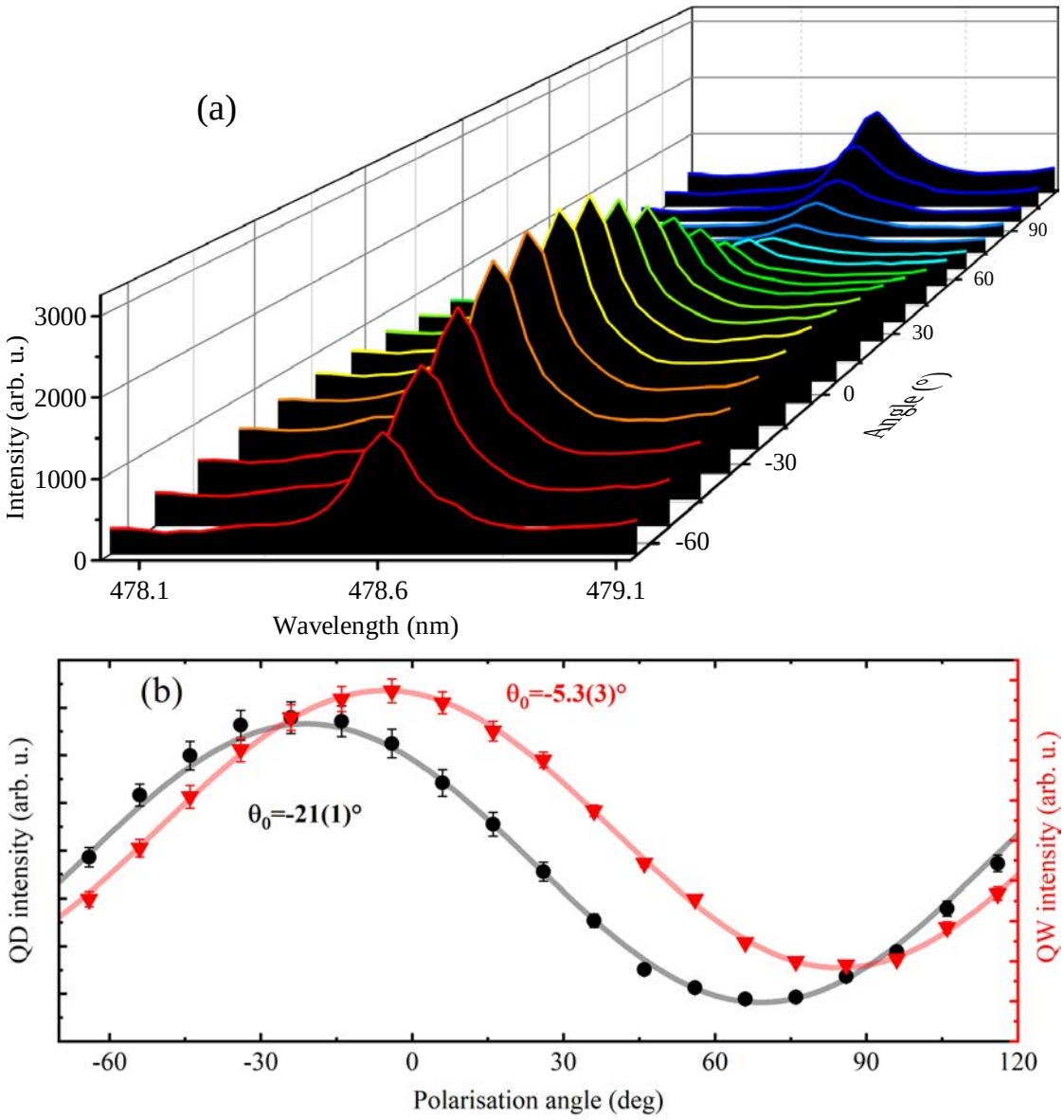

Figure 4.8: Example of a polarisation measurement. (a) Spectra for different polarisation angles. (b) Dependency of the integrated QD intensity and QW intensity on the polarisation angle. The lines are fits with Equation (4.2) and the extracted angles are given. The angle of 0 ° corresponds to the *m*-direction and the intensity scale starts at zero.

Measurement results

In Figure 4.9(a) the distribution of polarisation angles of both the QDs and the QWs at the emission wavelength of the respective QD is shown as a function of wavelength. The mean of both agree within 1 ° with the *m*-direction. The spread of QD angles is

with a standard deviation of 11 ° much greater than the spread of the QW angles with a standard deviation of 2.1 °. This can be seen more clearly in the histogram on the right side. On the one hand, the spread in QD and QW angles is partly caused by the setup imperfection mentioned before. Its influence is reflected in the QW angle spread: Since the crystallographic *c*-axis of the sample is fixed, the QW angles should be identical within the measurement uncertainty, which they are not, and also a spectral modulation is visible. On the other hand, the setup imperfection is the same for a fixed wavelength, meaning it is identical for a dot and its QW background. Since the QDs show a much larger angle spread, there has to be a second, more important influence on the spread apart from the setup. Since the biggest geometrical difference between QD and QW is that the former exhibits confinement in the growth plane as well, one could speculate

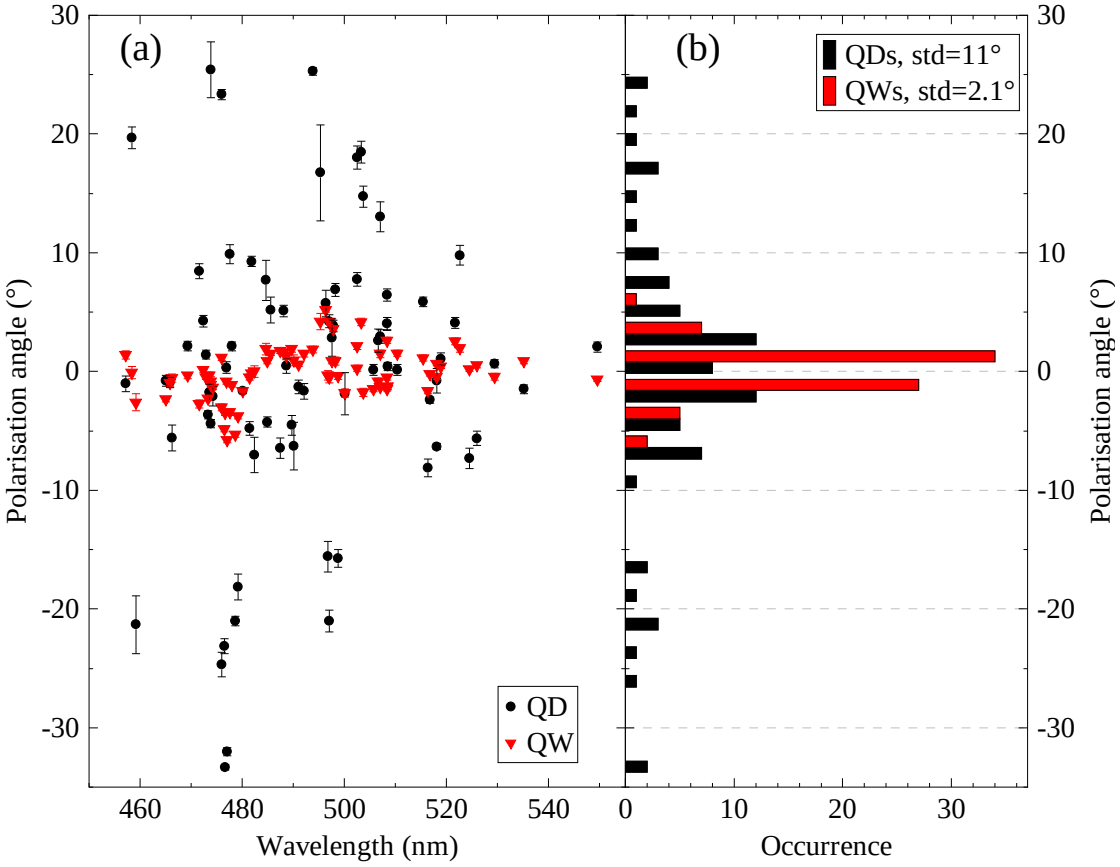

Figure 4.9: Distribution of polarisation angles of 76 QDs and the underlying QW. (a) Wavelength dependence. The polarisation angle of 0 ° corresponds to the *m*-direction. (b) Histogram of the QD and QW polarisation angles.

that the QD angle might be influenced by the orientation of the QD base or by indium segregation. The first explanation makes of course only a difference in case of a dot base deviating from a circle. This can be assumed to be the general case as it has been found for InGaAs QDs [89, 143]. The misalignment of the QD base in respect to the *m*-direction might be caused by strain deviations during growth originating from defects. This upper limit to the QD polarisation angle spread of 11 ° is of similar magnitude compared to the one measured by Teng *et al.* with elliptically top-down etched InGaN QWs. They reported a standard deviation of 13 ° [85]. Lundskog *et al.* achieved a higher degree of alignment with QDs grown on top of purposefully elongated pyramids where 90% of them emitting within ±10 ° compared to 75% in this study [84]. It remains unclear if this is due to a more stringent control of strain and shape on their part or due to the setup imperfections in our system. Further studies with a carefully characterised system would be needed to establish certainty. The dichroic mirror should be replaced with a 50:50 beam splitter cube as it has a heavily reduced influence on the polarisation of reflected or transmitted light, as can be seen in Figure 3.4. In Figure 4.10(a) the dependence of the DOLP of the studied QDs and their respective QW background is shown. Clearly, the QW DOLP distribution exhibits a spectral dependence, increasing from 0.5 at 460 nm to 0.75 at 500 nm and flattening out to 0.8 for longer wavelengths. This has been observed as well in PL studies of similarly grown *a*-plane QWs, however the origin of the lower DOLP at shorter wavelength has not been pinned down yet [81]. In the report, the DOLP was observed to increase again at even shorter wavelengths, which is not visible in this study as no QDs of sufficient brightness were found in that spectral range. The influence of the setup imperfections is not as noticeable as in the angle distribution. In contrast, the DOLP distribution of the QDs shows no spectral trend. Their mean value of 0.88, with a standard error of 0.01, lies well above even the highest single QW DOLP. This has been explained by a stronger carrier confinement in the QDs, enlarging the energy gap between the two highest valence bands, therefore enhancing the degree of polarisation [66]. The mean DOLP agrees with the two PL studies

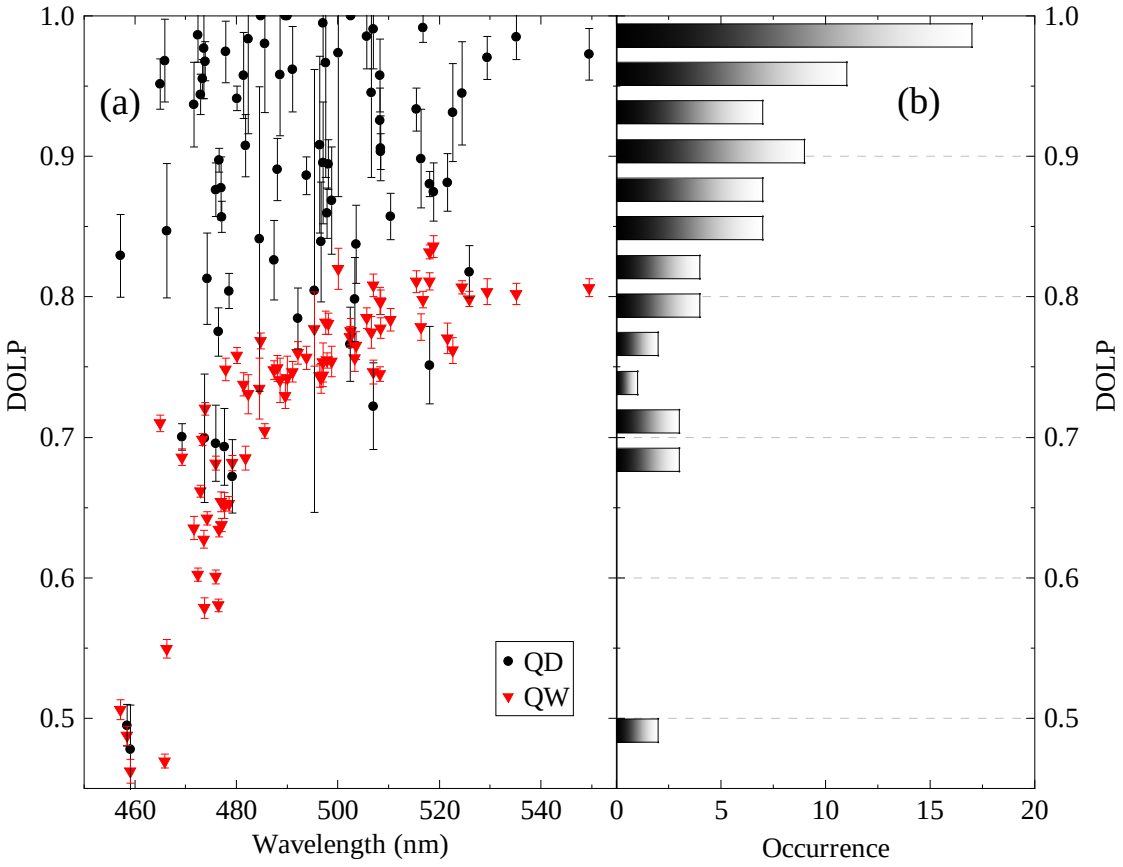

Figure 4.10: Distribution of DOLP of 76 QDs and the underlying QW. (a) Wavelength dependence. (b) Histogram of the QD DOLP.

cited above, which established a mean DOLP of 0.87(1) and 0.90(1) for Q2T and MDE grown *a*-plane QDs, respectively [66, 141]. It should be noted that the measurements described here are more sensitive than previous studies to the intensity minimum due to a 10 times longer integration time and also the systematic Malus' law fitting, such that a DOLP close to 1 could be better distinguished from 1. This will slightly decrease the mean DOLP observed here compared to the reports by Wang *et al*.

In Figure 4.10(b) the QD DOLP data is presented as histogram. It can be seen that the distribution peaks at the highest DOLP, meaning only a single linearly polarised component is present. This is highly desirable for future quantum cryptography applications, as many schemes use polarisation to encode information [2]. Even though the two above mentioned PL studies show a high mean DOLP of *a*-plane QDs, their distribution peak

at lower DOLP values. The same is true for the PL studies using strain engineered *c*-plane dots. This is reflected in the percentage of observed QDs with a DOLP$>$ 0.9: While these studies report a low part of 15% and 18% respectively [84, 85], here this is the case for more than 50% of the QDs. This large difference is likely to be due to a larger anisotropy for the *a*-plane QDs, be it caused solely by strain or additional shape anisotropy, which isolates the top most hole band from the lower ones [66]. This makes our QDs an excellent candidate for quantum cryptography schemes.

4.4 Single-photon emission

A high degree of QD polarisation is all well and good, but at the heart of the importance of QDs lies their ability to emit a single photon at a time. To ensure this is the case, an HBT measurement can be used to obtain the second order correlation function $g^2(\tau)$ of the luminescence (compare with section 2.4).

This measurement has been carried out with the QD presented in Figure 4.11 with the spectrum on the left and the polar polarisation plot on the right. The QD intensity dominates over the QW background emission so the dot properties can be effectively probed. The dot emission is highly polarised with a $DOLP = 0.94(1)$ and its polarisation angle coincides with the *m*-direction within 10 °. As the level of coincidence counts in the HBT measurement depends on the square of the input intensity, it is important to achieve a high EL flux. To this end, the sample luminescence is not directed through the comparatively lossy spectrometer, but it is bypassed and instead two tunable bandpass filters with steep edges are employed and the light is directly passed through the multimode fibre to the HBT setup described in subsection 3.2.6. The filtered QD spectrum can be seen in Figure 4.11. The minimum time bin of 25 ps was used.

The HBT measurement was running for 21 hours up to a level of 467 counts per time bin at long time delays. The histogram has been normalised to unity at long delays and is presented in Figure 4.12(c). The dip at zero delay is clearly visible. It has been fitted

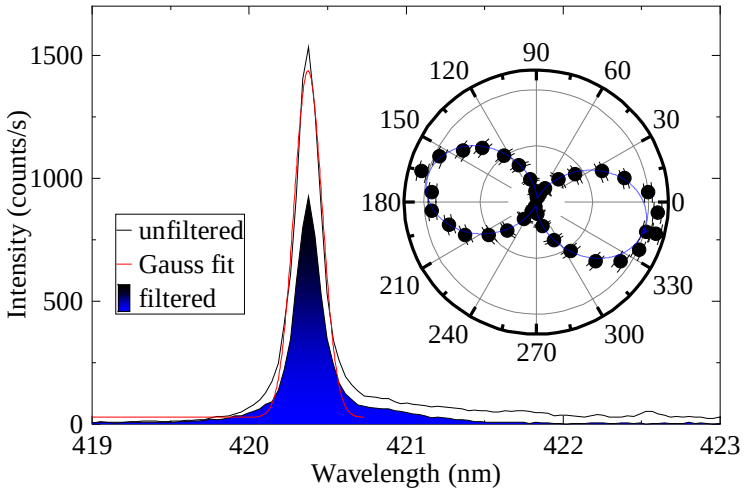

Figure 4.11: Spectra of the QD under question at a driving voltage of 5.8 V. The red line is a Gaussian fit. The graph with the filled area is the filtered spectrum. Inset: Polar polarisation plot of the same QD. The line is a Malus's fit (Equation (4.2)). 0 ° corresponds to the m-direction.

with the common formula [95, 98, 144]

$$g^2(\tau) = 1 - A \cdot \exp(-|\tau|/H) \tag{4.3}$$

with the dip of $g^2(\tau = 0) = 1 - A$ and the HBT rise time H. This model assumes a mono-exponential decay which has been shown in PL studies to be the case for Q2T and MDE grown a-plane InGaN QDs [64, 145]. The fit determines $g^2(0) = 0.67(2)$ and $H = 194(21)$ ps. The dip clearly does not go down to zero.

Correction for the instrument response function

However the instrument response function (IRF) of the HBT setup plays into the dip depth. As the lifetime of the emission of a-plane QDs is in general in the range of 200-700 ps [64, 145], it is likely to be on the order of the IRF. This means that the setup is not able to fully resolve the dip as it is too slow. However, the IRF can be taken into account as the measured HBT trace is the result of a convolution of Equation (4.3) with the IRF [144]. This shape can be calculated and fitted to the measured data. The IRF has

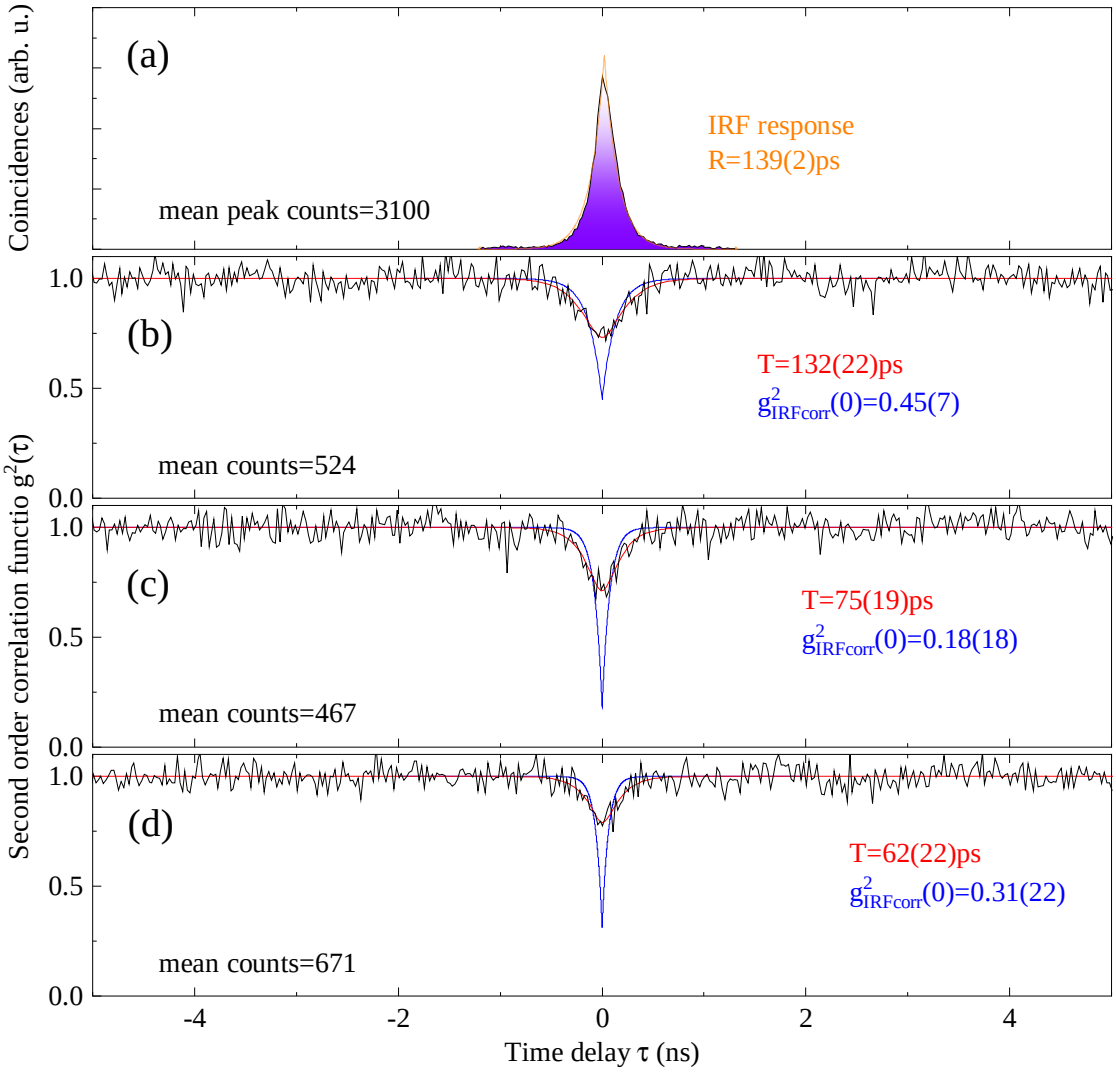

Figure 4.12: (a) Averaged IRF of the HBT setup. A mono-exponential decay has been used as a fit (Equation (4.4)). (b-d) HBT measurements of the QD under question. The red curve is a fit with Equation (4.3), whereas the blue fit line takes into account the IRF with the Equation (4.5). The driving voltage was (b) 5.6 V, (c) 5.8 V, (d) 6.1 V. The mean coincidence count level per bin is given.

been measured with an approximately 100 fs pulsed, 400 nm laser directly connected to the HBT setup through a fibre. To test its variation it was measured 48 times and the average is presented in Figure 4.12(a). It can be seen that the profile can be fitted well with an exponential function of the shape

$$\mathrm{IRF}(\tau) = B \cdot \mathrm{e}^{-|\tau|/R} \tag{4.4}$$

with an amplitude B and the decay time $R = 139(2)\,\mathrm{ps}$. This is on the order of the (convolved) HBT rise time H as assumed. Therefore a convolution is needed to obtain the true dip depth and true HBT rise time T, regardless of the instrument response. The calculation of the convolution is detailed in the appendix 8.2, yielding the following result for the IRF corrected second order correlation function.

$$g^2_{\mathrm{IRFcorr}}(\tau) = 1 - \frac{A \cdot T}{R^2 - T^2} \cdot \left(R \cdot \mathrm{e}^{-|\tau|/R} - T \cdot \mathrm{e}^{-|\tau|/T} \right) \tag{4.5}$$

Fitting the measured HBT trace with this equation with a fixed $R = 139\,\mathrm{ps}$, one obtains $g^2_{\mathrm{IRFcorr}}(0) = 0.18(18)$ and $T = 75(19)\,\mathrm{ps}$. Thus, the dip goes much further down, within the uncertainty even to zero. This proves that this QD does emit single photons under electrical excitation. There might be a small contribution from the background QW emission. However, it is difficult to determine the exact amount as the precise spectral QD shape is unknown. The Lorentzian shape of a damped two-level system is convolved with a Gaussian originating from spectral diffusion. In more detail the latter point means that due to the fluctuating charge environment close to the dot, the band gap changes slightly over time and so does the emission wavelength. The jitter occurs on two times scale, one of a few seconds and the other is much shorter, which will be investigated in chapter 6. This means for integration times on the order of seconds one will observe an averaged broader QD emission peak. Additionally, possible acoustic phonon side peaks can lead to difficulties of the background estimation. For example an HBT measurement which included more of the longer wavelength QD side emission seen in the unfiltered spectrum in Figure 4.11 did not result in a significant increase in $g^2(0)$, indicating that this part of the spectrum also originates from the QD. Due to those uncertainties and since the uncertainty of $g^2(0)$ is already quite large owing to the large timing bin of 25 ps compared to the true HBT rise time, a background correction is not attempted unlike in many publications [61, 63, 95, 144]. Note that the vast majority of CW HBT measurements of nitride QDs report a rise time T ranging between slightly

sub-nanosecond to a few nanoseconds [56,95,144] whereas here the rise times observed here are below 200 ps. Therefore correcting for the influence of the IRF makes a large difference.

Estimation of excitonic lifetime

Not only the dip depth, but also the HBT rising time T is extracted. Often wrongly interpreted as simply the exciton lifetime t_{QD} [56,95], it really has a second contribution which is the pump rate p. This can be understood as follows. The higher the pump rate is, the faster the QD is re-excited and the shorter is the HBT rise time. Therefore we get [146]

$$1/T = 1/t_{QD} + p. \tag{4.6}$$

Since the pump rate is proportional to the measured injection current, determining the rise time for different currents allows for the extraction of the lifetime of the QD emission. Therefore two more HBT measurements have been done, with a driving voltage of 5.6 V and 6.2 V, respectively. The results are shown in Figure 4.12(b,d). Fits with Equation (4.5) yield the values of $g^2_{\mathrm{IRFcorr}}(0) = 0.45(7)$ and $g^2_{\mathrm{IRFcorr}}(0) = 0.31(22)$, respectively. Since the filters have been slightly adjusted for each HBT measurement, the

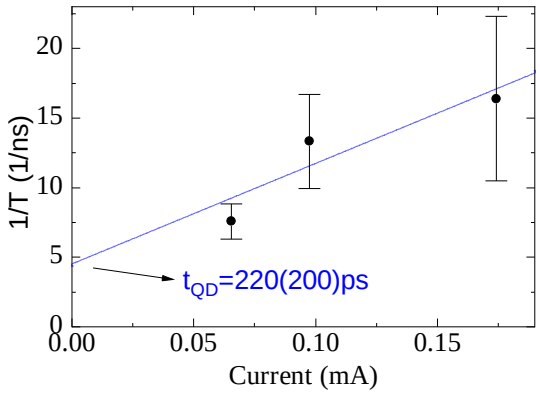

Figure 4.13: Determination of the exciton lifetime from the injection current and the HBT rise time. The straight line is a linear regression.

obtained values of $g^2_{\mathrm{IRFcorr}}(0)$ cannot be compared with each other. But the inverse of the HBT rise times are plotted in Figure 4.13 over the injection current. Their uncertainty $\delta_{1/T}$ is obtained through the ratio to the rise time $1/T \times \delta_T/T$. A linear fit gives a value of $1/T = 4.5(4.1)\,1/\mathrm{ns}$ at zero injection current. Therefore the QD exciton lifetime amounts to $t_{\mathrm{QD}} = 220(200)\,\mathrm{ps}$. This is within the range of PL lifetimes from similar dots [64, 145] and underlines the potential of *a*-plane QDs for high throughput, electrically driven single photon sources.

4.5 Temperature dependence

In order to confirm that the studied emission peak originates from a QD and not a defect, its temperature dependence is studied. In case of a defect one would expect to observe a discontinuous energy change at a certain temperature where the thermal excitation would overcome the exciton binding energy [137, 147]. This would result in two peaks at this temperature. In particular an exciton bound to a donor in InGaN would be expected to show an activation energy below the value for GaN of 17 to 12 meV [148]. The spectra taken with a fixed voltage of 6.7 V are plotted in Figure 4.14. It can be seen that the dot spectrum becomes dimmer and shifts to longer wavelength with increas-

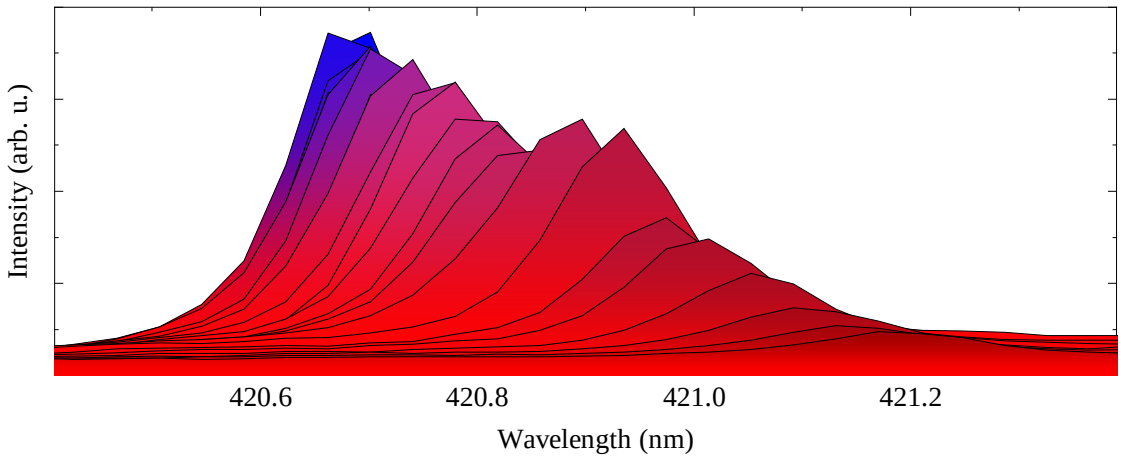

Figure 4.14: Temperature dependence of the HBT QD spectra for a fixed voltage of 6.7 V.

ing temperature. This latter behaviour is due to the well known bandgap shrinkage of semiconductors with increasing temperature. The peaks were fitted with a Gaussian to extract the peak parameters. It should be noted that the parameters depend on both current and voltage, of which only one could be fixed, such that the observed trends might deviate from those commonly seen in PL. The obtained QD peak position is plotted in Figure 4.15(a). An improved Varshni fit follows the data well [149]

$$E(T) = E_0 - S\langle\hbar\omega\rangle \cdot \left(\coth\left(\frac{\langle\hbar\omega\rangle}{2kT}\right) - 1 \right) \tag{4.7}$$

with the emission energy E_0 at 0 K , the mean phonon energy $\langle\hbar\omega\rangle = 12.2(4)$ meV and the dimensionless coupling parameter $S = 0.73(4)$. No discontinuity can be seen from the peak position, which should appear within that temperature range for the activation energies given above. So it can be concluded that the emission peak originates from a QD. This is underpinned by the fact that no sharp defect emission lines are known in the wavelength range [150].

In Figure 4.15(b) the line width of the HBT QD exciton is shown. As it might be expected, it does increase with rising temperature due to interactions of the exciton with acoustic phonons, whereas optical phonons can be excluded because of the large excitation energy of 92 meV [151]. A linear fit yields an increase of 2.8 μeV/K. This is on the lower side of reported values for InGaN QDs, ranging between 10 μeV/K and 100 μeV/K [63, 137, 152]. An activation energy with a Boltzmann term has not been observed for this particular QD. This might be the case at higher temperatures at which the QD is too dim to be observed. The linewidth at 4 K is broad compared to the transform limit given by $\hbar/t_{\mathrm{QD}}$ [153]. This is commonly observed in nitride QDs and is attributed to spectral diffusion happening on a much faster time scale than the integration time [100, 154–156].

Figure 4.15(c) shows the temperature dependence of the normalised integrated intensity of the HBT QD in black. At low temperature, it shows constant intensity up to 50 K

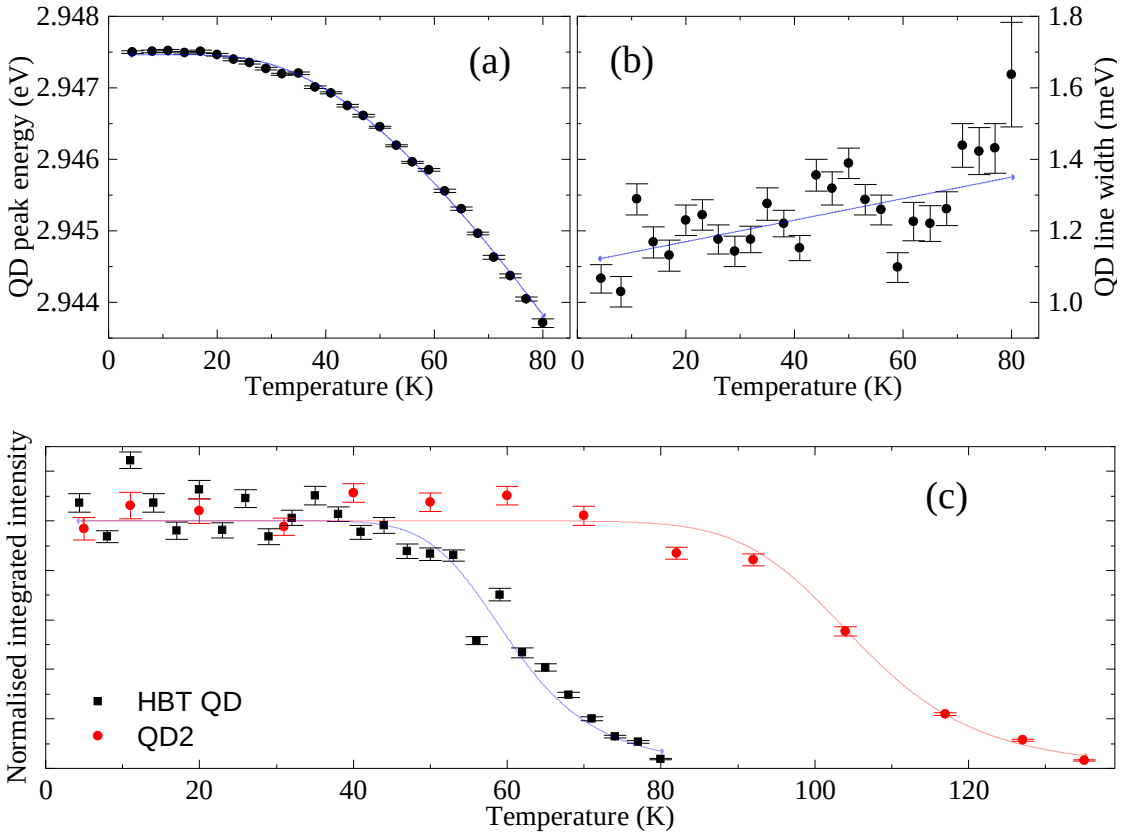

Figure 4.15: Temperature dependence of parameters of the HBT QD for a fixed voltage of 6.7 V. (a) QD peak energy. The line is a fit with an improved Varshni function (Equation (4.7)). (b) Linewidth with a linear regression. (c) Normalised integrated intensity, also for a second QD (red). Its driving voltage was fixed to 6.2 V. Fits with Equation (4.8) serve as a guide to the eye.

and then decreases to zero just above 80 K, respectively. The data is fitted with a single channel Arrhenius-type model [137]

$$I(T) = \frac{I_0}{1 + A \times \exp(-E/kT)} \tag{4.8}$$

with the intensity I_0 at low temperature, the amplitude $A = 8000(6000)$ and the activation energy $E = 46(4)$ meV. Thus, operation at temperatures higher than the boiling temperature of nitrogen at 77 K seems achievable with electrically excited non-polar InGaN QDs. Indeed, a second QD was found to emit up to 130 K, with a constant intensity up to 90 K. Its Arrhenius activation energy was found to be $E = 124(11)$ meV.

Unfortunately, single-photon emission could not be tested as the intensity was too dim. However, the potential for elevated temperature operation has been shown in PL studies of similar *a*-plane InGaN dots, achieving single-photon operation up to 220 K [63]. An important factor could have been etching the planar sample into approximately 200 nm narrow pillars. This might enhance the extracted light intensity through guiding effects, decrease the QW background by reducing its spatial extend below the diffraction limit of the emitted light and increase the temperature stability by altering the phononic structure. To harness those advantages in EL too one needs to find a way to contact the top p-layer. A solution could be filling up the etched volume with an insulating material on which the p-contacts can be patterned [9, 56]. This might however undo in parts the guiding effect and also the effect on the phononic structure. More importantly, if distributed Bragg reflectors are used on both sides of the QD layer to build a cavity and thus enhance the extraction, the lateral confinement would be reduced, if not destroyed depending on the refractive index of the filling material. Another solution consists of pillars with fins through which electrical injection can take place [157]. Both methods require careful and systematic study in the future.

4.6 Challenges

The path to a commercially viable InGaN single-photon source with real-world applications is still long. Three major obstacles are in the way: The contaminating background emission of the QW, deterministically triggering single photons and the low extraction efficiency of the emission. The first two issues are commented upon below, the third covers a much larger field.

4.6.1 Single-photon emission at elevated temperature

A big hurdle on the way to practical applications presents not only the high temperature operation as previously discussed, but more importantly a high purity of single-photon emission. An easy improvement step is to use samples containing only a single QD layer instead of 5 layers as done here for a increased QD density. For further reduction of the QW intensity, different growth parameters must be investigated, or post-growth processes such as etching narrow pillars, as explained previously. A more advanced method would be to use oxide mesas above or below the active layer to restrict the current flow through a much smaller area, therefore reducing background emission even further compared to pillars, similar to [158]. To make matters worse the QD-to-QW ratio decreases with temperature as shown in Figure 4.16. Here, an perfectly sharp filter with the width of the QD full width at half maximum (FWHM) has been assumed. The HBT QD shows a linear decrease with increasing temperature whereas the second dot on the right decreases more strongly at lower temperatures. The uncertainty is obtained through propagation from the peak parameters and is proportionally quite large at lower temperatures due to the deviation of the line shape from a Gaussian. At a temperature of 80 K which would allow for cooling with liquid nitrogen the QD-to-QW ratio were 1

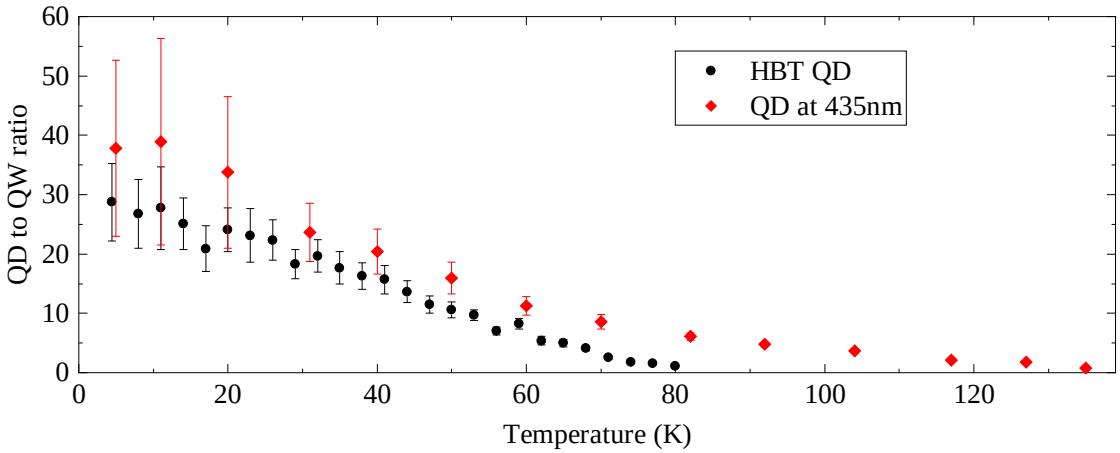

Figure 4.16: Ratio between QD and QW emission for a width of one FWHM as a function of temperature of the HBT QD and the second QD.

and 6 for the HBT QD and the second dot, compared to 29 and 38 at 4 K, respectively. This would not even allow in an HBT experiment to reach $g^2(0) = 0.5$, the limit of pure two-photon emission. However, there might have been a voltage setting with a more favourable QD-to-QW ratio.

4.6.2 Pulsed excitation

Furthermore, for a single-photon source to be practically operable the stream of photons must be pulsed, where the distance between subsequent photons must be much larger than their lifetime. This is not given for constant current excitation, therefore a train of electrical pulses must be used. Since the lifetimes of non-polar InGaN QDs are much shorter than 1 ns, they demand the use of electrical frequencies in the order of a few GHz to form pulses with a width much shorter than the lifetime. The transmission of such high frequencies without large losses can only be handled with coaxial cables, for example SMA cables. Unfortunately, the feedthrough cables in this setup consist only of twisted pairs of isolated wires. Nevertheless, the attenuation has been tested. The EL emission was probed as a function of the frequency. A function generator (Model TG302) has been used to generate a stream of square pulses with a 7.8 V peak-to-peak amplitude, a 2 V offset voltage and a 50% duty cycle with a carrier frequency between 20 Hz and 2 MHz. The EL generated with those pulses was recorded with the CCD and is shown in Figure 4.17(a). At a frequency of 20 kHz, the EL intensity drops by half, as can be seen more clearly in panel (b). Therefore, to excite QDs with GHz pulses, clearly coaxial wires are needed. Additionally, for experiments below room temperature - which makes it easier to identify bright QDs with a high QD-to-QW ratio- there is an additional constraint of finite cooling power of the cryostat. The AttoDRY800 is specified with a cooling power of approximately 100mW. Thus the heat transferred by the shielded wires for pulsed excitation must not be larger than a few tens of milliwatt to allow for the sample to be cooled down. For example 1 m of a stainless steel coaxial

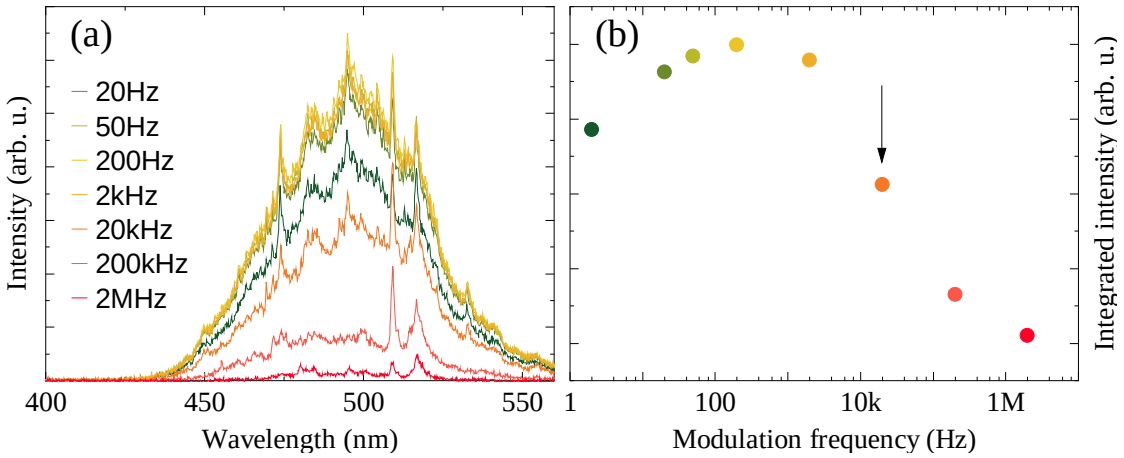

Figure 4.17: Pulsed EL for different excitation frequencies. (a) Spectra. (b) Integrated intensity with an arrow marking the 50% decrease around 20 kHz.

cable SS-UT86 connecting to a surface at room temperature and one at 4 K would result in a heat conduction power of 10 mW. Those stringent requirements explain why in the nitride QD research area there is only one report on pulsed single-photon EL, and only at room temperature where the cooling restriction does not apply [55]. For the more advanced research on arsenide QDs, pulsed single-photon emission at low temperature was achieved by means of flexible mini coaxial cables [159] or a probe needle [160].

Design of new cryostat lid

Therefore, a new cryostat lid was designed and built. The 3D model can be seen in Figure 4.18. It consists of a aluminium ring with octagonal outer side faces, allowing up to 8 feedthroughs, and a top plate with a 1 mm thick fused silica window for optical access. The feedthroughs could be of electrical nature or also optical fibres, for example for side excitation. 4 RF feedthroughs have been soft-welded to stainless steel plates (242-SMAD50, *Allectra*, transmitting frequencies up to 6.5 GHz). It was tested and found to be vacuum-tight down to the usual pressure of approximately 5×10^{-5} mbar at 4 K. Also a copper heat shield with a larger diameter was built to allow for more space to connect the cables to the sample. It is also used for current DC experiments to avoid cables touching the heat shield leading to local heating and therefore increased position

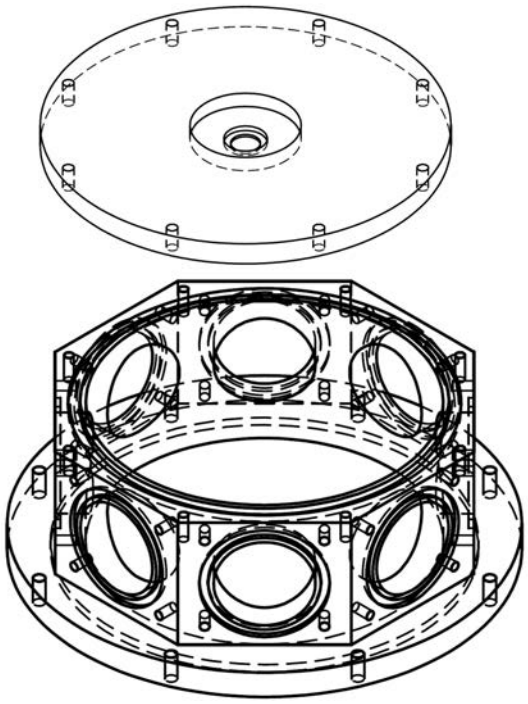

Figure 4.18: Aluminium cryostat lid compatible with the AttoDRY800 with space for up to 8 feedthroughs.

drift.

To decide on the exact nature of the contact between the coaxial cables and the sample one has to satisfy two conditions. Firstly the pulses should broaden in time the least possible, and therefore be guided as much as possible in a coaxial cable. Secondly, the area of interest needs to be movable in relation to the optical axis of the setup on a scale of millimetres to change between devices and on the scale of a few hundred micrometres to scan the device. The rough movement has to be done by either the already installed piezo-motors or some other motor being able to reliably operate at a minimum temperature of 4 K. The latter option might run into troubles with the limited space and also cost restrictions. But the piezo motors are very sensitive to shear forces so that the coaxial cables cannot be directly attached to it. One option could be to use a PCB chip fixed to the cryostat with a resonant waveguide connecting the coaxial cables and the wedge bonds to the sample, leaving only approximately 6 mm non-coaxial path length (the wedge bonds) which should broaden the RF pulses negligibly. Additionally,

one has to think of a structure to allow for transport of the bonded sample and the PCB chip between bonding machine and cryostat. An alternative way to contact the sample would be a probe needle [160], allowing for contacting all the samples as compared to a maximum of four. On the fine moving scale of 100 μm either the objective mounted on a piezo motor could be used to scan, or a so-called 4f-setup. The latter has been realised due to its cost advantage (see subsection 3.2.4). For the next generation QD-LED sample a program has been written in Labview and Matlab to scan the sample and automated finding of bright QDs with low QW background. It has already been successfully used in chapter 6 (see Figure 6.1 for an example map).

A practical point for future pulsed excitation is the need for impedance matching to ensure efficient excitation and maintaining a short pulse duration. This can be realised with a resistor and a capacitor in parallel to the QD diode [161, 162].

Several groups simulated how short a pulse must be —given a mono-exponential exciton lifetime τ— to be able to record a low $g^2(0)$ of a true single photon source. Usually, they focused on resonant excitation and used a Gaussian shaped excitation pulse with width T. Results have been extracted from the following publications and plotted in Figure 4.19 [47, 163–165]. A relation of $g^2(0) \approx \times 0.3T/\tau$ is visible for low

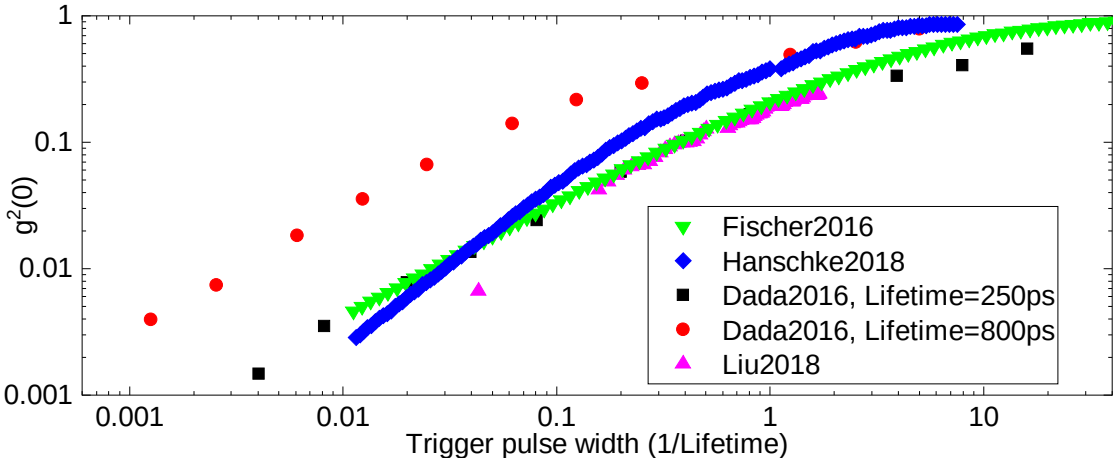

Figure 4.19: Simulation of the dependence of $g^2(0)$ as a function of the ratio between excitation pulse width and the transition lifetime T/τ for resonant excitation. Data extracted from following publications [47, 163–165].

T/τ. Therefore, for a $g^2(0) \approx 0.1$ one needs a ratio between the pulse width and the transition lifetime of 0.3, for $g^2(0) \approx 0.01$ a ratio of 0.03. For a lifetime of 500 ps this gives excitation pulse widths of 150 ps and 15 ps, respectively. Those values are quite short from a technological point of view. And one has to keep in mind that those simulations do not include effective pulse broadening caused by incoherent excitation schemes like electrical injection, which increases the $g^2(0)$ even further. Therefore, future experiments on non-polar nitride QDs with the aim of applicability should focus on dots with long transition lifetimes.

4.7 Conclusion

The electrically excited emission of highly polarised single photons from a non-polar QD was demonstrated for the first time. The polarised emission was studied in more depth for more than 70 QDs. It was shown that the achieved degree of linear polarisation of more than 50% of the QDs having a $DOLP > 0.9$ was superior to similar studies on strain engineered *c*-plane QDs. A preliminary study of the polarisation angle distribution showed a spread of 75% of the QDs within $\pm 10^\circ$, which ranks between the two studies of strain engineered QDs. However, imperfections in the setup might exaggerate the spread. The injection current into the QDs was found to be less efficient than into the QW for some dots. More work needs to be done to understand this behaviour. Three biexciton-exciton pairs could be identified with a small biexcition binding energy ± 3 meV. Comparing these values with simulations, those values could indicate a small QD height smaller than 2.5 nm. DC electrical excitation of a QD yielded a second order correlation function value of $g^2(0) = 0.18(18)$ after correction for the instrument response function of the measurement setup. This unambiguously demonstrates single-photon emission. The dot was found to emit up to 80 K, a second QD even up to 130 K. However in the future, for higher temperature single photon EL, the obstacle of the decreasing QD-to-QW ratio with increasing temperature has to be tackled. Pulsed exci-

tation at GHz frequencies also presents a great engineering challenge.

5 Electro-optical investigations of the lateral dipole moments of non-polar InGaN quantum dots

5.1 Introduction

Nitride quantum dots grown on a non-polar crystal plane could be naively thought of as being free from an in-built electric field, in contrast to those grown on the polar plane. However, only the crystal plane itself is non-polar, whereas the same is not necessarily true for dots, as they are exposed to the polar *c*-direction through their facets. These are much smaller compared to their base area, owing to the lens shape of the QDs, as evidenced by AFM measurements before capping the QDs [96]. With this geometry in mind, one would expect that nitride QDs grown on a non-polar plane should exhibit an in-built field along the *c*-direction and none in the *m*-direction. Indeed, it has been calculated by Patra and Schulz that the electrostatic built-in potential of a lens-shaped $In_{0.2}Ga_{0.8}N$/GaN QD drops along the polar direction of the QD [166]. This produces an in-built field. Due to the symmetry in the *m*-direction, there is no drop of the built-in potential and hence no electric field. Particularly interesting is the fact that the potential arising from the second order piezoelectricity is of similar magnitude to the potential stemming from the first order one, and that they are opposed to each other. This leads

to a reduced built-in potential drop along the polar QD axis. The authors expect that the dot geometry and base anisotropy, along with the indium content, may have a large influence on the magnitude and sense of direction of the potential drop, because the second order piezoelectric polarisation is partially linked to shear strain. Thus, if one were able to measure the lateral in-built field, one might be able to identify the indium content and the size of single QDs. Knowledge of these parameters is highly desirable for a more accurate understanding of the dots.

In order to extract the in-built field, an electric field has to be applied laterally across a single QD. There are several successful reports on this topic. Most of them focus on InGaAs/GaAs QDs [167–172], but there are also two papers on CdSe/ZeSe QDs [173, 174] and a single one on a polar *c*-plane InGaN QD from our group 15 years ago [175]. To apply a lateral field, the majority of reports used two Schottky contacts fabricated on the sample surface separated by a gap of a few micrometers [167, 168, 170, 172].

One very interesting aspect of these experiments is the observation of a substantial linewidth broadening [167, 169, 174, 175]. This has been attributed to carriers tunnelling out of the dot on the time scale of a few tens or hundreds of fs, leading via the Heisenberg uncertainty principle to a broadening of the dot line. A simple semi-classical model has previously been used to estimate the increase of the linewidth. It will be described in detail in section 5.6. It depends on the QD size and potential confinement depth along the direction in which the electric field is applied. The so-obtained equation can be used to fit the data and to extract the two parameters. These are of high interest as they have a large influence on the properties of a QD and are difficult to determine with other methods. This chapter is motivated by this insight to find out more about the parameters of *single* QDs.

5.2 Device fabrication and electrical properties

Following the majority of reports, we used Schottky contacts with a gap in between to apply a lateral field across the QD layer, which is close to the sample surface. Two opposing Schottky contacts have the benefit of blocking the leakage current for a small bias. Ni/Au contacts have been chosen as they resist HF etching and because of their established use in high voltage Schottky diodes [176–178]. Two different kinds of electrode patterns have been designed. The first type consists of two electrodes which have the shape of an L with an arm length of 140 μm and contact pads at opposite ends. The gap between two L's was varied for different devices between 0.5 μm, 1 μm and 2 μm. The arms were aligned to the *c*- and *m*-direction. The idea behind this design was to be able to apply a field along both crystal directions with just two contacting wires. This allows to study more devices as the number of contact wires is limited to 12 due to the number of pads on the interfacing PCB chip as well as the number of cable feedthroughs into the cryostat. An example of an L-shaped device is shown in Figure 5.1(a). The second device type consists of four electrodes arranged around a free square with a side length of 5 μm or 8 μm. The idea was to find QDs in the middle of the square where the electric field is homogeneous and find out the relevant parameters in both in-plane directions of the *same* QD. Indeed, with a suitable model one could also apply voltages

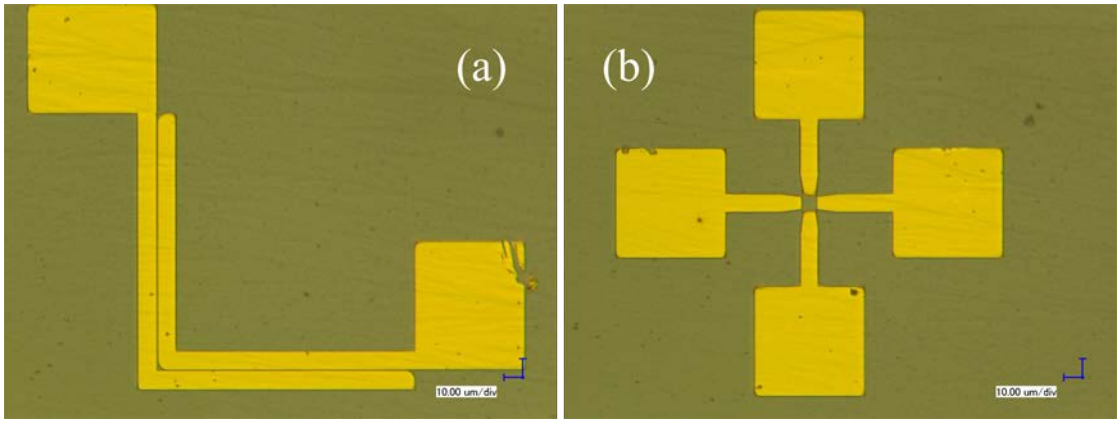

Figure 5.1: Microscope photos of the designed devices. (a) L-shaped device with a gap of 0.5 μm. (b) Square-shaped device with a gap of 8 μm.

to all four contacts such that the electric field in the middle of the device rotates over 360° and samples the in-built field in 2D [179]. An example of the square device is shown in Figure 5.1(b). However, this design could not be tested due to instability of the sample under thermal cycling.

The chosen sample contains a single QD layer 20 nm below the surface, grown via the Q2T method. The GaN layers above and below became unintentionally doped with a oxygen donor concentration of approximately $5 \times 10^{16}\,\mathrm{cm}^{-3}$. The sample had been previously investigated with μPL excited via two-photon absorption, showing single lines with a peak brightness of up to 500 counts/s. The devices on the sample surface were fabricated with electron beam lithography by John Jarman in the Cambridge group. The electrodes were made via evaporation of a bi-layer of Ni/Au with thicknesses of 20 nm and 80 nm, respectively. They were not annealed. The electrodes exhibit an angle of 6 ° to the *c*- and *m*-direction, determined through the observation of [*c*]-oriented asymmetric growth pits under an AFM. The approximate crystal direction can be observed in the PL setup through the stripes along [*c*] visible in a optical microscope photo (see Figure 5.1). The sense of the *c*-direction was attempted to be determined from the AFM scan. In this regard however, it was inconclusive. Convergent-beam electron diffraction, which is a transmission electron microscopy method, would have been needed along with a many-beam scattering simulation to interpret the diffraction pattern. Due to these complications the sense of the [*c*]-direction could not be established. The more stable, second setup version was used (see Figure 3.2(b)).

The sample was glued with thermally conductive silver paste to a copper sample holder. A commercially available PCB chip[1] surrounding it enabled electrical connections between the sample and DC cables feeding into the cryostat. The PCB was connected to these DC cables by soldering insulated copper wires with a diameter smaller than 1 mm onto the outer contacts of the PCB and pins on the other end of the wires. To connect the PCB to the sample, wedge-bonding was used with an approximately

[1] Produced by AttoCube matching their copper sample holder.

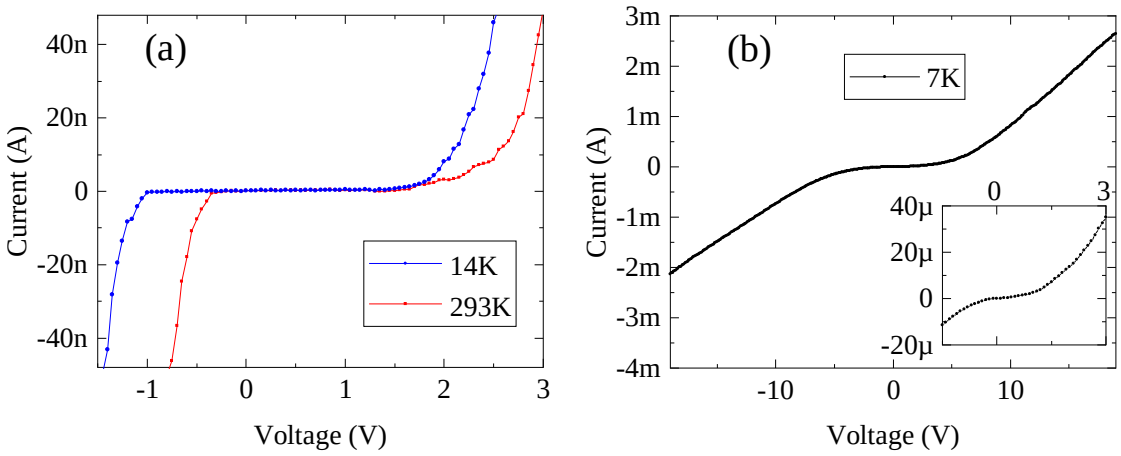

Figure 5.2: IV curves of the used device. Point-average of 32 with automatically adjusted acquisition times. (a) At 293 K and at 14 K before the μPL experiments described in the following. (b) At 7 K after the μPL measurements. The inset shows the direct comparison to (a) with the same voltage axis range. All measurements were carried out at a pressure of approximately 10^{-4} mbar.

25 μm-thick aluminium wire[2]. Six L-shaped devices were connected. The leakage current dependence on the applied voltage was measured with a source-meter unit (Keithley 236). The IV curve of one device with a 2 μm gap, measured at room temperature and at 14 K, is shown in Figure 5.2(a). Around 0 V, there is a plateau of negligible current visible with a width of approximately 2.5 V. This is the influence of the two Schottky diode electrode that oppose each other such that they block all current. Surprisingly, the IV curve shifted by 1 V to negative bias at 14 K compared to room temperature. The reason for this behaviour could not be identified. For these IV curve measurements, the current was limited to 50 nA in order to not damage the devices. After the μPL measurements described below, the IV curve of the same device was measured over a larger bias range of $\pm$20 V, shown in Figure 5.2(b). For larger voltages, the current increases linearly. This points towards Ohmic leakage pathways that become activated. The inset shows the direct comparison to the IV curves before the μPL measurements. The leakage current increased by 3 orders of magnitude. This is an issue that needs be addressed

[2]Gold wires with better conduction properties proved to be not rigid enough to cover the distance of in some cases almost 1 cm.

for future experiments.

5.3 Electric field simulations

In order to be able to relate an applied voltage to the resulting electric field in the QD plane, a 2D simulation has been carried out with the program *NextNano++*. It solved the Poisson equation iteratively along with the current equation. One might think that an estimate might be obtained with a direct calculation, as it can be done for a vertical Schottky diode with the full-depletion approximation. However, the lateral nature of the device complicates the situation beyond intuitive calculations. In Figure 5.3(a) the simulation device geometry is shown. The grid in the lateral and vertical direction is set to 20 nm and 10 nm, respectively. Convergence was successfully tested for different ratios of vertical to lateral resolution. The (unintentional) doping density was set to 5×10^{16} cm^3. Although the measurements were performed at 4.5 K, the simulation was carried out for room temperature as it did not converge otherwise due to instabilities. The results are therefore only an estimate[3]. The mobility of n-doped GaN was estimated through a phenomenological formula to be 810 cm^2/Vs [182]. Literature values of the barrier height of Ni/n-GaN Schottky diodes measured at 300 K depend on the fabrication quality and post-processing methods and scatter between 0.6 eV to 1.2 eV [183–187]. Here, the often cited value of 0.8 eV was chosen.

In Figure 5.3(b,c) the vertical and the lateral component of the electric field are shown at the depth of the QD layer of 20 nm respectively. The voltage applied to the right contact ranged between -10 V and 10 V. The vertical electric field is strongest directly under the contacts due to the depletion region, but is negligible elsewhere. For the lateral electric field, it is the opposite: close to the electrodes, the field peaks and then decreases

[3] It should be noted that only a few of the various reports on lateral fields applied across QDs contain an actual simulation compared to a rough estimation. And even of these, none state the temperature at which the simulation was done, neither in the paper nor in the PhD thesis if applicable [169,180,181], therefore pointing to room temperature.

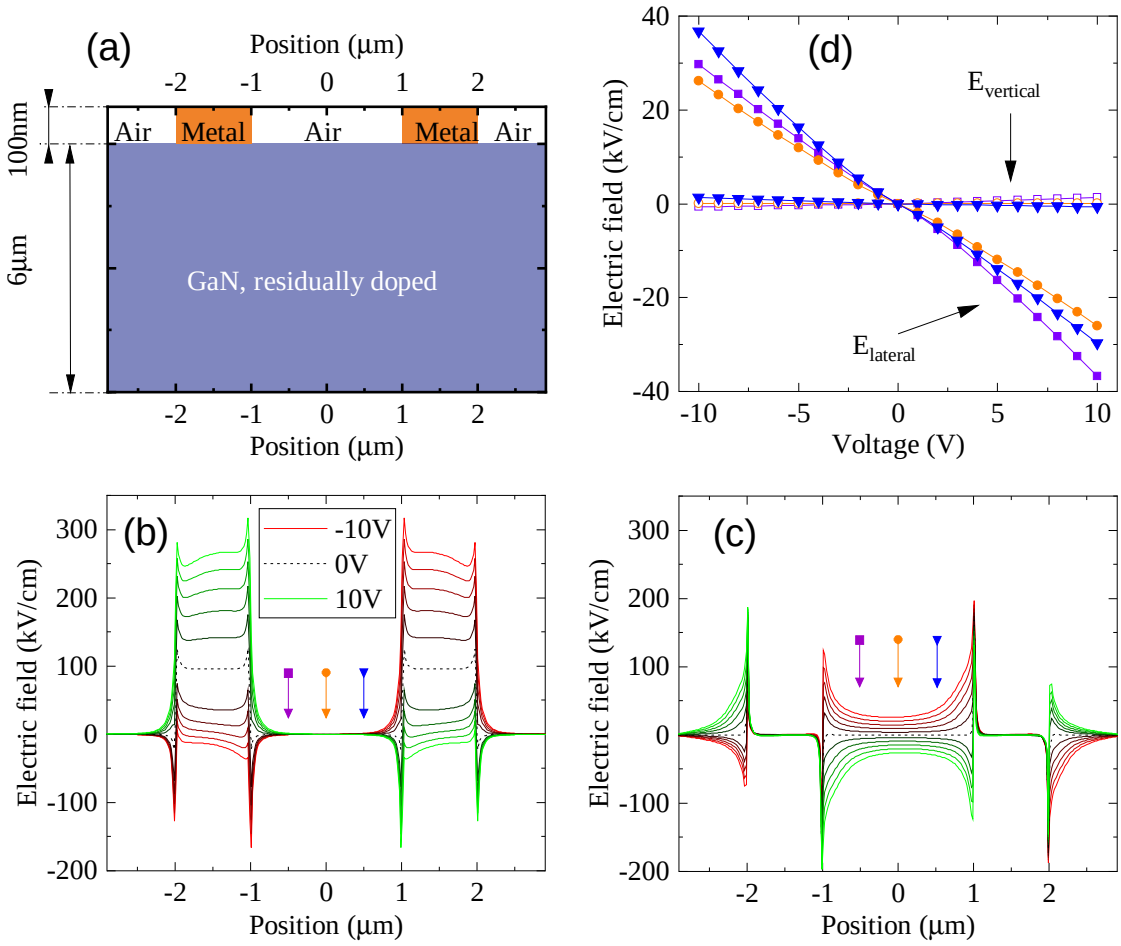

Figure 5.3: (a) 2D simulation structure. The vertical direction is not drawn to scale. (b) Vertical electric field component at 20 nm below the sample surface, for voltages ranging between +10 V and -10 V with a step of 2 V. The zero bias line is dashed. (c) Same for the lateral electric field component. (d) Voltage dependence of the lateral and vertical electric field component for positions mid-gap and 500 nm either side at a depth of 20 nm below the sample surface. These positions are marked in (b) and (c) with colour- and shape-coded arrows.

considerably towards the centre of the gap, so that the field which a QD experiences depends on its position relative to the electrodes. However, it must be remembered that the dots are optically excited by means of an 800 nm-laser through two-photon absorption, giving an approximate spot diameter of 1 μm. If the laser spot partially overlaps with one of the electrodes, the light is partially reflected and does not contribute to the excitation. Furthermore, the reduced power impacts the PL intensity quadratically through the non-linear dependence of two-photon excitation. Therefore, it is safe to assume that

in PL, no bright dots are observed that are closer than 500 nm to the electrodes, for a laser power typically saturating QDs. This means that the observed QDs lie in a region where the lateral and vertical electric field components are almost constant.

In Figure 5.3(d), the relation between the electric field and voltage can be seen for a position mid-gap and 500 nm either side. For the lateral field, the relationship is close to linear and varies by $\pm 15\%$ for the different positions. In comparison, the vertical field is negligible, such that with this device design a lateral electric field can be applied to a QD located approximately mid-gap. For the experiments in the next section, the conversion factor between an applied voltage and the resulting lateral electric field was calculated for a fixed bias as the mean over the field at positions in between ± 500 nm of the mid position. The relation was extended to higher voltages through linear extrapolation for data points with $|V| > 2$ V.

5.4 Laser power dependence of QD shift

PL studies have been carried out under two-photon-absorption on single QDs at 4.5 K on an L-shaped device. To find dots, the sample was moved with the piezo positioners such that the laser scanned through the gap between the electrodes, without an applied bias. Once a bright QD was found, and its spatial position optimised, a range of voltages was applied and spectra were taken concurrently. For the first examples presented, this was performed manually, later it was automated within the main *Labview* program.

In previous reports on QDs under the influence of a lateral electric field, it was observed that the amount of the QD peak shift depends on the intensity of the exciting laser [167, 169]. The higher the laser power is, the smaller is the shift for a given electric field. This is because an increased number of carriers around a dot in the nearby QW are swept to opposite sides by the electric field and partially screen the electric field experienced by the QD. This is of concern with regard to the tunnelling effect we would like to exploit in order to gain knowledge of individual QD parameters. To check

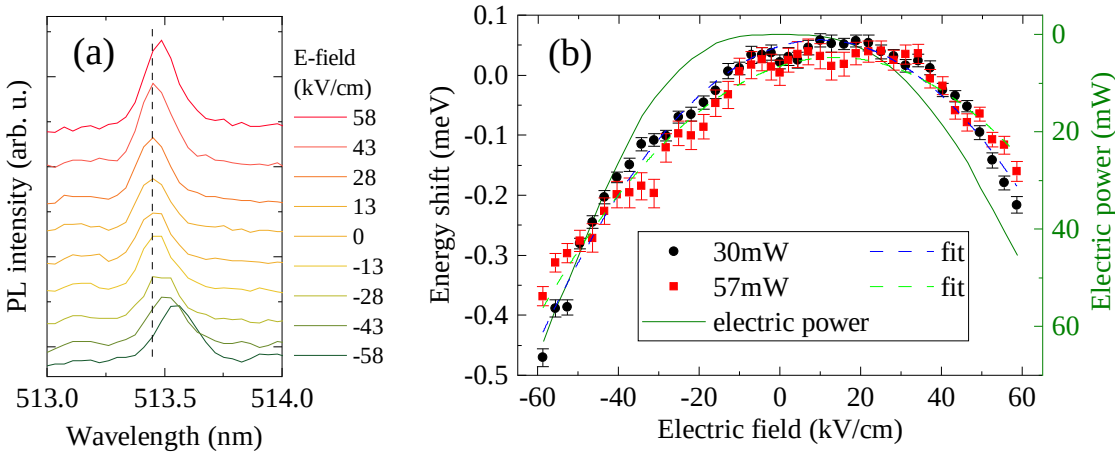

Figure 5.4: Energy shift of QD1. (a) Spectra taken at an excitation power of 57 mW. (b) Electric field dependent shift of the dot peak for excitation powers of 30 mW and 57 mW. Quadratic fits to the data are dashed, their parameters are given in the main text. The green line shows the electric power dissipated in the sample due to leakage.

the influence of an increased excitation power in our system, we studied the wavelength shift for one dot (QD1) for a power well below saturation (30 mW) and an excitation power close to it (57 mW)[4]. The voltage was varied in an opposing-staircase manner, meaning that at first a voltage of 0 V was applied, then +1 V, -1 V, then +2 V, -2 V and so on up to -20 V. Example spectra at voltages in increments of 5 V are shown in Figure 5.4(a) with increasing voltage for an excitation power of 57 mW. The dot emission at 513 nm was found between the electrodes where the electric field was parallel to the *c*-direction. It exhibited a shift to longer wavelengths for an increasing modulus of the electric field. This is shown in more detail in Figure 5.4(b) by extracting the peak energy with a Gaussian fit. The energy at zero field is subtracted.

At both excitation powers, one can see a clear parabolic shift of the peak to lower energy. The data is almost identical for both laser powers, which means that screening is negligible and that the dot sees the full amount of the applied field. This is different to previous reports using arsenide dots [167, 169]. To draw a fair comparison, one has to take into account that the experiments described here used two-photon excitation such

[4]The two-photon excitation power density amounts to 3.8 MW/cm^2 and 7.2 MW/cm^2, respectively, assuming a beam diameter of approximately 1 μm.

that a doubling in laser power leads to a four-fold increase of the emission intensity. However, the above mentioned references used one-photon excitation, where the increase of the intensity depends linearly on the laser power. Therefore, a fair comparison of the results presented in Figure 5.4 to the arsenide references consists in comparing the energy shift for a quadrupling of the laser power: this leads to a significant change in the shift. The difference might lie in the different excitation mechanism. One could speculate that through the two-photon excitation used here, fewer carriers are injected into the QW that could screen the field.

The parabolic dependence of the QD energy shift on an electric field is well known and can be described by the parameters of the intrinsic dot dipole p with the applied field F and the interaction of the field with the field-induced dipole (see Equation (2.2)). Fitting the data yields a dipole of $p = 0.21(1)\,\text{eÅ}$ and $p = 0.22(1)\,\text{eÅ}$ and a polarisability of $\alpha = -103(3)\,\text{meV/(MV/cm)}^2$ and $\alpha = -80(3)\,\text{meV/(MV/cm)}^2$ for a laser excitation power of 30 mW and 57 mW respectively. Since the data is almost identical, the extracted parameters are also similar for both powers. The lateral permanent dipole moment is approximately 40 times smaller than the *vertical* dipole component of an InGaN QD grown on the *c*-plane [74]. Although both components are measured along the *c*-direction, this is expected, as in the case of the *a*-plane QD, only the facets face the *c*-direction. Due to the flat lens shape, their projection onto the *c*-plane is much smaller compared to the base area of a *c*-plane grown dot. In a different study on a similarly grown *c*-plane dot, the *lateral* dipole moment was surprisingly determined to be also approximately 40 times larger than the one of the dot studied here, where a much smaller value would have been expected [175]. This could point to a calibration problem of the electric field in the previous study.

The *vertical* polarisability found for the *c*-plane grown InGaN QD was 2.5 times smaller than the lateral one obtained here [74]. This could be due to a smaller dimension of the QD in the vertical direction: its height was determined to be 2 nm through semi-empirical tight-binding calculations, whereas for the QD studied here, a minimum

diameter of approximately 6 nm will be deduced in the following section. It has been found both experimentally and through calculation that the polarisability increases for larger QDs [188], though it also depends on the ionisation energy [189]. The *lateral* polarisability of the *c*-plane grown InGaN dot was surprisingly large - 10 times larger than the lateral polarisability found for the non-polar dot. Furthermore, the size of the same polar dot was deduced to be approximately 2 nm [175], which is smaller than the diameter of the non-polar dot obtained with the same method. Again this could point to a problem of the electric field calibration in the previous study. On the other hand, the similarly determined confinement potential of the *c*-plane grown QD was 3 times shallower than of the non-polar dot, which might also explain the large difference.

5.5 Thermometry

In Figure 5.4(b) the discussed shift of the dot peak energy is contrasted with the approximate dissipated power in the total device on the right axis, calculated through the product of applied bias and leakage current. This is justified by the fact that the IV curve is linear from the points where the blocking character of the pair of opposing Schottky diodes fades. It can be seen that the dissipated power curve is roughly similar to the QD shift curve. But it is not parabolic and is not as much shifted to positive fields. Therefore, it is likely that the observed QD shift is due to the applied electric field and not due to heating.

To further strengthen this argument, we measured the local temperature of the sample by means of μPL with and without a large applied bias of 30 V, which produces a leakage current of several mA. In the sapphire substrate, there are Cr^{3+} ions, making it a highly dilute Ruby crystal. It emits two lines at $R_1 = 694.2\,\text{nm}$ and $R_2 = 692.9\,\text{nm}$ at room temperature. These originate from the transition of excited electrons from the two first excited states to the ground state [190]. Their intensity ratio R_1/R_2 reflects the Boltzmann distribution because population transfer between the excited states is very

rapid compared to their decay times and can therefore be used to measure the temperature on a micrometre scale. In Figure 5.5(a), spectra taken at several temperatures at an excitation power of 2 mW of a 405 nm CW laser are presented. The two-photon dichroic mirror was exchanged for a silver mirror to send the otherwise transmitted Ruby emission to the spectrometer, and the one-photon excitation dichroic mirror was used to couple the blue laser into the system. The data points were taken by heating the sample up (globally) using the cryostat heater close to the sample, taking spectra once a steady state was achieved, and noting the temperature of the sensor below the sample. The

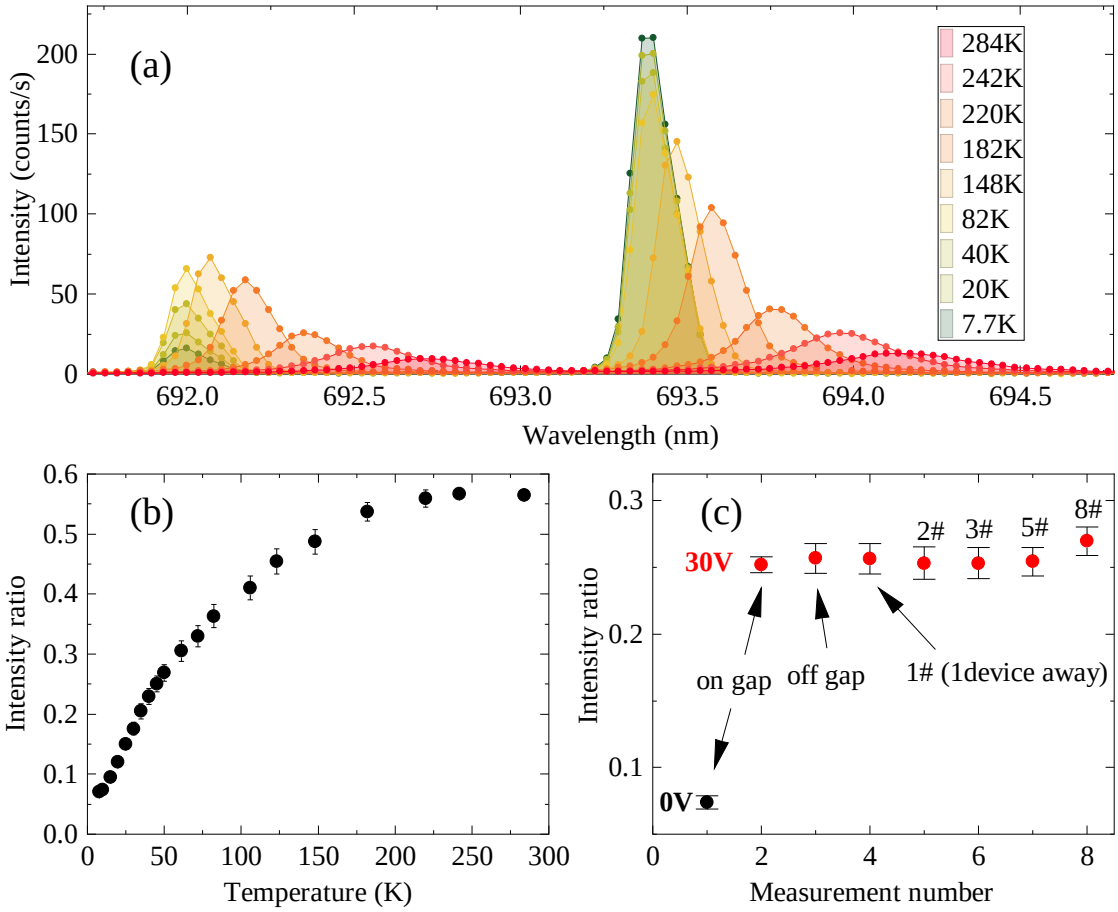

Figure 5.5: Thermometry using Ruby lines. (a) Spectra of the R_2 and R_1 lines at different temperatures. (b) Temperature dependence of the intensity ratio R_2/R_1. (c) Intensity ratio at a different position on the sample for a bias of 30 V (red marker). At the start position, where the laser is focused in the gap of the active device, the intensity ratio is measured as well without an applied bias (black marker).

peaks were fitted with Lorentzian lineshapes, and the ratio of their integrated intensity is presented in panel (b). Fitting them with a Boltzmann formula $A \cdot \exp(-T_0/T)$ results in a bad fit, which indicates that the cryostat temperature sensor was not correctly calibrated. However, the data points can be used as an approximate calibration scale. We then determine the intensity ratio with the laser focused in between the electrodes of the relevant device for zero bias. In the next step, we repeat the measurement with a voltage of 30 V at the same spot, then move the laser spot outside the electrodes, and finally a few neighbouring devices away. The intensity ratio obtained for the different laser spot positions can be seen in Figure 5.5(c). With the bias turned on, the intensity ratio everywhere on the sample amounts to approximately 0.25, corresponding to a temperature of about 45 K. By contrast, without a bias the ratio is approximately 0.07, corresponding to a temperature below 8 K. This means that the heat conductivity of GaN and sapphire is so good that the sample is heated up everywhere. A line scan between the electrodes along the gap yielded the same result.

Returning to the QD energy shifts: if these were merely due to heating, the above result would mean that all dots should show a similar shift behaviour compared to that in Figure 5.4. However, in section 5.7.2 we will encounter many dots that do not show this behaviour. For example, their energy remains constant for one voltage polarity and shifts for another. Some QDs even shift to shorter wavelengths, an effect not explainable by heating. In summary, these points clearly demonstrate that the observed QD energy shifts are largely due to the applied field and that the heating due to leakage plays, if at all, a minor role.

5.6 Electric field dependence of the linewidth

The linewidth of QD1 is plotted in Figure 5.6 for both excitation powers. It can be seen that for an increasing modulus of the applied bias, the dot linewidth increases from 0.6 meV to 0.8 meV for the lower excitation power. This is the effect observed in

previous publications due to fast tunnelling of carriers out of the dot [169, 174, 175]. It can be seen that the linewidth increases a little asymmetrically with respect to zero field. This is due to the in-built field, as evidenced by the previously discussed offset of the parabolic energy shift. As previously mentioned, the increase in the linewidth can be quantitatively understood with a simple semi-classical model. The following paragraph extends the reference of Heller et al. [169]. It models the dot in 1D as a potential trough with ionisation energy V_0 and diameter a in an otherwise constant potential landscape. Due to the position-momentum uncertainty relation $\Delta x \Delta p_x \geq \hbar/2$, the velocity v of a trapped particle with a mass m is at least as large as the minimum velocity uncertainty due to the size of the trough.

$$v \geq \Delta v = \frac{\hbar}{2ma} \tag{5.1}$$

Applying an electrical field F tilts the potential and allows tunnelling of the particle out of the trough. The tunnelling time τ can be approximated as the product of the inverse of the frequency of the particle hitting the one side wall where it may tunnel through, namely $f = v/2a \geq \hbar/4ma^2$, and the tunnelling transmission coefficient through a triangular-shaped potential obtained by means of the Wenzel-Kramers-

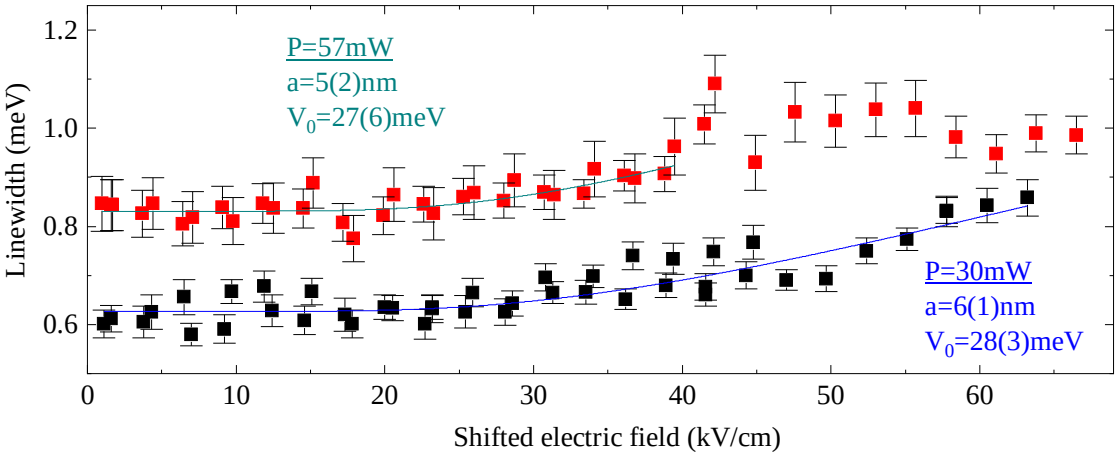

Figure 5.6: Electric field dependence of the linewidth of QD1 for two different laser powers. The field is shifted by the in-built dot field. The functional shape of the fits are explained in the main text.

Brillouin approximation [191].

$$\tau \leq \frac{4ma^2}{\hbar} \cdot \exp\left(\frac{4}{3}\frac{\sqrt{2m}}{eF\hbar}V_0^{3/2}\right) \tag{5.2}$$

The tunnelling with this characteristic time contributes to the linewidth Γ via the Heisenberg uncertainty relation $\Gamma \cdot \tau \geq \hbar/2$ [192]. Therefore, we obtain the minimum linewidth change $\Delta\Gamma$ caused by tunnelling as

$$\Delta\Gamma = \Gamma - \Gamma_0 = \frac{\hbar^2}{8ma^2} \exp\left(-\frac{4}{3}\frac{\sqrt{2m}}{eF\hbar}V_0^{3/2}\right) \tag{5.3}$$

with the zero-field linewidth Γ_0. Equation (5.3) can be used to extract the minimum potential depth and the minimum dot size in the direction of the applied field. This is done in Figure 5.6, where the field is shifted by the amount of the in-built field identified in the previous subsection. As Equation (5.3) is not symmetric to zero field, the modulus of the shifted field is taken. For the higher excitation power, the linewidth suddenly increases significantly at a field of 40 kV/cm and then decreases, therefore these data points are neglected. Only tunnelling of electrons is considered, as the mass of the holes is much larger. The effective electron mass m is estimated for a nominal indium content of 20% to be a linear interpolation between the values for GaN of $m = 0.2m_e$ [193] and InN $m = 0.042m_e$ [194]. This yields an effective electron mass of $m = 0.17m_e$. Looking at the graph, it strikes the eye that the zero field linewidth of 0.84 meV is larger at 57 mW of excitation power compared to 0.64 meV at half the power. It is likely that this is due to increased spectral diffusion as more carriers are created in the vicinity of the dot [142, 155] (see the power dependence of the spectral diffusion rate in the subsection 6.4.2 of the next chapter). Both data sets are fitted with Equation (5.3). The extracted minimum lateral QD sizes are $a = 6(1)$ nm and $a = 5(2)$ nm for the excitation power of 30 mW and 57 mW, respectively. This is plausible as AFM data measured on uncapped Q2T samples shows a bimodal height distribution, in which the smaller dots exhibit diameters

below 10 nm, which is limited by the finite AFM tip size. The extracted minimum lateral potential depths are 28(3) meV and 27(6) meV. This is a deeper confinement than reported for a *c*-plane grown InGaN QD, for which a confinement of 10 meV was extracted with the same method [175]. Measurements of temperature activated carrier escape for other polar InGaN dots yielded more comparable values of 17 meV [195] and 31 meV [196]. For non-polar InGaN QDs, larger confinement potentials have been reported: 38 meV for an *m*-plane grown dot [137] and 40 meV for an *a*-plane grown dot [63]. These larger values enabled higher temperature operation with single photon emission up to 100 K and 220 K, respectively. This would not be possible with this dot, as its potential depth is not deep enough. However, this result was obtained from only one QD. To get an overview of the spread of lateral sizes and potential depths, more measurements were carried out on a number of QDs.

5.7 Energy shifts of many QDs

In order to investigate a larger number of dots, the measurements were automated within the main *Labview* measurement program. The two-photon excitation power was fixed at 50 mW, which is close to the saturation power of most dots. The laser spot was scanned through the 2 μm gap of one L-shaped device. Every line narrower than 1 nm with a minimum peak brightness of 100 counts/s on the 300 l/mm grating was investigated with the finer 1200 l/mm grating. The integration time for every voltage step was set to 2 s as a trade-off between signal strength and drift. In the arm in which the applied electric field was parallel to the *c*-direction, 50 lines in 16 spectra were measured. Lines in the other arm were then investigated in order to obtain a similar number of measurements. But only 10 lines in 6 spectra could be found that matched the criteria. This may have been due to an elliptical laser spot size on the sample, caused by suboptimal alignment.

Surprising, none of these lines showed a systematic linewidth change with increasing voltage modulus. This might indicate that the confinement potential of these dots is

deeper than the above examined dot, so that the electrons cannot escape within the range of the applied electric field magnitude. This would be promising for the operation at elevated temperatures. However, the influence of the electric field is noticeable through systematic shifts of the peak energy of the QDs. Therefore we focus on this quantity. The observed peak energy shifts can be divided into three main groups: Parabolic behaviour, noisy behaviour without clear trend, and irregular behaviour comprising all the rest. In the following subsections, we focus on the first and the last group.

5.7.1 Parabolic behaviour

In the arm in which the electric field was parallel to the *c*-direction, there were 5 lines out of 50 which showed a parabolic peak energy shift. Two examples are shown in Figure 5.7. They feature a small inbuilt field. However, with a different sign. The results of all 5 lines are summarised in Figure 5.8, including QD1 of the previous section, marked in blue. Also, the polarisability of the one QD showing parabolic behaviour in the arm in which the electric field is perpendicular to the *c*-direction is included, and marked in red (mQD).

In Figure 5.8(a), the obtained polarisability values are plotted over the QD emission energy. One can see a trend: The higher the dot energy is, the lower is the polarisability.

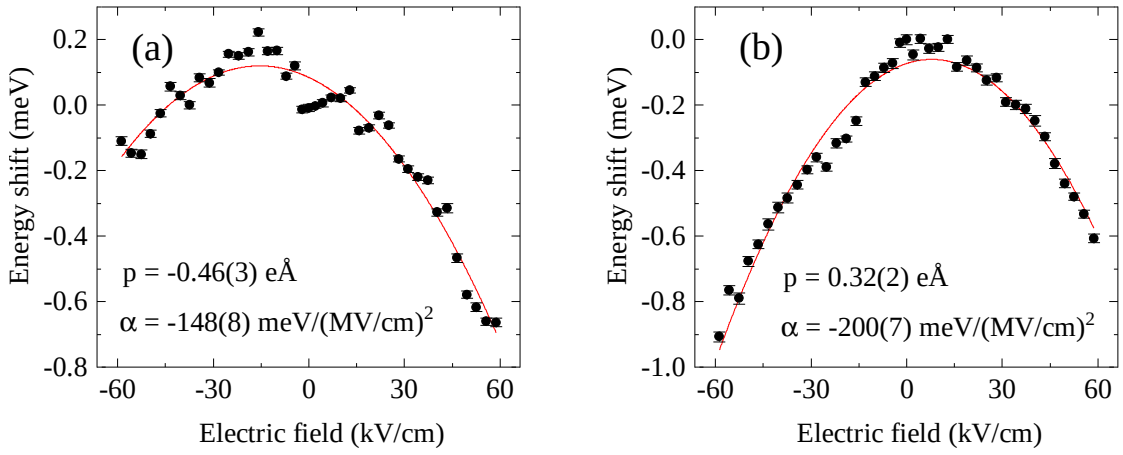

Figure 5.7: Two examples of QDs featuring a parabolic shift to lower energy for an electric field parallel to [*c*]. The energy at zero bias is subtracted.

This could be explained through the picture of the exciton binding energy. The stronger the binding between electron and hole is, the more difficult it is to separate them by an electric field, meaning the polarisability would decrease. This decrease of the polarisability with increasing QD emission energy fits with $\mathbf{k}\cdot\mathbf{p}$ simulations of non-polar InGaN QDs. They show an increase of the exciton binding energy for an increased emission energy due to a reduced indium content for the same dot height, as can be seen in Figure 5.8(c) [122]. In panel (b), the dependence of the dipole moment on the QD energy is shown. Both negative and positive moments can be seen, but the trend is not clear. It has been shown that in the special case of non-polar InGaN/GaN QDs, the second order component of the piezoelectric effect acts in the opposite direction to that of the first order component and that both components are comparable in magnitude [166]. The size, indium content, and especially the geometrical shape of a dot, may enhance or decrease the magnitude of the second order piezoelectric component. Therefore, permanent lateral dipole moments aligned parallel *and* anti-parallel to the c-direction can be expected.

In Figure 5.8(d), the polarisability is plotted over the dipole moment. The red marked dot mQD is included as its lateral dipole moment $|p| = 0.08(1)\,\text{eÅ}$ is negligible compared to most others. The graph shows a clear trend: The larger the modulus of the moment is, the larger is the polarisability. This suggests that the in-built field $F_0 = -p/2\alpha$ is of similar magnitude for all dots, similarly to a study on InGaAs quantum rings [197]. Its values are plotted in Figure 5.8(e). No clear dependency can be seen. The in-built field varies between +14 kV/cm and -15 kV/cm. The mean in-built field amounts to $F_0 = -3\,\text{kV/cm}$ with a standard deviation of 11 kV/cm. This clearly demonstrates a reduction of the in-built field by more than two orders of magnitudes compared to the vertical field component polar InGaN dots [74, 198].

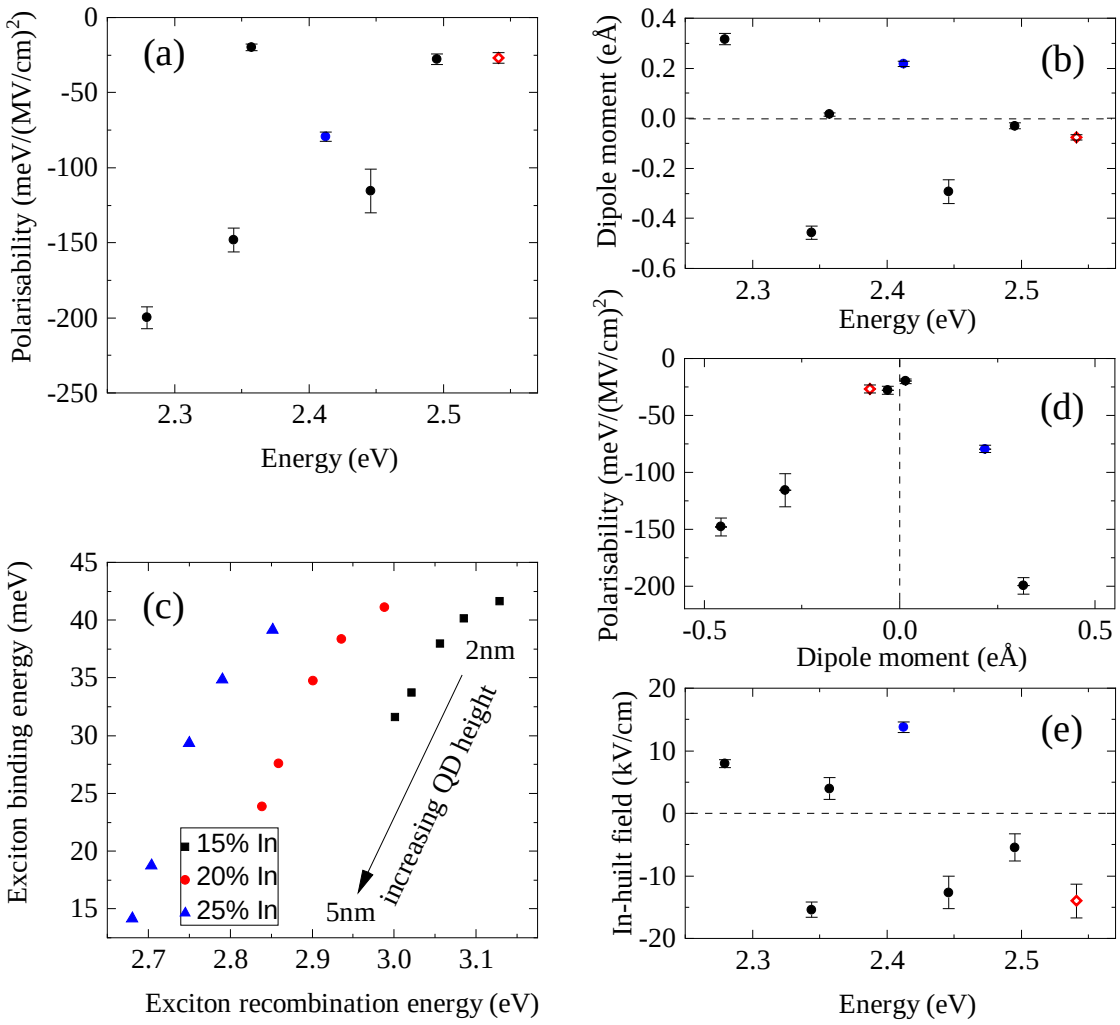

Figure 5.8: Parameters extracted from dots showing a parabolic energy shift under the influence of a lateral electric field **F**. (a) Dependence of the polarisability on the QD emission energy. (b) Dependence of the dipole moment on the QD emission energy. (c) Replotted results of **k**·**p** simulations of non-polar InGaN QDs [122]: Dependence of the exciton binding energy on the exciton recombination energy for different indium content and dot heights (2, 2.5, 3, 4, 5 nm, fixed round base of 30 nm). (d) Dependence of the polarisability on the dipole moment. The black data points are from QDs in the arm of the device where $\mathbf{F}||[c]$, including the blue data point marking the previously mentioned QD1. The square red data point marks the QD mQD found in the other device arm where $\mathbf{F}||[m]$. (e) Dependence of the in-built field on the emission energy.

5.7.2 Irregular behaviour

Instead of only showing the well understood examples, here also examples are shown which do not follow an apparent parabolic shift and remain a challenge to understand.

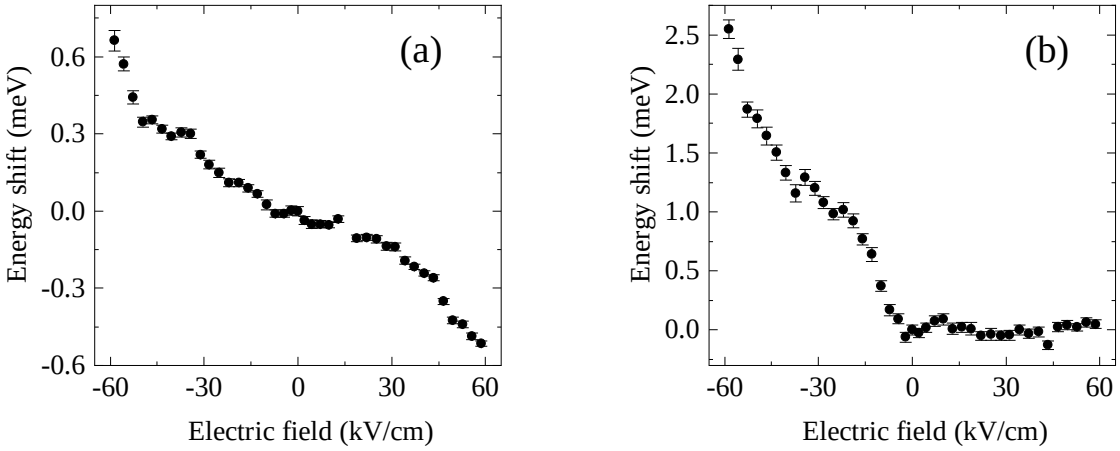

Figure 5.9: Two examples of irregular behaviour of QDs under an electric field parallel to [c]. The energy at zero bias is subtracted. (a) Linear shift. (b) Linear shift with constant energy for positive field polarity.

In the device arm where the electric field is parallel to the c-direction, apart from 10% of the dots which exhibit parabolic energy shifts and 28% of the dots which show no systematic changes within the fit uncertainty, 62% of the QDs exhibit non-parabolic behaviour. Two examples are plotted in Figure 5.9. The majority of the oddly behaving dots showed an energy increase for negative fields, whereas for positive polarity, most dots exhibited an energy decrease, resulting in an overall approximately linear trend, as shown in Figure 5.9(a). The shift magnitude ranged between 0.2 and 2.5 meV for a field of ± 59 kV/cm. A few dots show the opposite behaviour. One interpretation could be that the dot follows a parabolic behaviour with a very large polarisability, its vertex being far outside the applied electric field range. This would indicate a giant in-built field, which, however, is at odds with the naive expectation and, more importantly, with previously mentioned continuum-based strain calculations [166]. In the arm where the electric field is perpendicular to [c], the same linear shift behaviour was also observed for a stark majority of 8 out of 10 dots. The magnitude of the shift ranged between 0.3 and 4.7 meV for the same field difference. To explain this, one might think again of a large, offset parabola in conjunction with a QD axis misaligned to the electrode axis. Therefore, the projection of the in-built field would have been measured. But

in this case, the average magnitude of the shift should be much smaller than the shifts observed in the other arm, where the electric field is parallel to [c]. However, this is not the case. As previously mentioned, it might be important to note that the sense of direction of the field is arbitrarily defined with regard to the c-direction, as the sense of the latter is not known. However, this arbitrary sense of direction of the field is derived from the voltage, which is applied to the inner L-contact. The linear shift can be observed much more often to higher energy for positive voltage polarity (negative electric field polarity), for both fields parallel to the c- and the m-direction. This points to an electrical source of the irregular shifts, necessitating further investigations in the future.

In some cases, no change for a positive electric field polarity can also be seen along with a linear energy increase at negative fields, as shown in Figure 5.9(b). One might think that this could be the case of an electron-hole pair being maximally separated due to a large in-built field, thus being squeezed into opposite corners of the dot. However, in this model the sharp turn-on of the shift at 0 V is surprising, since the probability density of electron and hole are not billiard-ball hard, but smooth functions. Therefore, a gradual turn-on would be expected.

Overall, the voltage dependence of the shift of the dots reflects the underlying voltage-field dependence. The examples shown illustrate that the seemingly simple device construction leads to some unexpected behaviour. This needs closer investigation in further studies for this electric-field method to be a more quantitative tool.

5.8 Similar electric field dependence of multiple lines

As seen in the previous section, the study of a larger number of dots under the influence of a lateral electric field showed a multitude of different shift behaviours. Sometimes,

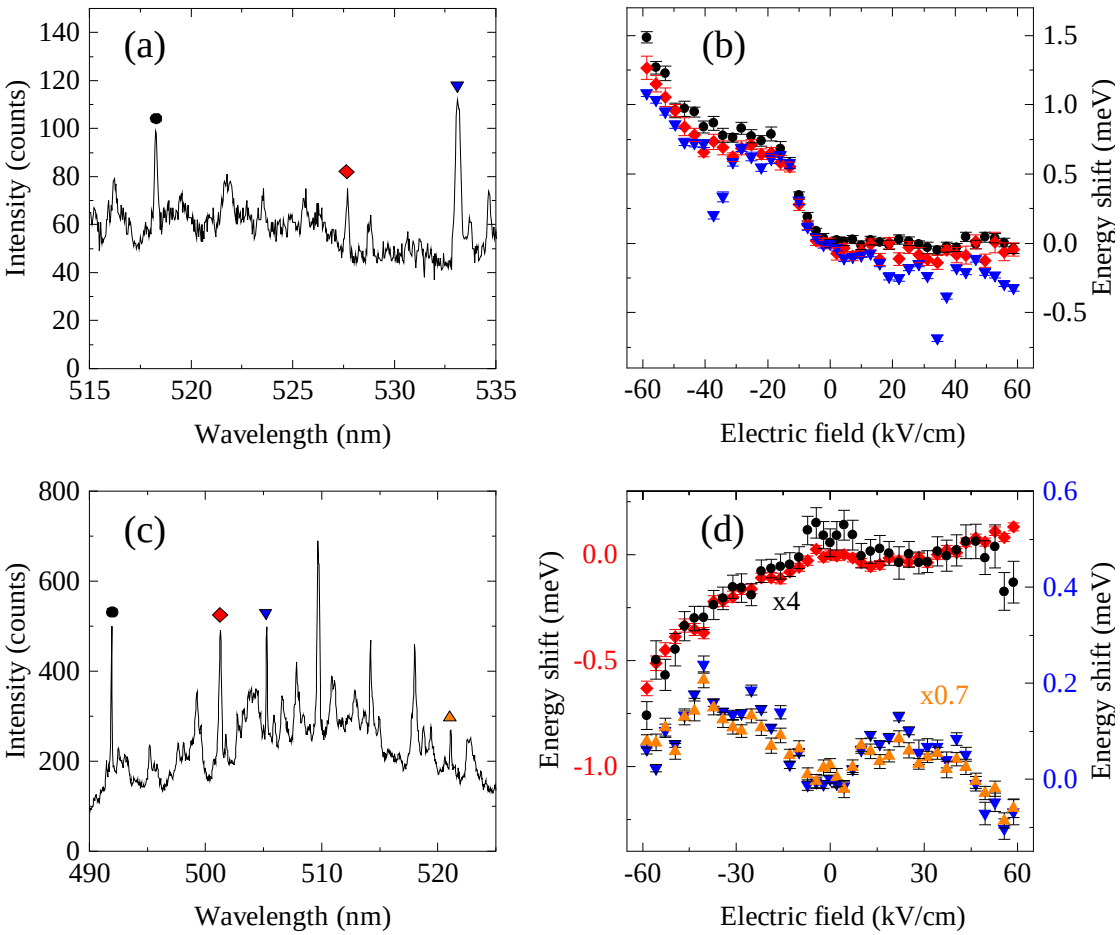

Figure 5.10: Multiple lines showing similar shift behaviour for two spectra taken at a different spatial position. (a) Spectrum 12, see Table 5.1. (b) Electric field dependence of the three, in (a) marked lines. The energy at zero bias is subtracted. (c) Spectrum 15. (d) Electric field dependence of the four, in (c) marked lines. The shift of the shortest and longest wavelength line is multiplied by a factor of 4 and 0.7, respectively. The energy at zero bias is subtracted.

several narrow emission lines in the same spectrum could be observed. Detailed analysis after the experiment showed a similarity in the energy shift behaviour for some of these lines. It should be noted that not all lines in one spectrum behaved the same way. In Figure 5.10(a,c) two spectra with several lines are shown with the respective energy shifts of some of them in panel (b,d).

Since the shift behaviours differed so much between lines and positions, it is highly likely that the lines exhibiting similar shifts originate from the same dot. This would be

possible in two cases: emission from multi-excitonic complexes or excited states. The first case was covered by several studies on arsenide and nitride QDs. A study on InGaAs dots under the influence of a vertical electric field revealed similar polarisability, but different magnitude of the dipole moments of neutral and charged excitons [199]. For a biexciton on the other hand, a difference in shift was observed under the influence of a lateral field leading to the cancellation of the biexciton binding energy [200]. For InGaN QDs only one report convincingly identified two charged excitons in the polar system [91]. They exhibited an energetic distance of approximately 2 meV and 5 meV from the neutral exciton. Furthermore, PL measurements under the influence of a vertical electric field showed that their dipole moments and polarisability were reduced by 15-40% compared to the neutral exciton. The reports on the value of the biexciton binding energy of different InGaN dots $|E_{XX}^{b}|$ are larger in number, with values ranging between sub-10 meV to over 40 meV [201]. For *a*-plane InGaN dots in particular, one report identified a biexciton with a binding energy of -36 meV in PL [64] and in this work 3 biexcitons were found in EL with binding energies ranging between -3.2 meV and 2.9 meV, see subsection 4.3.1.

In contrast to this, the energy spacing between the exciton ground state and the first excited state of an InGaN quantum dot is typically larger. Unpublished results obtained from Saroj Patra and Stefan Schulz from Tyndall National Institute in Cork, Ireland, as part of $\mathbf{k} \cdot \mathbf{p}$ simulations on the influence of the dot shape on exciton binding energies [122] yielded energy spacings between 30 meV and 35 meV for an $In_{0.2}Ga_{0.8}N$ dot with a 30 nm wide base in one dimension and different base ellipticity. For smaller dots this energy separation will increase, as can be qualitatively understood from the particle-in-a-box model. This fits with the result of a tight binding calculation of a polar $In_{0.2}Ga_{0.8}N$ pyramidal dot of a diameter of 8.6 nm and a height of 2.1 nm, yielding a value of 122 meV for the separation of the ground and first excited electron state [202]. The energy spacing between the hole states is negligible. Furthermore, regarding the shift amount, investigations of shallow QD-like traps in a GaAs/GaAlAs QW found that

Spectrum Number	Line wavelength (nm)	ΔE_{i0} (meV)	Shift magnitude (meV)
2	512.6	115	0.47
	529.6	38	0.44
	538.3		0.21
8	515.3	65	0.28
	529.5		0.13
	518.6	22	0.28
	523.5		0.45
10	529.6	6	0.35
	530.9		0.18
12	518.2	67	1.39
	527.6	24	1.34
	533.1		1.31
15	491.9	47	0.15
	501.3		0.74
	505.3	74	0.29
	521.1		0.27

Table 5.1: Lines showing similar shift dependency. $\Delta E_{i0} = E_i - E_0$ denotes the energy spacing between the lowest energy state E_0 and higher states E_i.

higher excited states shifted by a larger amount than the ground state, as they are more extended and therefore the electron and hole are more easily separated [169].

The energy spacings between the lines that exhibited a similar energy shift under the influence of a lateral electric field here obtained are summarised in Table 5.1. In the third column, the difference ΔE_{i0} between the lowest energy line E_0 and the higher energy lines E_i has been calculated. For the lowest energy spacing ΔE_{10}, the measured values range between 6 meV and 74 meV. The smaller values may be due to multi-excitonic complexes. Those larger than 40 meV are more likely to belong to excited states. Most show a similarly large, if not larger shift than the lowest energy line, which could be another indication of excited states. But as similar shifts were only noticed during the detailed analysis after the experiment, no verification of this assignment could be done. In the future, one may identify lines originating from the same dot by showing a similar shift pattern in slow-time scale spectral diffusion measurements [203, 204], investigate the power and polarisation dependence of the lines to identify biexcitons

and trions [205] and probe excited states through photoluminescence excitation [206].

5.9 Conclusion and improvement ideas

In this chapter, the application of a lateral electric field across single InGaN quantum dots grown on the *a*-plane was demonstrated, using two L-shaped opposing Schottky contacts aligned to the crystal directions [*m*] and [*c*].

A single QD line was observed to show a systematic linewidth increase with an increasing bias. A simple semi-classical model based on rapid tunnelling of electrons yielded a minimum lateral dot size of $6(1)$ nm and a minimum lateral confinement potential of $28(3)$ meV, agreeing with previous temperature dependence studies of similar dots. The same QD line showed a parabolic shift to lower energy, with an in-built dipole that was small compared to *c*-plane QDs, as expected. To show that this shift to lower energy was not merely due to heating, thermometry measurements based on Ruby lines were conducted, showing that the leakage current of the device heated the whole sample evenly. Along with the observation that other dot lines shifted to higher energy under the influence of an applied bias, this proved that the electric field was the source of the shifts.

A systematic study was attempted, investigating all lines with a certain minimum brightness and a maximum linewidth. Upon the application of a field, lines responded in general by shifting in energy. No systematic linewidth changes were observed. Apart from noise, two main shift behaviours were identified. The first featured a parabolic dependence of the energy shifts on the applied field observed for 10% of the dots in each arm. This is the well-known influence of the QCSE. The extracted polarisability ranged between 20 meV/(MV/cm)^2 and 200 meV/(MV/cm)^2, where the vertical polarisability of *c*-plane dots fits into the lower range. The values of the dipole moments ranged between -0.45 eÅ and 0.32 eÅ, which is small compared to the vertical component of *c*-plane grown InGaN QDs. This was expected, as the dot area exposed to the polar

c-direction is much smaller. The more surprising fact of different signs of the dipoles is likely due to the peculiar situation of non-polar InGaN dots, with the second order piezo-electricity being opposed to the first order and of similar magnitude. One or the other may be enhanced for different dot shapes, sizes and indium contents. A mean absolute in-built field of 10(4) kV/cm has been deduced, which presents a reduction by approximately two orders of magnitude compared to the vertical field in polar InGaN dots. A second group of emission lines did not show parabolic shifts. This was observed for 62% of the lines found in the arm where the field is parallel to the *c*-direction, and for 80% of the lines in the other arm. Possible reasons for this behaviour were discussed and point towards a locally malfunctioning device.

Coincidentally, it was observed that a few lines in the same spectrum showed very similar shifts behaviours, which were attributed to the same QD. Their energy spacing ranged between 6 meV and 115 meV. This might indicate multi-excitonic complexes for small energies and excited states for larger energies. In the future, this hypothesis should be investigated through similarity in spectral diffusion patterns, power and polarisation dependence measurements and excitation photoluminescence measurements.

In general, it would be desirable to improve the electrical properties through better fabrication methods. For example, it has been shown that a thicker Ni layer of 300 nm reduces the leakage of opposing Schottky contacts [207]. Rapid thermal annealing at an appropriate temperature could also help at this point [207]. It could be useful to establish additional Ohmic contacts to either side of the device to characterise each of the single Schottky contacts in detail.

6 Decreased fast spectral diffusion of non-polar InGaN quantum dots

6.1 Introduction

Nitride dots have been shown to emit single photons at much higher temperatures than arsenide dots, even up to 350 K [54]. However, after decades of research the main advantage of arsenide dots is more mature fabrication, paving the way to bright and, of particular importance, *indistinguishable* sources of single photons. Single quanta of light that are identical in all defining properties, such as polarisation, wavelength, temporal wavepackets, are needed for quantum computing applications [208–210], and could be useful for quantum cryptography applications [5, 211] beyond the protocol BB84 [2].

For nitride QDs to catch up in this regard, a significant reduction of the amount of spectral diffusion is a necessary requirement. This previously mentioned phenomenon occurs when carriers close to a dot are trapped and untrapped, creating a temporarily varying local electric field. This field interacts with an exciton in a QD and causes its emission energy to change due to the QCSE. There are two timescales when this happens: around a few seconds, and on a much faster scale [100]. The latter causes

an inhomogeneous linewidth broadening because spectrometer acquisition times are limited by the CCD detector speed to a minimum of a few milliseconds. Commonly, linewidths of nitride dots are often observed to be in the meV range [54, 100, 212]. Reports of linewidths well below 1 meV are rare [63, 131, 213], down to a minimum of approximately 170 μeV [62]. This is still at least a factor of 100 larger than the minimum linewidth, limited by the typical lifetime of a few ns and below [214]. One reason for this can be found in the large defect densities of nitride materials, particularly of threading dislocations (10^8 cm^{-2} for low density samples grown via MOCVD) as compared to arsenide materials (which are almost defect free within relevant areas) [94, 100, 102, 215]. Growth of GaN on the non-polar *a*-plane is known to result in even larger *a*-plane dislocation densities of 10^{10} cm^{-2} to 10^9 cm^{-2} [96, 216], although, locally, low values of 10^6 cm^{-2} can be achieved through the ELOG technique (compare with subsection 3.1.1). Another important factor is the large piezo-electric and spontaneous polarisation difference between nitride materials along the *c*-direction, resulting in large in-built dipole moments of polar nitride dots. These then interact strongly with nearby carriers. For example in the case of GaN/AlN dots, this is a particularly strong effect, resulting in significantly broader linewidths for lower emission energy dots. This observation has been matched with calculations which show that lower emission energy dots feature a larger height, thus exhibiting a larger dipole moment [217].

Several experimental methods have been employed to characterise spectral diffusion of emission lines at times shorter than a few milliseconds. A spectral hole burning technique allowed the acquisition of spectra through pump modulation and lock-in detection, down to 500 ns [218]. Photon-correlation Fourier spectroscopy uses intensity correlations at the outputs of a Michelson interferometer [219]. Spectral diffusion causes complementary changes in the fringes at the outputs. Its time resolution is theoretically only limited by the correlation system, usually in particular the detectors, to a few hundred picoseconds. However in practice, the requirement of interferometric stability limited a measurement on CdSe/ZnS nanocrystals to a resolution of 20 μs [220]. In con-

trast to this, intensity correlation measurements with an HBT setup in combination with a spectrally narrow resonant excitation are more robust, yielding an account of spectral diffusion due to the shifting of the emitter absorption line in and out of resonance with the laser [221].

Many semiconductor dots, with the exception of arsenide ones, still rely on non-resonant excitation. To apply the non-interferometric intensity correlation technique in this case, spectral filtering of the emission can be used. Filtering out a part of an emission line broadened by spectral diffusion is conceptually the same as resonant excitation in regard to the effect that spectral diffusion has on a measurement of the second order correlation function: When the dot line jitters out of the detection window (off the laser excitation wavelength), it does not contribute to the measurement. For a certain timespan, the electric environment of the dot does not change such that the line fully contributes to the measurement. However, on a longer timescale, the environment fluctuates such that the line jumps randomly in and out of the measurement window (the laser excitation line). This leads to a bunching in an autocorrelation measurement, as demonstrated by the first report studying spectral diffusion with this technique, using a CdSe/ZnSe dot in a nanowire [222]. The same timescale can be found in a cross-correlation HBT measurement, selecting the two halves of the inhomogeneously broadened emission line. Since the line stays within one half for a certain time, an antibunching can be found (in addition to the single-photon induced antibunching at zero delay). Due to the randomness of the line jumps, the spectral filter width does not influence the measured timescale of the bunching or antibunching, but only its strength - as long as the filter window does not comprise the full inhomogeneously broadened emission line.

In the domain of nitride QDs, two reports determined the rate of spectral diffusion of one dot each. Both were grown on the polar plane. An autocorrelation measurement on an interface GaN/AlGaN dot yielded a maximum spectral diffusion time of 22 ns [155]. The excitation power density was around 10 kW/cm^2. A spectral diffusion measurement on an InGaN/GaN dot in a DBR cavity yielded a longer maximum time of 340 ns, in

spite of a higher excitation density of a few hundreds W/cm^2 [156]. This has been attributed to deeper traps in the underlying QW. Both experiments demonstrated a linear increasing trend of the spectral diffusion rate with increasing excitation power[1].

The aim of this chapter is to clarify whether spectral diffusion times of non-polar InGaN/GaN dots are longer, as one might anticipate due to the reduced permanent dipoles (compare with subsection 5.7.1), or shorter, as one might expect as a result of increased dislocation densities as compared to polar InGaN QDs.

6.2 Sample and setup

The dots of the sample used for this study were grown with the MDE technique (see subsection 3.1.1). The QD layer was embedded in the unintentionally doped region of a p-i-n structure. The dopant details are summarised in section 8.1. The sample was etched into randomly located nanopillars for enhanced light extraction by John Jarman in Cambridge. The pillar diameters measured approximately 180 nm. An example scanning electron microscope image can be seen in Figure 3.1(b). The setup used was the more stable, second configuration shown in Figure 3.2(b). All experiments were carried out at 4.5 K. The dots were excited non-resonantly via the InGaN QW with a CW 405 nm laser diode. A 100$\times$ objective with an $NA = 0.7$ was used. Since the dots were not embedded in a cavity, the intensity of the dots was comparatively low. Brightness was a critical factor for this experiment, since the measurement time of the second order correlation function depends quadratically on it, and only half of a dot's linewidth (and therefore half of its intensity) contributed to the experiments described here. Thus, to identify bright dots, the 4f-scanning system was used, along with the dot finding code described in subsection 3.2.4. An example can be seen in Figure 6.1. Once the bright dots were identified, excitation power dependence measurements of the dot intensity and

[1] Another, earlier publication gave a rough estimate of the spectral diffusion time of approximately 25 ns of a GaN/AlN dot as a by-product of a cross-correlation measurement of an exciton and an unconventional biexciton [223].

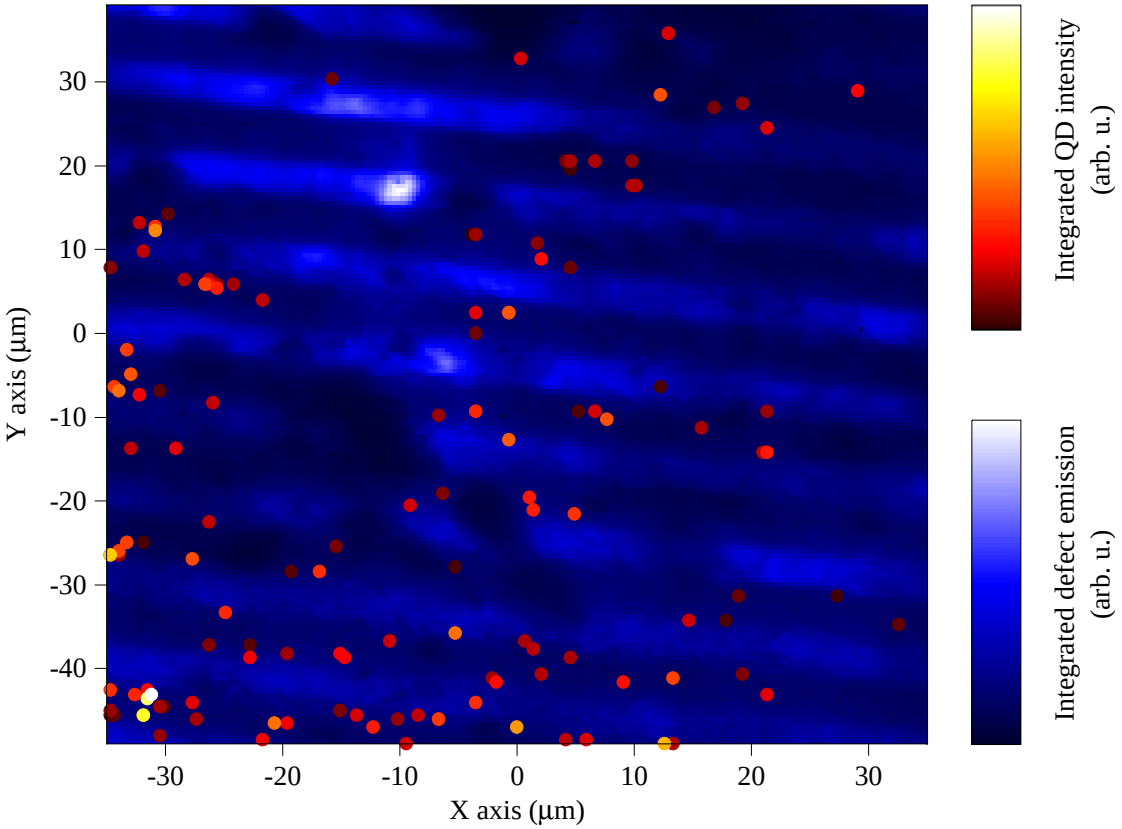

Figure 6.1: Example scan with the 4f-scanning system. The defect emission is integrated between 480 nm and 565 nm, shown in the blue-black scale. On top, the position of the most intense dots found with the automatic fitting option is shown. Their integrated intensity is colour-coded, too. The dot studied in the following sections is the brightest one, marked in white in the bottom left corner. The shear calibration factor is not included as absolute positions are not important.

linewidth were conducted using the third diffraction order of a fine 1200 l/mm, 500 nm blaze grating to increase the spectral resolution. This was only possible because of the comparatively high dot brightness and the existence of another 1200 l/mm grating in the same spectrometer with a blaze for 1000 nm, which boosted the intensity compared to the 500 nm blaze. The use of the 4f-scanning system included automatically confocal collection, favourably reducing background emission for second order correlation function measurements. For these, the spectrometer served as a filter with variable width, with the first diffraction order of the fine 1200 l/mm grating. The HBT setup, described in detail in subsection 3.2.6, was positioned behind the output slit of the spectrometer.

The slit was imaged onto the HBT PMTs via a biconvex lens with a focal length of 25 mm. It was aligned together with the beamsplitter of the HBT setup, without the PMTs, with the help of a laser routed through the multimode fibre going into the spectrometer. The TCSPC card used was a *TimeHarp260* (sold by the company *PicoQuant*). The exponential decay time of the instrument response function of the HBT setup was determined with an approximately 100 fs, 425 nm laser to be $R = 116(1)$ ps. A *Labview* program enabled automatic optimisation of a dot's intensity after a set amount of time by moving the x- and y-piezo positioners.

6.3 Properties of the studied quantum dot

In regard to fast spectral diffusion, a detailed study of one quantum dot grown on the *a*-plane is presented. It was found by means of a map obtained with the 4f-scanning system. In Figure 6.1, the brightest dots of the scan are shown on a background of the defect emission integrated between 480 nm and 565 nm. It can be seen that the defect emission varies spatially in bands. This is due to the ELOG template used for the growth. A cathodoluminescence study on an *a*-plane ELOG GaN sample attributed the dark regions to positions where no mask was present [224] (compare the ELOG method described in section 3.1). It can therefore be concluded that the majority of bright QDs can be found on material with a higher dislocation density, but likely a lower point defect and impurity density [224]. The white marked QD in the bottom left corner was chosen because of its high brightness to carry out the spectral diffusion experiments.

First, however, its basic properties are identified. Its spectrum is shown in Figure 6.2(a) measured with a fine 1200 l/mm grating in first and third diffraction order. The latter data was fitted with a Gaussian. The dot linewidth thus obtained[2] was approximately 320 μeV at an excitation power of 10 kW/cm^2, lying above the spectral resolution of 260 μeV. For a non-polar InGaN dot, this is one of the smallest values

[2] In the following, quantitative values referring to a linewidth will always use the FWHM as metric.

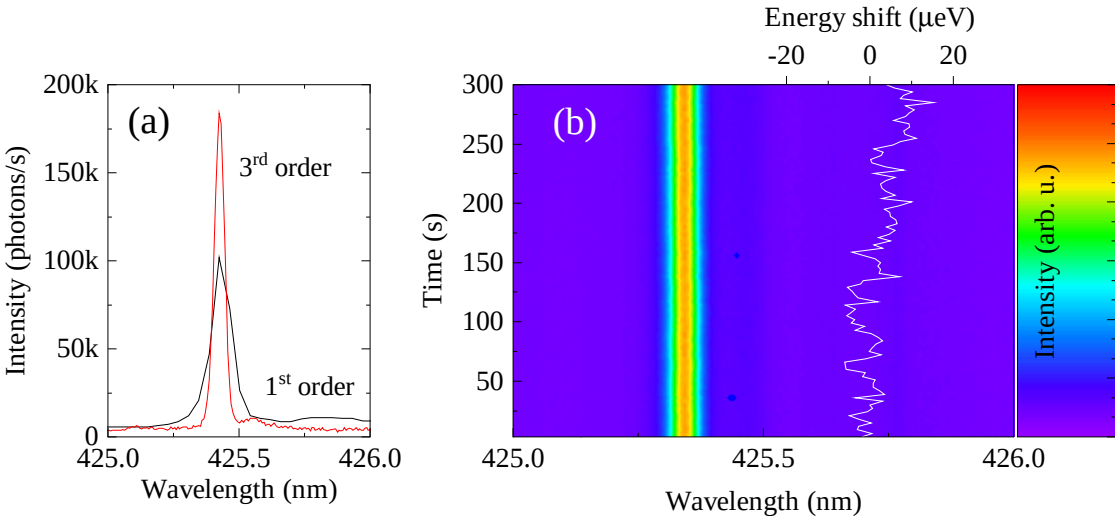

Figure 6.2: (a) Spectra recorded with the first and third diffraction order of the spectrometer of QD1. The third order spectrum is rescaled to the integrated intensity of the first order one. Excitation power density 10 kW/cm^2, integration time 3 s. (b) Slow timescale spectral diffusion over 5 min. Third diffraction order, excitation power density 10 kW/cm^2. On the right side, the fitted peak position is shown in white. The fit uncertainty of the energy lies on the order of 1 μeV.

measured, though it is still more than two orders of magnitude larger than the lifetime-limited width. In Figure 6.2(b), a sequence of 100 spectra, acquired over 5 minutes, is shown. In the colour-coded intensity profile, no variation of the peak energy can be discerned. The peak energy was extracted with a Gaussian fit for each spectrum. This is shown as a white line on the right hand side. It varied by only approximately 20 μeV over 5 min, which is very stable for a nitride QD.

In Figure 6.3(a-c) the power dependence of QD1 is shown. The measurements were carried out with the third diffraction order of the 1200 l/mm grating with a blaze of 1000 nm, and an integration time of 20 s, whilst monitoring the excitation power. In panel (a), the intensity dependence for CW excitation is shown. The equivalent first diffraction order intensity is given, established through two calibration measurements at both diffraction orders at the same power and integration time. To make it comparable to other setups, the intensity is given in number of photons per second detected by the

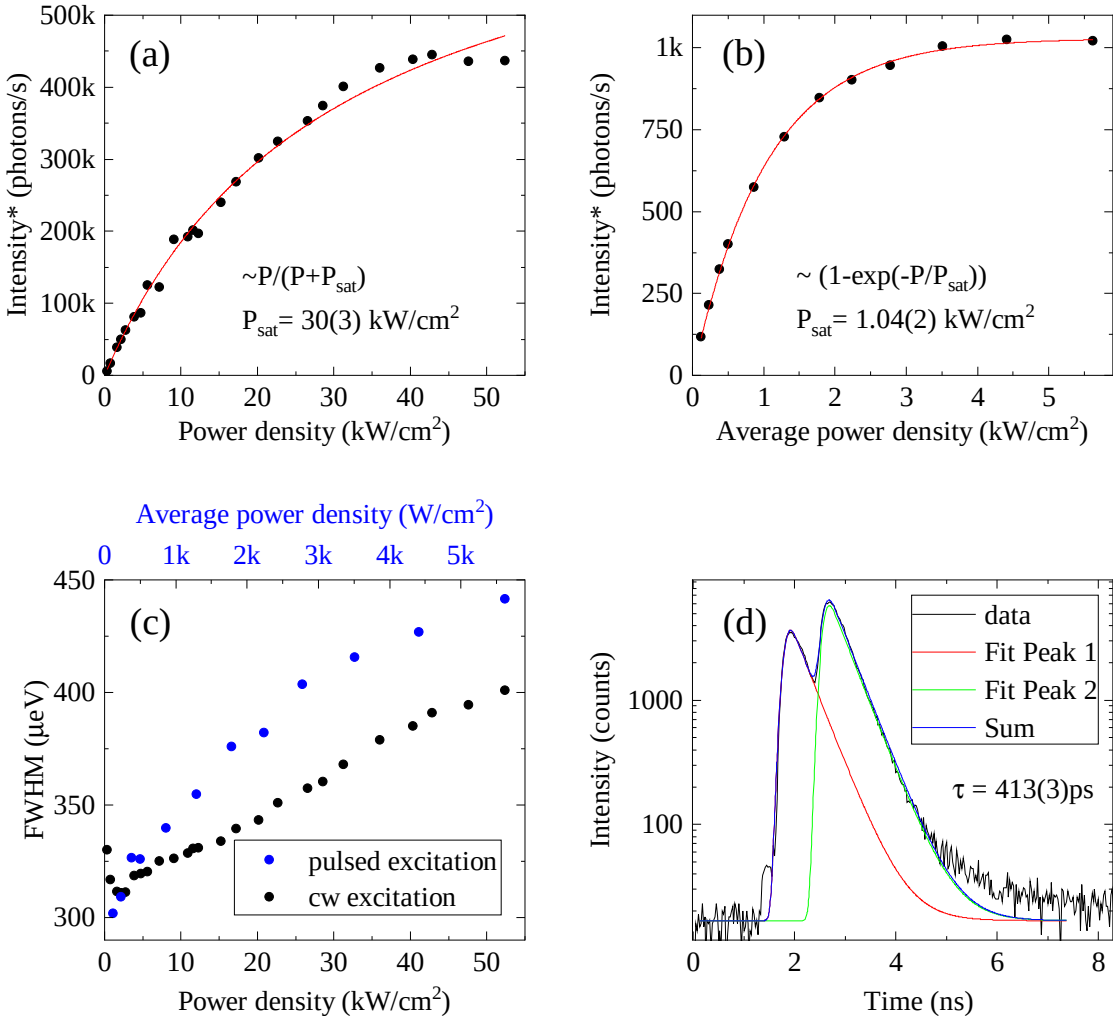

Figure 6.3: Excitation power dependence and lifetime measurement of QD1. The third order diffraction of the 1200 l/mm, 1000 nm blaze grating was used. (a,b) Intensity dependence under CW and pulsed excitation. The equivalent first diffraction order intensity is given. (c) Linewidth dependence for both excitation types. (d) Lifetime measurement at an average excitation power of 8 kW/cm^2. The prepulse is due to a reflection in the sync cable. The fit is detailed in the main text.

CCD[3], instead of counts/s. A fit of the shape [225]

$$I = I_{\mathrm{sat,CW}} \cdot \frac{P}{P + P_{\mathrm{sat,CW}}} \tag{6.1}$$

yielded a saturation intensity of $I_{\mathrm{sat,CW}} = 740(30) \times 10^3$ photons/s and a saturation

[3]For different settings of the CCD used here, the equivalent of 1 count can vary between 2.6 and 16 electrons.

power density of $P_{\mathrm{sat,CW}} = 30(3)\,\mathrm{kW/cm^2}$. The latter value is at least one order of magnitude larger than typical excitation power densities used for the spectral diffusion measurement on a polar InGaN QD [156]. On the one hand, this might be due to an increased density of dislocations, which provides alternative recombination pathways to carriers. On the other hand, this report used a cavity, such that a lower power density might have been needed to excite dots. Along with the setup efficiency of approximately 1%, the saturation intensity can be used to estimate the outcoupling efficiency, giving an approximate value of 3%[4]. This is plausible for a dot surrounded by high refractive index material without a cavity, but with the modest enhancement through the etched pillar.

In Figure 6.3(b), the intensity dependence for pulsed excitation with a frequency-doubled 80 MHz Titanium-Sapphire laser, tuned to the same wavelength of 405 nm as the CW laser diode, is shown. The pulse duration was approximately 100 fs. A fit with the following equation [48, 190, 226]

$$I = I_{\mathrm{sat,puls}} \cdot \left(1 - \mathrm{e}^{-P/P_{\mathrm{sat,puls}}}\right) \tag{6.2}$$

yielded a saturation intensity of $I_{\mathrm{sat,puls}} = 1030(6)$ photons/s and an average saturation power density of $P_{\mathrm{sat,puls}} = 1.04(2)\,\mathrm{kW/cm^2}$. As expected, the saturation average power is lower than in the case of continuous excitation. The ratio of the saturation intensity for CW and pulsed excitation $I_{\mathrm{sat,CW}}/I_{\mathrm{sat,puls}} = 720$ should reflect the ratio of the inverse of the lifetime and the repetition rate of the laser. However, this ratio equates only to approximately 30, and points to a reduced excitation efficiency of the dot for pulsed excitation. This agrees with the increased level of the QW background under pulsed excitation (not shown). To pin down the cause of this behaviour, and a strategy to mitigate it, further studies would be needed.

[4] Estimate: Maximum saturation intensity 7.4×10^5 photon/s divided by the setup efficiency of 0.01 and multiplied by the approximate lifetime of 4×10^{-10} s.

In Figure 6.3(c), the dependence of the dot linewidth on the (average) excitation power density for both CW and pulsed excitation is shown. One can see a rising, linear trend with increasing power, starting from approximately 300 μeV. Under very high pulsed excitation not obtained with continuous excitation, however, the linewidth increases sublinearly. The increase of the FWHM with increasing power is the first indication of an increase in the strength of fast timescale spectral diffusion, when the more carriers are excited. The linewidth values are approximately the same for both excitation types in terms of the saturation power density.

In panel (d), the lifetime of QD1 is shown. It was measured with one of the PMTs of the HBT setup at an excitation power of 8 kW/cm^2. Its IRF is approximately Gaussian with a width of $FWHM = 210$ ps. The data was fitted with a convolution of a mono-exponential decay and a Gaussian IRF. Additionally, a pulse replica was included with the same IRF width and QD decay time to account for a reflection in the electrical cable coming from the laser clock diode. The fit yielded a lifetime of $\tau = 413(3)$ ps, which lies in the range of previously observed lifetimes of InGaN dots grown on the *a*-plane [145].

To be sure that the emission line was indeed emitting single photons, the second order correlation function was measured with the HBT setup described in the setup chapter. The HBT setup was installed at the output slit of the spectrometer in order to be able to use the spectrometer as a filter with a sharp cut-off. In this case, an output slit width of 7 CCD pixels was chosen in order to include the full dot line, which had a FWHM of approximately 2.5 CCD pixels when using the 1200 l/mm grating. In Figure 6.4(a), the second order correlation function of QD1 for an excitation power density of 2.9 kW/cm^2 and a bin width of 25 ps is shown. It was obtained from the raw measurement done in the start-stop-mode by normalisation to the coincidence level at long delay times ($|\tau| > 3$ ns). It features a dip at zero delay time down to $g^2(0) = 0.6$. As the QD lifetime is relatively short and, along with the pump rate, contributes to a shorter HBT rise time (compare with Equation (4.4)), the latter may be comparable to the HBT IRF. It has been measured at the dot wavelength, shown in the inset of Figure 6.4(b). The IRF is

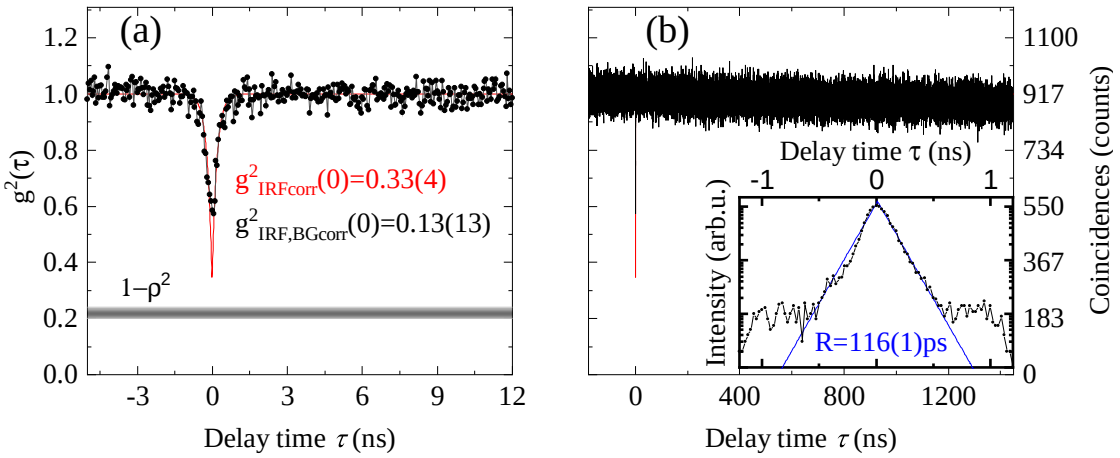

Figure 6.4: Single photon emission of QD1. (a) Second order correlation function including the full dot linewidth, measured at 2.9 kW/cm^2. The QW background emission decreased the dot-to-signal ratio to $\rho = 0.88$, leading to an offset of $1-\rho^2$. The fit is the IRF corrected $g^2_{\mathrm{IRFcorr}}(\tau)$ (Equation (4.3)). (b) Same measurement on a larger delay timescale. A decrease of the counts with increasing delay time is visible, starting at zero measurement delay time. This is due to the pile-up effect. The inset shows the HBT IRF on a logarithmic scale, fitted with an exponential decay function (Equation (4.4)).

well described by an exponential decay, apart from the low intensity side wings, yielding $R = 116(1)$ ps (compare with Equation (4.4)). Fitting the second order correlation function with the IRF-corrected Equation (4.5) yields a value of $g^2(0)_{\mathrm{IRFcorr}} = 0.33(4)$. In addition to the IRF, the QW background emission also has an influence on the above figure of merit. In this case, the ratio of the quantum dot to the total signal within the window of 7 CCD pixels is $\rho = 0.88(4)$, estimated from the offset of a Gauss fit to the QD line. To correct for the influence of background light, one can apply the commonly used formula [61, 137, 227]

$$\frac{1-g^2_{\mathrm{raw}}(0)}{1-g^2_{\mathrm{BGcorr}}(0)} = \rho^2, \tag{6.3}$$

yielding a background and IRF corrected value of $g^2_{\mathrm{IRF,BRcorr}} = 0.13(13)$. The uncertainty interval was obtained by using Equation (6.3) with combinations of the value plus or minus the uncertainty on the input parameters g^2_{IRFcorr} and ρ. It is clear therefore that the dot emitted single photons as the corrected $g^2(0)$ value is well below the threshold

of 0.5, which would be obtained by a Fock state $n = 2$.

6.4 Fast timescale spectral diffusion

Having evaluated the basic dot properties, we can come to the actual experiment we want to perform. It is very similar to the measurement of the second order correlation function previously discussed. The only change consists in restricting the filter window of the spectrometer to a part of the dot linewidth. First, however, there is a technical challenge which needs to be addressed.

6.4.1 Pile-up effect

The challenge can already be seen when contemplating the zoomed out HBT trace shown in Figure 6.4(b): the level of coincidence counts is not constant for long delay times, it decreases. When fitting an exponential bunching decay alongside this slow decrease, this is problematic. To make matters worse, the spectral diffusion time constant of this particular dot appears to be on the order of a few hundred nanoseconds. This makes it even more difficult to distinguish between the decaying background and the bunching originating from the spectral diffusion.

To understand the origin of this slow decay in the HBT trace, the dependence of it on the count rate was investigated. The count rate was changed solely by changing the output slit width, and the input light was mainly originating from a QW. As can be seen in Figure 6.5(a) on a semi-logarithmic scale, the decay is mono-exponential in nature. Its decay time is shorter for a higher input count rate on the PMTs, whilst the coincidence level at zero delay time naturally increases. This is quantified by fitting single exponentials to each data set. The relationship between the decay time T and the amplitude A of the exponential, meaning the level of coincidence counts at zero delay time divided by bin width and measurement time, is shown in Figure 6.5(b). On a double-logarithmic

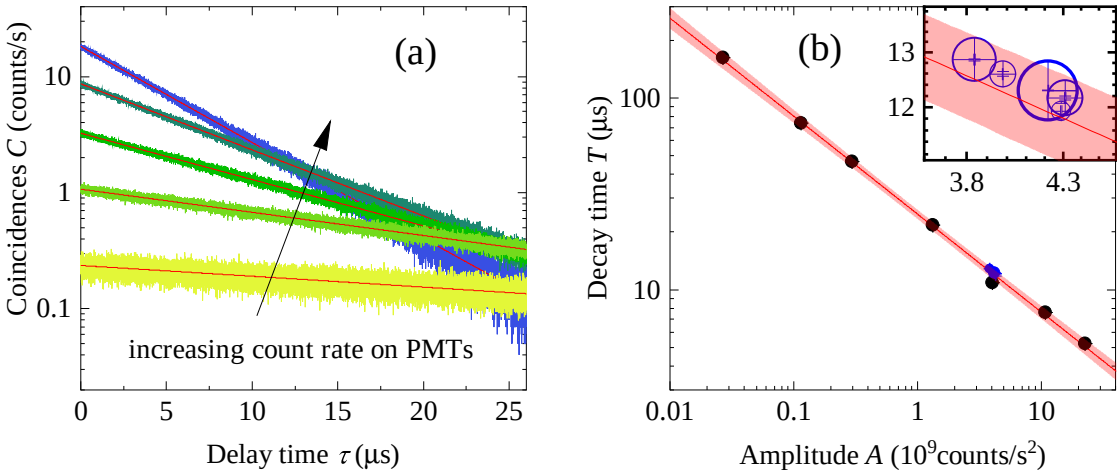

Figure 6.5: Study of the pile-up effect with increasing count rate. (a) A few data sets with mono-exponential fits. (b) Relation between exponential decay amplitude and decay time for a bin width of 0.8 ns. The red line is linear fit on the double-logarithmic scale, the parameters are given in the main text. The red shaded area marks the uncertainty range. The blue data points, shown magnified in the inset, are the results of a variation of the bin width (0.05, 0.1, 0.2, 0.4, 1.6 ns). The marker diameter is proportional to the logarithm of the bin width.

scale, the points clearly follow a linear relation, yielding the following parameters.

$$T = \frac{24.8(5)\mu\text{s}}{A^{0.511(9)}} \left(\frac{10^9 \text{counts}}{\text{s}^2} \right)^{0.511(9)} \tag{6.4}$$

Before this experiment, the dependence of the decay time on the bin width was tested. For a bin width between 0.05 ns and 1.6 ns, a mono-exponential decay was found, whereas for a bin width of 6.4 ns a biexponential decay was observed. For this reason, the bin width was set to 0.8 ns for the previous measurement of the count rate dependence. The mono-exponential data points are shown in detail in the inset of Figure 6.5(b). Within the uncertainty of the fit, they are consistent with the data set for different count rates. The conclusion from the relationship between decay time and amplitude is that the effect is due to classic pile-up [108]. In the classic HBT start-stop mode, the arrival of photons after the stop signal in the same channel will be neglected in the sense that it will not contribute to the histogram at a longer time delay. It is for

this reason that the count rate drops at longer delay times. It also explains why the decay time decreases as the count rate on the PMTs increases: the more photons there are on average, the more likely it is that one will take the path to the stopping PMT. The electronic origin of the effect will also become clear in spectral diffusion HBT measurements with narrower time bins, showing that the pile-up decay does not start at zero delay time but zero measurement delay time.

It was only after the experiments that I realised the pile-up effect could be circumvented by the use of a so-called time-tagging mode, where the arrival times of the photons are recorded, and the second order correlation function is calculated from this list post measurement. This is possible due to a short deadtime of detector and a short processing time of an appropriate TCSPC card. However, the results presented below are similar to those measured with the time-tagged mode, as will be demonstrated in subsection 6.4.3.

An example measurement is shown in Figure 6.6(a). It used the higher energy half of the dot linewidth at a relatively high excitation power of $18.2\,\mathrm{kW/cm^2} = 0.64 \cdot P_{\mathrm{sat}}$. The time bin was set to 50 ps, in order to be able to cover an interval of $1.6\,\mu$s, as the maximum number of bins is limited to 32768. To obtain a reasonable signal-to-noise ratio, the data was rebinned post measurement with a bin size of 1 ns. Three features can be seen: an antibunching dip at zero delay time, which is due to the single-photon nature of the QD emission, a bunching peak around zero time delay, which is caused by spectral diffusion, and an apparently linear coincidence count decay for longer delay times, which is due to the aforementioned pile-up effect. The zero delay time is not in the middle because the maximum electronic delay of both channels combined only amounts to 200 ns. A longer delaying cable would have considerably decreased the count rates.

In order to extract the spectral diffusion bunching time, the pile-up decay time needs to be estimated first. One way to do this is to determine the coincidence count rate at

zero measurement delay time[5] divided by the bin width, and then use this value as input for the pile-up calibration Equation (6.4). However, the coincidence count rate at zero measurement time can only be obtained with a high degree of uncertainty due to noise in the measurement and also a potentially non-negligible influence of the bunching.

Therefore integration is used, as this is a more robust method. Summing all the counts over the whole delay time interval yields on the one hand a certain number of counts C^*. On the other hand, the analytical integration - assuming that the sum of bunching counts are negligible in comparison to the summed pile-up decay counts - yields an equation depending on both the normalised decay amplitude A and the pile-up decay time T:

$$C^* = \int_0^{\tau'_{\max}} A \cdot t_{\text{meas}} \cdot \mathrm{e}^{-\tau'/T} \, \mathrm{d}\tau' = A \cdot T \cdot t_{\text{meas}} \left(1 - \mathrm{e}^{-\tau'_{\max}/T} \right), \tag{6.5}$$

with the HBT measurement time t_{meas} and the maximum measurement delay time $\tau'_{\max}$. In a second step, A is replaced using the pile-up calibration Equation (6.4). The resulting non-linear equation is then solved numerically in order to determine the pile-up decay time T. It is numerically verified that the function $T(C^*)$ is monotonically decreasing for increasing C^*, such that small deviations in the total number of counts do not produce totally different results. In the example case shown in Figure 6.6(a), $T = 30(1)\,\mu$s is obtained. Its uncertainty is obtained by solving Equation (6.5) with all combinations of the pile-up calibration parameters plus or minus their uncertainty and taking the maximum and minimum value.

We are now in a position to extract the bunching time by fitting the HBT trace, excluding the few anti-bunching data points, with the following equation

$$C(\tau) = D \cdot \mathrm{e}^{-(\tau+\tau'_0)/T} \cdot \left(B \cdot \mathrm{e}^{-|\tau|/T_{\text{SD}}} + 1 \right) \tag{6.6}$$

[5] Here the distinction between measurement delay time τ' and delay time τ is made because the pile-up effect starts to take effect at the first measurement bin, which does not necessarily correspond to zero time delay.

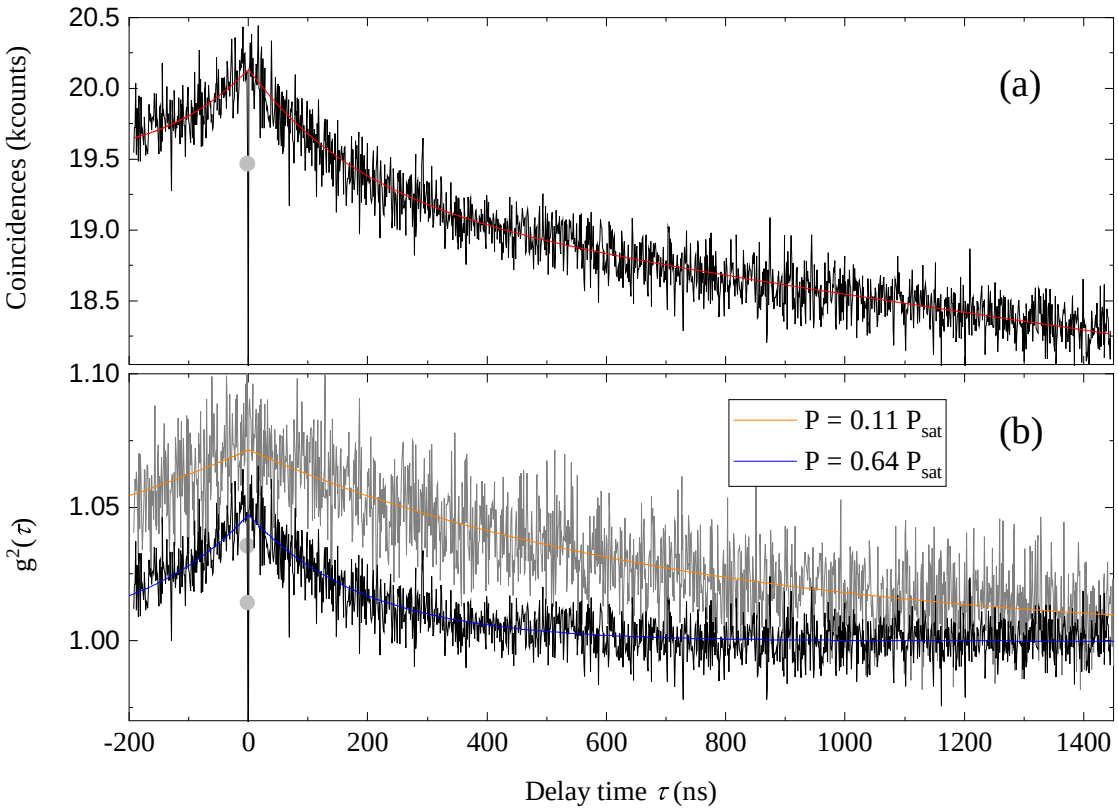

Figure 6.6: Spectral diffusion traces rebinned to a bin width of 1 ns. (a) HBT trace of QD1 for a wavelength selection of half the dot's linewidth at an excitation power density of 18.2 kW/cm^2. The fit is described by Equation (6.6), excluding the antibunching data points. (b) HBT traces for a wavelength selection of half the dot's linewidth at two different excitation powers, corrected for the pile-up decay. The fits are described by Equation (6.7).

with the proportionality constant D, the bunching amplitude B, the offset of the measurement time delay from zero time delay τ_0' and the spectral diffusion time T_{SD}. The term in the brackets accounts for the bunching due to the spectral diffusion, and the prefactor accounts for the pile-up effect. In case of an infinitely low count rate, the decay time T goes to infinity, such that the prefactor tends to 1, retrieving an overall functional expression commonly used in previous reports [155, 156]. The method to obtain the uncertainty of the spectral diffusion time and the bunching amplitude is explained exemplarily for the latter: the data is also fitted with the values $T \pm \delta_T$, providing slightly different values $B(T+\delta_T)$ and $B(T-\delta_T)$. The mean deviation Δ_B from B is taken $\Delta_B = [B(T+\delta_T) - B(T-\delta_T)]/2$. This uncertainty is then added together with

the uncertainty of the original fit δ_B to obtain $\delta_{\mathrm{B,total}} = \sqrt{\Delta_B^2 + \delta_B^2}$.

The HBT trace can then be corrected for the pile-up decay, normalised to obtain a value of 1 for long delay times and fitted with the following equation.

$$g^2(\tau) = B \cdot \mathrm{e}^{-\tau/T_{\mathrm{SD}}} + 1 \tag{6.7}$$

This is shown for the above mentioned example in Figure 6.6(b).

6.4.2 Power dependence of the fast spectral diffusion time of QD1

Similarly, an HBT trace at a much lower excitation power density of $P = 0.11 \cdot P_{\mathrm{sat}}$ with the same wavelength window selected was taken. The trace, corrected for the pile-up effect, is also shown in Figure 6.6(b). It can be seen that the spectral diffusion time is increased. This is expected, as a reduced excitation power results in a decrease in the number of carriers that could interact with the QD. To underline this explanation, more HBT traces were taken at different excitation powers for a spectral window of half the QD's linewidth. All the traces were corrected for the pile-up effect and fitted as previously described, extracting the spectral diffusion time. This data set is presented in Figure 6.7(a). It can be seen that the spectral diffusion time does indeed increase with decreasing excitation power. The trend can be more easily seen for the spectral diffusion rate, the inverse of the spectral diffusion time, shown on the right vertical scale: the trend is linear as previously motivated. The longest spectral diffusion time of 860(160) ns achieved is longer than for previous reports on nitrides dots by at least a factor of approximately 2.5 [156].

In Figure 6.7(b), the excitation power dependence of the bunching amplitude is shown. As explained in section 6.1, only the bunching strength and not the spectral diffusion time is dependent on the width of the spectral window. This parameter was kept con-

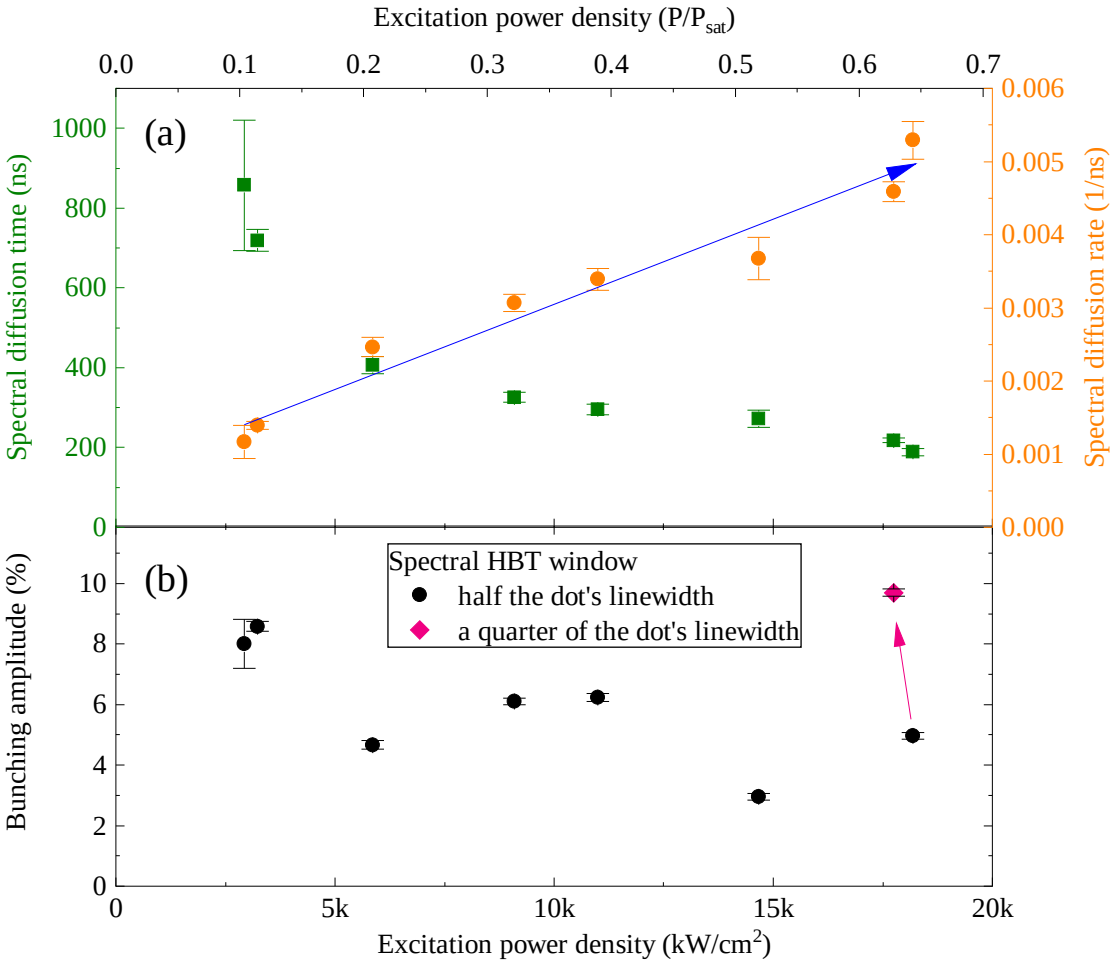

Figure 6.7: (a) Excitation power density dependence of the spectral diffusion time (left scale) and the spectral diffusion rate (right scale). (b) Excitation power dependence of the spectral diffusion bunching strength. All data points but the pink one are measured for a spectral HBT window width of half the dot's linewidth.

stant throughout the experiment at the width of 3.5 CCD pixel, with the exception of one data point at the second highest excitation power, which was measured with a spectral window corresponding to 1.5 CCD pixel, which is approximately a quarter of the dot's linewidth. Nevertheless, for the remainder of the data points measured with the same spectrometer output slit width, a decrease of the bunching amplitude with increasing power can be seen. This might be due to the fact that with increased excitation power, the spectral diffusion rate not only increases on a fast timescale but also on a much slower timescale of hours. If the inhomogeneously broadened dot line drifts

into the spectral HBT window, such that the centre part of the line is symmetrically included, the proportion of the QD emission being measured will increase, so reducing the bunching amplitude. Conversely, if the centre of the dot line drifts away from the spectral HBT window, a smaller part of the dot is selected. At the same time, a larger proportion of the light detected by the HBT setup would originate from QW, thus also reducing the bunching. However, narrowing the spectral HBT window has the effect of increasing the bunching amplitude, as can be seen in Figure 6.7 for the two data points at the highest excitation power.

6.4.3 More QD examples

The potential landscape and defect distribution surrounding a QD varies from dot to dot. To ensure that the behaviour of the dot presented in the previous subsection is not an exceptional case, the spectral diffusion time of more QDs has been determined. Although no maps for them were saved, given the distribution in Figure 6.1, it is likely that these dots also lie in the window region of the ELOG sample, where no mask is present, and the threading dislocation density is high. For all the QDs, first an HBT with a wide spectral selection window was taken, comprising the total QD linewidth, to verify that no bunching occurs due to other sources, such as random charging and uncharging of the dot [52, 228], or degenerate biexciton-exciton emission [229]. Next, the spectral width of the HBT was narrowed down to half a dot's linewidth. The resulting trace was corrected for the pile-up effect and fitted with Equation (6.7). Two extreme examples are shown in Figure 6.8. The measurement on QD3, emitting at 438 nm, yields the shortest spectral diffusion time of 70(5) ns for an excitation power of $P = 12.7\,\mathrm{kW/cm^2} = 0.2 \cdot P_{\mathrm{sat}}$; whereas QD2, emitting at 424 nm, yields the longest spectral diffusion time of 1170(50) ns for an excitation power of $P = 7.4\,\mathrm{kW/cm^2} = 0.07 \cdot P_{\mathrm{sat}}$. This is 3.5 times longer than any previously measured spectral diffusion time of a nitride dot, particularly that of a polar InGaN dot [156]. This shows that non-polar InGaN QDs

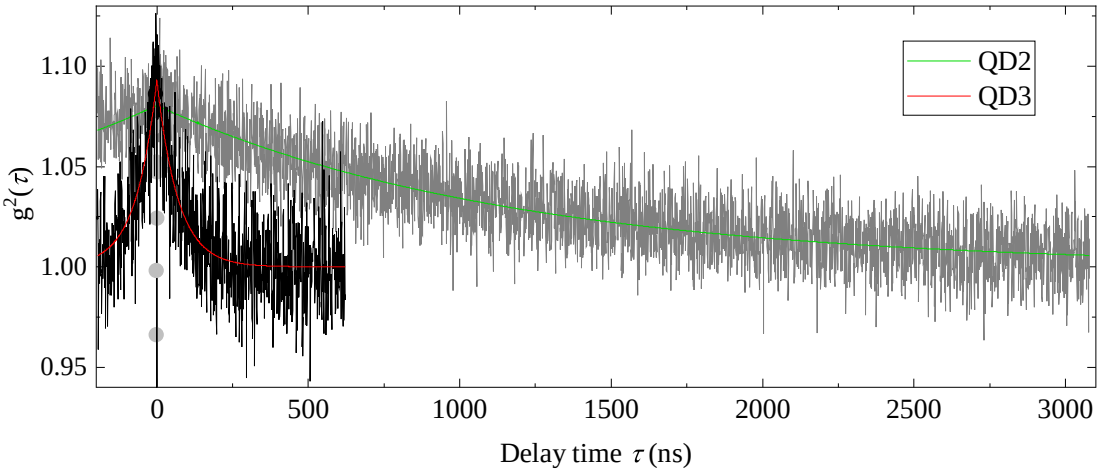

Figure 6.8: Second order correlation function of two other dots QD2 and QD3 at an excitation power density of $P = 7.4\,\mathrm{kW/cm^2}$ and $P = 12.7\,\mathrm{kW/cm^2}$, respectively. The fits are described by Equation (6.7), yielding spectral diffusion times of 1170(50) ns and 70(5) ns.

grown on the *a*-plane exhibit similar and in some cases longer spectral diffusion times than polar InGaN dots, despite a higher threading dislocation density in the former case. Moreover, since the lifetimes of non-polar InGaN QDs are on average at least a factor of two shorter than those of polar InGaN dots, the important ratio of spectral diffusion time to lifetime is favourably larger for the non-polar dots.

6.4.4 Comparison of a spectral diffusion measurement in start-stop and in time-tagged mode

The disadvantage of the pile-up effect can be mitigated by using a TCSPC card supporting the so-called time-tagged mode, in which a list of all the photons detected in the different channels is recorded. Post-measurement analysis can then be performed to retrieve the second order correlation function without a pile-up effect. One hurdle to overcome to use this method lies in the enormous size of the data files, which is naturally much larger than simple HBT measurement traces. For the analysis, a *Python*-coded program[6] was used, which interlinks with *C*-libraries to speed up the calculation.

[6] Available freely on github https://github.com/QuantumPhotonicsLab/readPTU

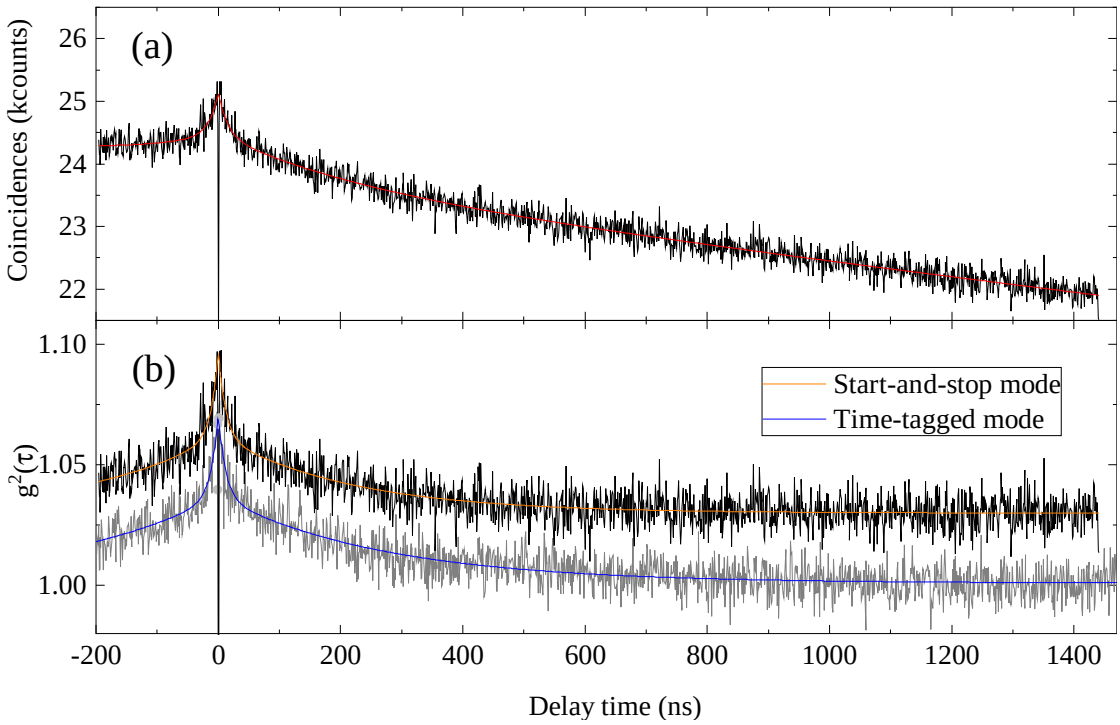

Figure 6.9: (a) Uncorrected start-stop HBT trace on QD4. The fit is a biexponential version of Equation (6.6) with the parameters described in the main text. (b) Comparison of the pile-up corrected and normalised second order correlation function measured in the start-stop mode to the time-tagged measurement of the same QD4. The former trace is shifted upwards by 0.03. The fits are a biexponential version of Equation (6.7) with the parameters described in the main text.

It was written by Raphaël Proux, formerly a member of Professor Brian Gerardot's group at the Heriot-Watt-University, Edinburgh, United Kingdom [230].

A comparison measurement was made on another QD4, emitting at 443 nm. To ensure good comparability, the measurement mode was changed every hour and the cycle repeated 4 times. The traces were then added together for each mode. The uncorrected start-stop trace is shown in Figure 6.9(a). From the time-tagged measurement in panel (b), it becomes evident that the bunching decay is biexponential in this case. This untypical behaviour might be caused by two different trap populations. It is not caused by charging events, as an HBT on the full line showed no bunching. An appropriate adaptation of Equation (6.6) yields a good fit to the uncorrected start-stop trace. In panel (b), it is corrected for the pile-up effect and normalised. Fitting both traces with

Equation (6.7) adapted for the biexponential bunching decay yields $T_{SD1} = 11(2)$ ns and $T_{SD2} = 216(12)$ ns for the start-stop mode, and $T_{SD1} = 12(2)$ ns and $T_{SD2} = 271(14)$ ns for the time-tagged mode. The short component spectral diffusion decay times are the same within their margins of uncertainty. For the longer components, the time-tagged decay time is 25% longer than the start-stop decay time. It was expected that the former is longer than the latter, as the integration method used to determine the pile-up decay time from the data neglects the excess bunching counts. This leads to an increased number of counts C^*, and in turn to a decreased pile-up time T' and results in a decreased bunching time T'_{SD}. However, the size of the difference $T'_{SD} - T_{SD}$ is surprising. A calculation was carried out by assuming the bunching parameters measured in the time-tagged mode as a good guess of the true values, and simulating the pileup decay with a time constant similar to the one observed in the start-stop measurement. The previously explained nonlinear equation solving and fitting procedure was then used to determine the start-stop parameters and compare them to the initial ones of the time-tagged mode. This revealed that the impact of the slightly shorter pile-up decay time on the fitting of a biexponential bunching, with the same decay times and amplitudes as obtained above for the time-tagged mode, is a decrease of the decay times of 1.7%. This is negligible in comparison to the reduction of 25% observed in the experiment.

However, this calculation did not take into account the presence of noise, both on top of the trace obtained in start-stop mode and the time-tagged mode. Rerunning the comparison calculation with a typical 1% Gauss-distributed noise on top of the signal of both the time-tagged and the start-stop mode data for 1000 noise configurations painted a different picture. The same noise configuration was used for both modes. The results for the longer spectral diffusion time T_{SD2} are given in Figure 6.10. The results of the shorter spectral diffusion time T_{SD1} are similar. In panel (a) the comparison between the spectral diffusion times of both modes are shown for identical noise configurations and for randomly different noise configurations. It can be seen that there is a strong correlation between the decay times in case of the same noise configuration, as one could

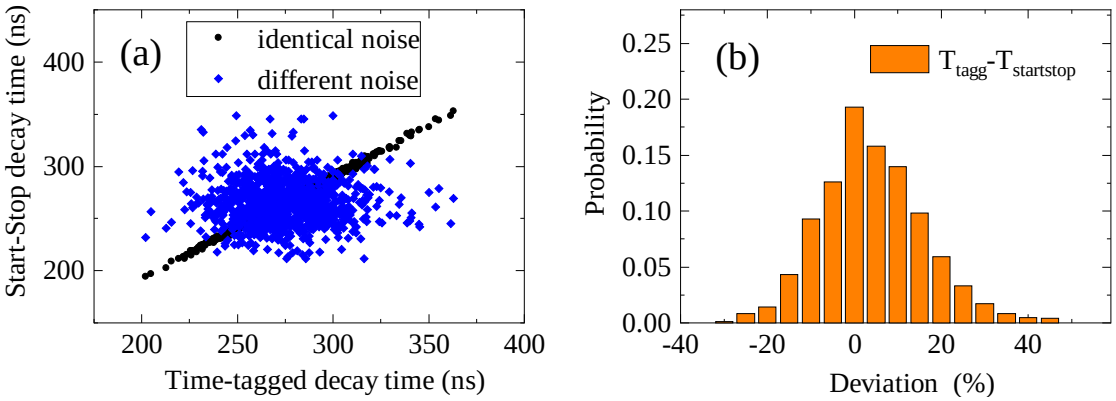

Figure 6.10: Calculation of the measurement in Figure 6.9. Comparison of the longer decay spectral diffusion time T_{SD2} obtained by fitting mock start-stop data and mock time-tagged data, including a 1% noise. (a) Comparison of the fitted decay times for the identical noise configurations and different noise configurations. (b) Distribution of the deviation of the start-stop T'_{SD2} from the time-tagged T_{SD2}, as a fraction of the start stop T'_{SD2}.

expect. However, the measurements present above in Figure 6.9 have been carried out sequentially, so that the noise was different for each measurement. Therefore, we want to see the deviation of the start-stop time from the time-tagged time for different noise configurations. This is shown in panel (b) in orange. A start-stop mode time shorter by more than 22% compared to the time-tagged mode time occurred with a probability of 0.08. Therefore, it seems likely that the difference between the experimentally obtained spectral diffusion times was also influenced by changes in the electro-static environment of the dot over time.

6.5 Conclusion and future experiments

In summary, second order correlation measurements were carried out to determine the fast timescale spectral diffusion of single non-polar InGaN QDs, the first time for non-polar nitride dots. First, it was ascertained that the dot in question emitted single photons by measuring its second order correlation function with a spectral window including the whole of the dot line. This yielded an antibunching dip at zero delay with a depth of $g^2(0) = 0.13(13)$ after correction for the finite detector response time and the QW

background emission, proving single-photon emission. Reducing the spectral selection window of the HBT measurement to one half of the QD's linewidth resulted in an additional bunching peak. In order to extract its amplitude and decay time, the underlying pile-up decay was addressed, originating from the use of the start-stop HBT mode. Along with a power dependence calibration, the pile-up decay time was determined from the measured trace via an integration method. At the lowest excitation power density of $P = 2.9\,\mathrm{kW/cm^2} = 0.1 \cdot P_{\mathrm{sat}}$, the extracted spectral diffusion decay time proved to be with 860(160) ns longer than for any nitride dot, and in particular 2.5 times longer than for a polar InGaN dot used in a previous study. In line with previous reports, the power dependence of the inverse of the spectral diffusion time, the spectral diffusion rate, showed a linear increasing trend with increasing excitation power, due to an increased carrier density. Repeating the experiments on other dots demonstrated shorter and also even longer spectral diffusion times, as long as over one microsecond. This indicates that the detailed measurements presented in the first part of this chapter are not due to an outlier. Therefore, the non-polar InGaN dots exhibit comparable and in some cases longer spectral diffusion times than polar counterparts, despite higher *a*-plane dislocation densities. Due to their shorter lifetimes, the ratio of spectral diffusion time to lifetime is larger compared to polar dots.

This presents a first step towards the generation of indistinguishable photons with nitride QDs. To realise this successfully, firstly, pulsed excitation would be desirable in regard to applicability and finite detector response functions. Pulsed excitation experiments described in the first part of this chapter showed a fast lifetime of 413(3) ns, but also a reduced saturation count rate and signal-to-background ratio. These undesirable features would need further careful investigation and improvement. Secondly, in the field of arsenide QDs, it has been established that the use of quasi-resonant excitation into higher dot states, or even resonant excitation of the dot transition, increases the indistinguishability due to a reduced time-jitter and a lower carrier density. Thirdly, a cavity could help to further reduce the numbers of charge carriers in the vicinity a dot.

7 Conclusion

This thesis describes experimental studies of InGaN dots grown on the non-polar *a*-plane. It is focused on the electrical excitation of these dots, the lateral electric field built into them and its implications, among them reduced fast timescale spectral diffusion.

For the first time, electrically driven single-photon emission from a non-polar nitride dot was demonstrated. DC electrical excitation of a QD yielded the second order correlation value of $g^2(0) = 0.18(18)$ at 4.5 K after correction for the finite detector response time, proving the single-photon character of the dot emission. Furthermore, a study on more than 70 randomly selected QDs showed that 50% of them exhibit a degree of linear polarisation greater than 0.9. This agrees with PL studies on similar non-polar InGaN QDs, but is a considerably larger value than obtained for strain-engineered polar InGaN dots. Due to setup imperfections, the measured polarisation degree was only a lower bound. The mean polarisation angle was found to coincide with the crystallographic *m*-direction. 75% of the dots exhibited a polarisation angle within $\pm 10^\circ$ of the mean. It is unclear how much the setup imperfections were responsible for this spread in angles. Current dependent measurements allowed the identification of three biexciton-exciton pairs which exhibited a small biexciton binding energy with the range of ± 3 meV. A comparison with a reported simulation suggests a small QD height below 2.5 nm. Temperature-dependent measurements showed that the dot, of which the second order correlation function was measured, exhibited a constant intensity up to 50 K and vanished at 80 K, for a fixed voltage. Another dot showed EL up to a temperature of 130 K, demonstrating the potential for elevated temperature operation of *a*-plane InGaN

QDs. A hurdle in the way of realising single-photon emission at higher temperatures is the requirement of a reduced QW background emission. Additionally, pulsed excitation, needed for a useful single-photon source, comes with the challenge of delivering electrical pulses to the dot with a width much shorter than the dot's lifetime. This will require careful setup design, or choosing dots with longer lifetimes.

Another aspect covered in this thesis is the behaviour of emission lines of *a*-plane InGaN dots subjected to a lateral electric field. This is the first report on that topic for non-polar nitride dots. The field was generated by means of two opposing Schottky contacts evaporated on the sample surface. Only for one dot an increase in the emission linewidth could be observed. A fit derived with a simple semi-classical model gave a minimum lateral size of 6(1) nm and a minimum potential depth of 28(3) meV. This confinement is relatively shallow compared to previous reports of non-polar nitride InGaN dots and might explain why only one dot showed a linewidth increase, whereas all 60 other examined dots did not. For most of these, shifts in the emission energy could be observed. 10% of them showed a parabolic shift commonly seen in structures subjected to the QCSE. Small permanent dipoles ranging between $-0.44\,\mathrm{e\AA}$ and $+0.32\,\mathrm{e\AA}$ have been observed. Reported theoretical calculations of the built-in potential of non-polar InGaN dots agree with these findings as they qualitatively suggest a small in-built field which may be aligned parallel or anti-parallel to the polar direction depending on the relative contributions of the first and second order piezo-electricity. In the experiments, a mean in-built field of -3 kV/cm with a standard deviation of 11 kV/cm was observed, demonstrating a decrease by more than two orders of magnitude compared to the vertical field in polar InGaN dots. 62% of the examined dots exhibited an irregular energy shift, which could not be described by a parabola. It was concluded that this might be due to the particular implementation of the electrodes. Future experiments should take care to increase their quality and possibly add an Ohmic contact to allow for individual testing of each electrode. Additionally, it should be ensured that the direction of the polar axis is known from the beginning of the sample growth. Another surprising

observation was that for spectra containing several lines, some of them showed a similar energy shift behaviour, in contrast to the rest of the lines in the same spectrum. It was concluded that these are likely to originate from the same dot, being either multi-excitonic complexes in the case of small energy spacings between the lines or excited states in the case of larger energy differences. Further investigations should be able to distinguish between these possibilities through the power dependence and polarisation dependence of the lines, and photoluminescence excitation spectra. Both possibilities would present a valuable knowledge since the current understanding and identification of multi-excitonic complexes and excited states of nitride dots is rather in its infancy.

The final part of the thesis is focused on the fast timescale spectral diffusion experienced by *a*-plane InGaN dots. The aim of the first investigation of this kind on non-polar nitride dots was to clarify if for them the timescale of the fast spectral diffusion would be increased (due to an increased defect density) or decreased compared to polar dots (due to the reduced magnitude of the in-built dipole). A robust intensity correlation method was used which did not require interferometric stability. CW-laser excited HBT measurements of a part of a dot's linewidth featured not only an antibunching dip, but also a bunching peak decaying on a longer timescale. The decay time constant reflects how fast the electric environment of a dot changed, giving a measure of the timescale of the spectral diffusion. For a bright random dot it was found to be as long as 860(160) ns, which is at least 2.5 times longer than the longest spectral diffusion time previously reported for any other nitride dot. A proportionality between the excitation power density and the inverse of the spectral diffusion time was observed, in line with previous reports. Measurements on more *a*-plane dots found that spectral diffusion times ranged between 70(5) ns and 1170(50) ns. It was therefore be concluded that, compared to polar InGaN dots, *a*-plane InGaN QDs experience spectral diffusion on a similar, if not longer timescale despite an increased defect density of the samples. More importantly: the ratio of the spectral diffusion time and the emission lifetime is much more favourable for *a*-plane dots, because of consistently reduced lifetimes. Therefore, non-polar nitride

dots are more suitable to produce indistinguishable photons than polar nitride dots.

In the future, one of several key points to address is the use of cavities to increase the single-photon brightness by improving the outcoupling efficiency of non-polar InGaN dots. The easiest solution is a cavity with two distributed Bragg reflectors above and below the dots. An issue here is the trade-off between low refractive contrast of $Al_xIn_{1-x}N$ to GaN, and large lattice mismatch and therefore large strain of $Al_xGa_{1-x}N$ to GaN. This problem can be circumvented by using mesoporous distributed Bragg reflectors, which have already been demonstrated for polar InGaN/GaN dots [231].

Another potentially fruitful avenue lies in the pursuit of resonant excitation of nitride QDs. This would help to reduce background emission and drastically decrease the number of excited carriers, thus yielding longer spectral diffusion times. A successful implementation should significantly increase the degree of indistinguishability of single photons emitted by non-polar nitride dots, which has never been measured for any nitride dots due to strong spectral diffusion. An increased emission brightness by virtue of a cavity will be instrumental to make the experiment feasible in terms of acquisition time.

A last interesting point to study could the spread of biexciton binding energies of non-polar InGaN dots. One important, more general aspect is to gain a deeper understanding of the dot's parameters by means of this extra measurable quantity. A second aspect, aiming towards applications, is to investigate if some dots exhibit a negligible biexciton binding energy - which seems likely since for three dots it was found to be small - such that the biexciton cascade could be used to generate time-reordered entangled photon pairs [126]. If the opposite is the case and large biexciton binding energies are found for some dots, then the two-photon resonant excitation of the biexciton cascade could be used to reduce the background emission. Moreover, for arsenide dots, it has been shown both theoretically and experimentally that the lower bound to the single-photon purity due to re-excitation is reduced by resonant excitation of the three-level biexciton system compared to the direct excitation of the two-level excitonic transition [47].

8 Appendix

8.1 Samples

In Table 8.1, the samples are listed that were used for this thesis. More details could be obtained from Prof Rachel Oliver at the University of Cambridge, or Dr Tongtong Zhu in the same group. The QD layer of the samples C6379A and C5703E was embedded in a p-i-n junction. For the sample C6379A, the 2 μm-thick GaN bottom layer was Si-doped with a concentration of $3 \times 10^{18}\,\mathrm{cm}^{-3}$. The p-doped GaN top layer was 130 nm thick with a Mg dopant concentration of $3 \times 10^{19}\,\mathrm{cm}^{-3}$. For the sample C5703E, the QDs were embedded in a 50 nm unintentionally doped GaN layer, a 600 nm-thick Si-doped GaN layer on the bottom with a dopant concentration of $3 \times 10^{18}\,\mathrm{cm}^{-3}$ and a 200 nm-thick Mg-doped GaN layer on top with a dopant concentration of $3 \times 10^{19}\,\mathrm{cm}^{-3}$.

Sample number	Chapter	Growth method	ELOG	p-i-n?
C6379A	4	Q2T	no	yes
C5714F	5	Q2T	no	no
C5703E	6	MDE	yes (5μm wide stripes)	yes

Table 8.1: Samples used in the thesis.

8.2 Calculation of HBT trace fit accounting for the finite detector response time

If one has a single photon emitter with some background, one expects under continuous excitation an HBT-trace of the following form

$$g^{(2)}(\tau) = 1 - A \cdot \exp(-|\tau|/T) \tag{8.1}$$

with delay τ, the dip depth $g^{(2)}(0) = 1 - A$ and the time constant T. This assumes an emitter with an exponential decay, which is normally the case for our QDs. Suppose the instrument response function (IRF) can be approximated with a double-side single exponential decay

$$IRF(\tau) = C \cdot \exp(-|\tau|/R) \tag{8.2}$$

with the decay time R and a constant C. If T is comparable or shorter than R, a fit with Eq. (1) gives a larger value for $g^{(2)}(0)$ as well as for T than they actually are. In this regime, the measured HBT trace is the convolution of Eq. (1) and Eq. (2).

$$\begin{aligned} g_{\mathrm{m}}^{(2)}(\tau) &= IRF(\tau) * g^{(2)}(\tau) \\ &= \int_{-\infty}^{+\infty} IRF(t) \cdot g^{(2)}(\tau - t)\mathrm{d}t \\ &= \int_{-\infty}^{+\infty} C \cdot \exp\left(-\frac{|t|}{R}\right) \cdot \left(1 - A \cdot \exp\left(-\frac{|\tau - t|}{T}\right)\right)\mathrm{d}t \end{aligned}$$

To make things easier we look just at $\tau \geq 0$. But we do not loose information because the convolution of two symmetric functions generates a symmetric one as well. In the following we cut the second part of the integral into three pieces to get rid of the

modulus.

$$\begin{aligned} g_{\mathrm{m}}^{(2)}(\tau) = \quad & 2C \quad \cdot \int_0^{+\infty} \exp\left(-\frac{t}{R}\right) \mathrm{d}t \\ & - \quad AC \cdot \left[\int_{-\infty}^{0} \exp\left(+\frac{t}{R} - \frac{\tau - t}{T}\right) \mathrm{d}t \right. \\ & + \quad \int_0^{\tau} \exp\left(-\frac{t}{R} - \frac{\tau - t}{T}\right) \mathrm{d}t \\ & + \quad \left. \int_{\tau}^{+\infty} \exp\left(-\frac{t}{R} + \frac{\tau - t}{T}\right) \mathrm{d}t \right] \end{aligned}$$

Let us introduce two abbreviations

$$\oplus = \frac{1}{T} + \frac{1}{R} \quad \text{and} \quad \ominus = \frac{1}{T} - \frac{1}{R}.$$

That gives us

$$\begin{aligned} g_{\mathrm{m}}^{(2)}(\tau) = \quad & 2C \quad \cdot \int_0^{+\infty} \mathrm{e}^{-\frac{t}{R}} \mathrm{d}t \\ & - \quad AC \cdot \left(\int_{-\infty}^{0} \mathrm{e}^{-\frac{\tau}{T}} \cdot \mathrm{e}^{t\oplus} \mathrm{d}t + \int_0^{\tau} \mathrm{e}^{-\frac{\tau}{T}} \cdot \mathrm{e}^{t\ominus} \mathrm{d}t + \int_{\tau}^{+\infty} \mathrm{e}^{+\frac{\tau}{T}} \cdot \mathrm{e}^{-t\oplus} \mathrm{d}t \right) \\ = \quad & 2C \quad \cdot \left[-R \cdot \mathrm{e}^{-\frac{t}{R}} \right]_0^{+\infty} \\ & - \quad AC \cdot \left(\mathrm{e}^{-\frac{\tau}{T}} \cdot \left[\frac{1}{\oplus} \mathrm{e}^{t\oplus} \right]_{-\infty}^{0} + \mathrm{e}^{-\frac{\tau}{T}} \cdot \left[\frac{1}{\ominus} \mathrm{e}^{t\ominus} \right]_0^{\tau} + \mathrm{e}^{+\frac{\tau}{T}} \cdot \left[-\frac{1}{\oplus} \mathrm{e}^{-t\oplus} \right]_{\tau}^{+\infty} \right) \\ = \quad & 2CR \quad -AC \left(\mathrm{e}^{-\frac{\tau}{T}} \cdot \left(\frac{1}{\oplus} + \frac{1}{\ominus} \cdot \mathrm{e}^{\ominus\tau} - \frac{1}{\ominus} \right) + \mathrm{e}^{+\frac{\tau}{T}} \cdot \frac{1}{\oplus} \cdot \mathrm{e}^{-\oplus\tau} \right) \\ = \quad & 2CR \quad -AC \left(\left(\frac{1}{\oplus} - \frac{1}{\ominus} \right) \cdot \mathrm{e}^{-\frac{\tau}{T}} + \frac{1}{\ominus} \cdot \mathrm{e}^{-\frac{\tau}{T}} \cdot \mathrm{e}^{\ominus\tau} + \frac{1}{\oplus} \cdot \mathrm{e}^{+\frac{\tau}{T} \cdot \mathrm{e}^{-\oplus\tau}} \right) \end{aligned}$$

Here, we make one small side calculation, which is simplifying the expressions coloured red and blue above.

$$\begin{aligned} \mathrm{e}^{\frac{\tau}{H}} \mathrm{e}^{-\oplus\tau} \quad &= \quad \mathrm{e}^{\frac{\tau}{T} - \tau\left(\frac{1}{T} + \frac{1}{R}\right)} = \mathrm{e}^{-\frac{\tau}{R}} \\ \text{or} \quad \mathrm{e}^{-\frac{\tau}{T}} \mathrm{e}^{\ominus\tau} \quad &= \quad \mathrm{e}^{\tau\left(-\frac{1}{T} + \frac{1}{T} - \frac{1}{R}\right)} = \mathrm{e}^{-\frac{\tau}{R}} \end{aligned}$$

That yields the following.

$$\begin{aligned} g_{\mathrm{m}}^{(2)}(\tau) &= 2CR - AC\left(\left(\frac{1}{\oplus} - \frac{1}{\ominus}\right)\cdot \mathrm{e}^{-\frac{\tau}{T}} + \frac{1}{\ominus}\cdot \mathrm{e}^{-\frac{\tau}{R}} + \frac{1}{\oplus}\cdot \mathrm{e}^{-\frac{\tau}{R}}\right) \\ &= 2CR - AC\left(\left(\frac{1}{\oplus} - \frac{1}{\ominus}\right)\cdot \mathrm{e}^{-\frac{\tau}{T}} + \left(\frac{1}{\ominus} + \frac{1}{\oplus}\right)\cdot \mathrm{e}^{-\frac{\tau}{R}}\right) \end{aligned}$$

Now we simplify the expressions coloured green above.

$$\begin{aligned} \frac{1}{\oplus} \pm \frac{1}{\ominus} &= \frac{1}{\frac{1}{T}+\frac{1}{R}} \pm \frac{1}{\frac{1}{T}-\frac{1}{R}} \\ &= \frac{1}{\frac{R+T}{RT}} \pm \frac{1}{\frac{R-T}{RT}} \\ &= \frac{RT}{R+T} \pm \frac{RT}{R-T} \\ &= \frac{RT(R-T) \pm RT(R+T)}{R^2-T^2} \end{aligned}$$

That gives for "+" $2TR^2/(R^2-T^2)$ and for "-" $-2T^2R/(R^2-T^2)$. With successive use of simplification (1) and then (2) we get

$$\begin{aligned} g_{m}^{(2)}(\tau) &= 2CR - AC\left(\frac{-2TR^2}{R^2-T^2}\cdot \mathrm{e}^{-\frac{\tau}{T}} + \frac{2T^2R}{R^2-T^2}\cdot \mathrm{e}^{-\frac{\tau}{R}}\right) \\ &= 2CR - \frac{2ACTR}{R^2-T^2}\left(R\cdot \mathrm{e}^{-\frac{\tau}{R}} - T\cdot \mathrm{e}^{-\frac{\tau}{T}}\right) \end{aligned}$$

Now we just need to normalise this convolution to 1 for $\tau \to +\infty$. In that case $g_{m}^{(2)}(\tau) = 2CR$. So the normalised second order correlation function accounting for a finite detector response time is

$$g_{\mathrm{m,norm}}^{(2)}(\tau) = 1 - \frac{AT}{R^2-T^2}\left(R\cdot \mathrm{e}^{-\frac{\tau}{R}} - T\cdot \mathrm{e}^{-\frac{\tau}{T}}\right). \tag{8.3}$$

This form is the same as Equation (4.5) with $|\tau|$ for τ as it is symmetric in τ. A quick check: For an ideal detector with $R \to 0$ we get $g_{\mathrm{m,norm}}^{(2)}(\tau) = 1 - A\mathrm{e}^{-\frac{\tau}{T}}$, which is identical to Equation (8.1) with $T = H$.

Bibliography

[1] M. Fox, *Quantum Optics, an Introduction* (Oxford University Press, 2006). 1, 21

[2] C. H. Bennett and G. Brassard, "Quantum Cryptography: Public Key Distribution and Coin Tossing" in "Proc. IEEE Int. Conf. Comput. Syst. Signal Process.", (Bangalore, India, 1984), p. 175. 2, 53, 59, 102

[3] A. K. Ekert, "Quantum Cryptography Based on Bell's Theorem" Phys. Rev. Lett. **67**, 661 (1991). 2

[4] N. Gisin, G. Ribordy, W. Tittel, and H. Zbinden, "Quantum Cryptography" Rev. Mod. Phys. **74**, 145 (2002). 2

[5] V. Scarani, H. Bechmann-Pasquinucci, N. J. Cerf, M. Dusek, N. Lütkenhaus, and M. Peev, "The Security of Practical Quantum Key Distribution" Rev. Mod. Phys. **81**, 1301 (2009). 2, 102

[6] R. L. Rivest, A. Shamir, and L. M. Adleman, "Cryptographic Communications System and Method" US Patent 4405829A, filed Dec. 14, 1977, and issued Sept. 20, 1983. 2

[7] S. Buckley, K. Rivoire, and J. Vučković, "Engineered Quantum Dot Single-Photon Sources" Rep. Prog. Phys. **75**, 126503 (2012). 2, 3, 5, 22

[8] W. K. Wootters and W. H. Zurek, "A Single Quantum Cannot Be Cloned" Nature **299**, 802 (1982). 2, 3

[9] T. Heindel, C. A. Kessler, M. Rau, C. Schneider, M. Fürst, F. Hargart, W. M. Schulz, M. Eichfelder, R. Roßbach, S. Nauerth, M. Lermer, H. Weier, M. Jetter, M. Kamp, S. Reitzenstein, S. Höfling, P. Michler, H. Weinfurter, and A. Forchel, "Quantum Key Distribution Using Quantum Dot Single-Photon Emitting Diodes in the Red and Near Infrared Spectral Range" New J. Phys. **14**, 083001 (2012). 2, 68

[10] K. Takemoto, Y. Nambu, T. Miyazawa, Y. Sakuma, T. Yamamoto, S. Yorozu, and Y. Arakawa, "Quantum Key Distribution over 120 km Using Ultrahigh Purity Single-Photon Source and Superconducting Single-Photon Detectors" Sci. Rep. **5**, 14383 (2015). 2

[11] Q. Zhang, F. Xu, Y.-A. Chen, C.-Z. Peng, and J.-W. Pan, "Large Scale Quantum Key Distribution: Challenges and Solutions [Invited]" Opt. Express **26**, 24260 (2018). 2

[12] H. K. Lo, X. Ma, and K. Chen, "Decoy State Quantum Key Distribution" Phys. Rev. Lett. **94**, 15 (2005). 2

[13] X.-B. Wang, "Beating the Photon-Number-Splitting Attack in Practical Quantum Cryptography" Phys. Rev. Lett. **94**, 230503 (2005). 2

[14] Z. Yuan, A. Plews, R. Takahashi, K. Doi, W. Tam, A. W. Sharpe, A. R. Dixon, E. Lavelle, J. F. Dynes, A. Murakami, M. Kujiraoka, M. Lucamarini, Y. Tanizawa, H. Sato, and A. J. Shields, "10 Mb/s Quantum Key Distribution" J. Light. Technol. **36**, 3427 (2018). 2

[15] S. Unsleber, Y.-M. He, S. Gerhardt, S. Maier, C.-Y. Lu, J.-W. Pan, N. Gregersen, M. Kamp, C. Schneider, and S. Höfling, "Highly Indistinguishable On-Demand Resonance Fluorescence Photons from a Deterministic Quantum Dot Micropillar Device with 74% Extraction Efficiency" Opt. Express **24**, 8539 (2016). 3, 6

[16] H.-J. Briegel, W. Dür, J. I. Cirac, and P. Zoller, "Quantum Repeaters: The Role of Imperfect Local Operations in Quantum Communication" Phys. Rev. Lett. **81**, 5932 (1998). 3

[17] N. Sangouard, C. Simon, H. De Riedmatten, and N. Gisin, "Quantum Repeaters Based on Atomic Ensembles and Linear Optics" Rev. Mod. Phys. **83**, 33 (2011). 3

[18] H. J. Kimble, "The Quantum Internet" Nature **453**, 1023 (2008). 3

[19] S. Wehner, D. Elkouss, and R. Hanson, "Quantum Internet: A Vision for the Road Ahead" Science **362**, eaam9288 (2018). 3

[20] H. Wang, H. Hu, T. H. Chung, J. Qin, X. Yang, J. P. Li, R. Z. Liu, H. S. Zhong, Y. M. He, X. Ding, Y. H. Deng, Q. Dai, Y. H. Huo, S. Höfling, C. Y. Lu, and J. W. Pan, "On-Demand Semiconductor Source of Entangled Photons Which Simultaneously Has High Fidelity, Efficiency, and Indistinguishability" Phys. Rev. Lett. **122**, 1 (2019). 3, 6

[21] P. W. Shor, "Algorithms for Quantum Computation: Discrete Logarithms and Factoring" in "Proc. 35th Annu. Symp. Found. Comput. Sci.", (1994), p. 124. 3

[22] E. Knill, R. Laflamme, and G. J. Milburn, "A Scheme for Efficient Quantum Computation with Linear Optics" Nature **409**, 46 (2001). 3

[23] J. Carolan, C. Harrold, C. Sparrow, E. Martín-López, N. J. Russell, J. W. Silverstone, P. J. Shadbolt, N. Matsuda, M. Oguma, M. Itoh, G. D. Marshall, M. G. Thompson, J. C. Matthews, T. Hashimoto, J. L. O'Brien, and A. Laing, "Universal Linear Optics" Science **349**, 711 (2015). 3, 4

[24] M. Varnava, D. E. Browne, and T. Rudolph, "How Good Must Single Photon Sources and Detectors Be for Efficient Linear Optical Quantum Computation?" Phys. Rev. Lett. **100**, 60502 (2008). 4

[25] Y.-X. Gong, X.-B. Zou, T. C. Ralph, S.-N. Zhu, and G.-C. Guo, "Linear Optical Quantum Computation with Imperfect Entangled Photon-Pair Sources and Inefficient Non-Photon-Number-Resolving Detectors" Phys. Rev. A **81**, 52303 (2010). 4

[26] R. Valivarthi, I. Lucio-Martinez, P. Chan, A. Rubenok, C. John, D. Korchinski, C. Duffin, F. Marsili, V. Verma, M. D. Shaw, J. A. Stern, S. W. Nam, D. Oblak, Q. Zhou, J. A. Slater, and W. Tittel, "Measurement-Device-Independent Quantum Key Distribution: From Idea Towards Application" J. Mod. Optic. **62**, 1141 (2015). 4

[27] S. Aaronson and A. Arkhipov, "The Computational Complexity of Linear Optics" in "Proc. 43rd Annu. ACM Symp. Theory Comput.", (2011), p. 333. 4

[28] H. Wang, J. Qin, X. Ding, M. C. Chen, S. Chen, X. You, Y. M. He, X. Jiang, L. You, Z. Wang, C. Schneider, J. J. Renema, S. Höfling, C. Y. Lu, and J. W. Pan, "Boson Sampling with 20 Input Photons and a 60-Mode Interferometer in a 10^{14} -Dimensional Hilbert Space" Phys. Rev. Lett. **123**, 250503 (2019). 4

[29] B. Lounis and M. Orrit, "Single-Photon Sources" Rep. Prog. Phys. **68**, 1129 (2005). 4

[30] V. Giovannetti, S. Lloyd, and L. MacCone, "Advances in Quantum Metrology" Nat. Photonics **5**, 222 (2011). 5

[31] I. Afek, O. Ambar, and Y. Silberberg, "High-NOON States by Mixing Quantum and Classical Light" Science **328**, 879 (2010). 5

[32] J. C. Loredo, C. Antón, B. Reznychenko, P. Hilaire, A. Harouri, C. Millet, H. Ollivier, N. Somaschi, L. De Santis, A. Lemaître, I. Sagnes, L. Lanco, A. Auffèves, O. Krebs, and P. Senellart, "Generation of Non-Classical Light in a Photon-Number Superposition" Nat. Photonics **13**, 803 (2019). 5

[33] P. Senellart, G. Solomon, and A. White, "High-Performance Semiconductor Quantum-Dot Single-Photon Sources" Nat. Nanotechnol. **12**, 1026 (2017). 5

[34] S. Castelletto, B. C. Johnson, V. Ivády, N. Stavrias, T. Umeda, A. Gali, and T. Ohshima, "A Silicon Carbide Room-Temperature Single-Photon Source" Nat. Mater. **13**, 151 (2014). 5

[35] A. J. Morfa, B. C. Gibson, M. Karg, T. J. Karle, A. D. Greentree, P. Mulvaney, and S. Tomljenovic-Hanic, "Single-Photon Emission and Quantum Characterization of Zinc Oxide Defects" Nano Lett. **12**, 949 (2012). 5

[36] T. T. Tran, K. Bray, M. J. Ford, M. Toth, and I. Aharonovich, "Quantum Emission from Hexagonal Boron Nitride Monolayers" Nat. Nanotechnol. **11**, 37 (2016). 5

[37] Y. Zhou, Z. Wang, A. Rasmita, S. Kim, A. Berhane, Z. Bodrog, G. Adamo, A. Gali, I. Aharonovich, and W. Gao, "Room Temperature Solid-State Quantum Emitters in the Telecom Range" Sci. Adv. **4**, eaar3580 (2018). 5

[38] I. Aharonovich and E. Neu, "Diamond Nanophotonics" Adv. Opt. Mater. **2**, 911 (2014). 5, 6

[39] I. Aharonovich, D. Englund, and M. Toth, "Solid-State Single-Photon Emitters" Nat. Photonics **10**, 631 (2016). 6

[40] D. Riedel, I. Söllner, B. J. Shields, S. Starosielec, P. Appel, E. Neu, P. Maletinsky, and R. J. Warburton, "Deterministic Enhancement of Coherent Photon Generation from a Nitrogen-Vacancy Center in Ultrapure Diamond" Phys. Rev. X **7**, 31040 (2017). 6

[41] H. Bernien, L. Childress, L. Robledo, M. Markham, D. Twitchen, and R. Hanson, "Two-Photon Quantum Interference from Separate Nitrogen Vacancy Centers in Diamond" Phys. Rev. Lett. **108**, 43604 (2012). 6

[42] T. B. Hoang, G. M. Akselrod, and M. H. Mikkelsen, "Ultrafast Room-Temperature Single Photon Emission from Quantum Dots Coupled to Plasmonic Nanocavities" Nano Lett. **16**, 270 (2016). 6

[43] F. Liu, L. Biadala, A. V. Rodina, D. R. Yakovlev, D. Dunker, C. Javaux, J.-P. Hermier, A. L. Efros, B. Dubertret, and M. Bayer, "Spin Dynamics of Negatively Charged Excitons in CdSe/CdS Colloidal Nanocrystals" Phys. Rev. B **88**, 35302 (2013). 6

[44] H. Utzat, W. Sun, A. E. K. Kaplan, F. Krieg, M. Ginterseder, B. Spokoyny, N. D. Klein, K. E. Shulenberger, C. F. Perkinson, M. V. Kovalenko, and M. G. Bawendi, "Coherent Single-Photon Emission from Colloidal Lead Halide Perovskite Quantum Dots" Science **363**, 1068 (2019). 6

[45] X. Lin, X. Dai, C. Pu, Y. Deng, Y. Niu, L. Tong, W. Fang, Y. Jin, and X. Peng, "Electrically-Driven Single-Photon Sources Based on Colloidal Quantum Dots with Near-Optimal Antibunching at Room Temperature" Nat. Commun. **8**, 1132 (2017). 6

[46] A. P. Beyler, L. F. Marshall, J. Cui, X. Brokmann, and M. G. Bawendi, "Direct Observation of Rapid Discrete Spectral Dynamics in Single Colloidal CdSe-CdS Core-Shell Quantum Dots" Phys. Rev. Lett. **111**, 177401 (2013). 6

[47] L. Hanschke, K. A. Fischer, S. Appel, D. Lukin, J. Wierzbowski, S. Sun, R. Trivedi, J. Vučković, J. J. Finley, and K. Müller, "Quantum Dot Single Photon Sources with Ultra-Low Multi-Photon Probability" npj Quantum Inf. **4**, 2056 (2018). 6, 73, 129

[48] N. Somaschi, V. Giesz, L. De Santis, J. C. Loredo, M. P. Almeida, G. Hornecker, S. L. Portalupi, T. Grange, C. Antón, J. Demory, C. Gómez, I. Sagnes, N. D. Lanzillotti-Kimura, A. Lemaítre, A. Auffeves, A. G. White, L. Lanco, and P. Senellart, "Near-Optimal Single-Photon Sources in the Solid State" Nat. Photonics **10**, 340 (2016). 6, 110

[49] E. Schöll, L. Hanschke, L. Schweickert, K. D. Zeuner, M. Reindl, S. F. Covre Da Silva, T. Lettner, R. Trotta, J. J. Finley, K. Müller, A. Rastelli, V. Zwiller, and K. D. Jöns, "Resonance Fluorescence of GaAs Quantum Dots with Near-Unity Photon Indistinguishability" Nano Lett. **19**, 2404 (2019). 6

[50] Ł. Dusanowski, S. H. Kwon, C. Schneider, and S. Höfling, "Near-Unity Indistinguishability Single Photon Source for Large-Scale Integrated Quantum Optics" Phys. Rev. Lett. **122**, 173602 (2019). 6

[51] J. Kettler, M. Paul, F. Olbrich, K. Zeuner, M. Jetter, and P. Michler, "Single-Photon and Photon Pair Emission from MOVPE-Grown In(Ga)As Quantum Dots: Shifting the Emission Wavelength from 1.0 μm to 1.3 μm" Appl. Phys. B-Lasers O. **122**, 48 (2016). 6

[52] C. Nawrath, F. Olbrich, M. Paul, S. L. Portalupi, M. Jetter, and P. Michler, "Coherence and Indistinguishability of Highly Pure Single Photons from Non-Resonantly and Resonantly Excited Telecom C-Band Quantum Dots" Appl. Phys. Lett. **115**, 023103 (2019). 6, 120

[53] S. K. Patra and S. Schulz, "Exploring the Potential of c-Plane Indium Gallium Nitride Quantum Dots for Twin-Photon Emission" Nano Lett. **20**, 234 (2020). 7, 17, 19

[54] M. J. Holmes, S. Kako, K. Choi, M. Arita, and Y. Arakawa, "Single Photons from a Hot Solid-State Emitter at 350 K" ACS Photonics **3**, 543 (2016). 7, 102, 103

[55] S. Deshpande, T. Frost, A. Hazari, and P. Bhattacharya, "Electrically Pumped Single-Photon Emission at Room Temperature from a Single InGaN/GaN Quantum Dot" Appl. Phys. Lett. **105**, 141109 (2014). 7, 23, 39, 40, 71

[56] L. Zhang, C. H. Teng, P. C. Ku, and H. Deng, "Site-Controlled InGaN/GaN Single-Photon-Emitting Diode" Appl. Phys. Lett. **108**, 153102 (2016). 7, 23, 39, 40, 52, 64, 68

[57] J. Li, K. B. Nam, M. L. Nakarmi, J. Y. Lin, H. X. Jiang, P. Carrier, and S.-H. Wei, "Band Structure and Fundamental Optical Transitions in Wurtzite AlN" Appl. Phys. Lett. **83**, 5163 (2003). 7

[58] H. P. Maruska and J. J. Tietjen, "The Preparation and Properties of Vapor-Deposited Single-Crystal-Line GaN" Appl. Phys. Lett. **15**, 327 (1969). 7

[59] V. Davydov, A. A. Klochikhin, R. P. Seisyan, V. V. Emtsev, S. V. Ivanov, F. Bechstedt, J. Furthmueller, H. Harima, A. V. Mudryi, J. Aderhold, O. Semchinova, and J. Graul, "Absorption and Emission of Hexagonal InN. Evidence of Narrow Fundamental Band Gap" Phys. Status Solidi B **229**, r1 (2002). 7

[60] S. Z. Wang, S. F. Yoon, Y. X. Xia, and S. W. Xie, "20 MeV-Deep Donor Level in InN Film of 0.76 EV Band Gap Grown by Plasma-Assisted Nitrogen Source" J. Appl. Phys. **95**, 7998 (2004). 7

[61] M. J. Holmes, K. Choi, S. Kako, M. Arita, and Y. Arakawa, "Room-Temperature Triggered Single Photon Emission from a III-Nitride Site-Controlled Nanowire Quantum Dot" Nano Lett. **14**, 982 (2014). 7, 63, 112

[62] J.-H. Cho, Y. M. Kim, S.-H. Lim, H.-S. Yeo, S. Kim, S. Gong, and Y.-H. Cho, "Strongly Coherent Single Photon Emission from Site-Controlled InGaN Quantum Dots Embedded in GaN Nano-Pyramids" ACS Photonics **5**, 439 (2017). 7, 24, 103

[63] T. Wang, T. J. Puchtler, T. Zhu, J. C. Jarman, L. P. Nuttall, R. A. Oliver, and R. A. Taylor, "Polarisation-Controlled Single Photon Emission at High Temperatures from InGaN Quantum Dots" Nanoscale **9**, 9421 (2017). 7, 63, 66, 68, 91, 103

[64] B. P. L. Reid, T. Zhu, C. C. S. Chan, C. Kocher, F. Oehler, R. Emery, M. J. Kappers, R. A. Oliver, and R. A. Taylor, "High Temperature Stability in Non-Polar $(11\bar{2}0)$ InGaN Quantum Dots: Exciton and Biexciton Dynamics" Phys. Status Solidi C **11**, 702 (2014). 7, 51, 61, 65, 98

[65] B. P. L. Reid, C. Kocher, T. Zhu, F. Oehler, C. C. S. Chan, R. A. Oliver, and R. A. Taylor, "Non-Polar InGaN Quantum Dot Emission with Crystal-Axis Oriented Linear Polarization" Appl. Phys. Lett. **106**, 171108 (2015). 7, 20, 52, 53

[66] T. Wang, T. J. Puchtler, S. K. Patra, T. Zhu, M. Ali, T. J. Badcock, T. Ding, R. A. Oliver, S. Schulz, and R. A. Taylor, "Direct Generation of Linearly Polarized Single Photons with a Deterministic Axis in Quantum Dots" Nanophotonics **6**, 1175 (2017). 7, 14, 15, 17, 18, 19, 25, 52, 53, 58, 59, 60

[67] C.-Y. Yeh, Z. W. Lu, S. Froyen, and A. Zunger, "Zinc-Blende–Wurtzite Polytypism in Semiconductors" Phys. Rev. B **46**, 10086 (1992). 10

[68] T. J. Puchtler, "Development of Stucture and Materials for InGaN/GaN Cavity-Quantum Electrodynamics" Ph.D. thesis, University of Cambridge (2015). 11

[69] F. Bernardini, V. Fiorentini, and D. Vanderbilt, "Spontaneous Polarization and Piezoelectric Constants of III-V Nitrides" Phys. Rev. B **56**, R10024 (1997). 11

[70] I. Vurgaftman and J. R. Meyer, "Band Parameters for Nitrogen-Containing Semiconductors" J. Appl. Phys. **94**, 3675 (2003). 11

[71] O. Ambacher, "Growth and Applications of Group III-Nitrides" J. Phys. D. Appl. Phys. **31**, 2653 (1998). 12

[72] T. Takeuchi, C. Wetzel, S. Yamaguchi, H. Sakai, H. Amano, I. Akasaki, Y. Kaneko, S. Nakagawa, Y. Yamaoka, and N. Yamada, "Determination of Piezoelectric Fields in Strained GaInN Quantum Wells Using the Quantum-Confined Stark Effect" Appl. Phys. Lett. **73**, 1691 (1998). 12

[73] N. Grandjean and M. Ilegems, "Visible InGaN/GaN Quantum-Dot Materials and Devices" Proc. IEEE **95**, 1853 (2007). 12

[74] A. F. Jarjour, R. A. Oliver, A. Tahraoui, M. J. Kappers, R. A. Taylor, and C. J. Humphreys, "Experimental and Theoretical Study of the Quantum-Confined Stark Effect in a Single InGaN/GaN Quantum Dot Under Applied Vertical Electric Field" Superlattices Microst. **43**, 431 (2008). 12, 85, 93

[75] D. A. B. Miller, D. S. Chemla, T. C. Damen, A. C. Gossard, W. Wiegmann, T. H. Wood, and C. A. Burrus, "Band-Edge Electroabsorption in Quantum Well Structures: The Quantum-Confined Stark Effect" Phys. Rev. Lett. **53**, 2173 (1984). 12

[76] C. Cohen-Tannoudji, B. Diu, F. Laloë, S. R. Hemley, N. Ostrowsky, and D. B. Ostrowsky, *Quantum Mechanics. Volume II, Angular Momentum, Spin, and Approximation Methods* (WILEY-VCH Verlag, Weinheim, 2019), 2nd ed. 12

[77] S. Schulz, T. J. Badcock, M. A. Moram, P. Dawson, M. J. Kappers, C. J. Humphreys, and E. P. O'Reilly, "Electronic and Optical Properties of Nonpolar a-Plane GaN Quantum Wells" Phys. Rev. B **82**, 125318 (2010). 14, 15, 16, 52

[78] W. Bi, H. Kuo, P. Ku, and B. Shen, eds., *Handbook of GaN Semiconductor Materials and Devices* (CDC Press, 2017). 14

[79] D. Sutherland, "Optical Characterisation of Non-Polar InGaN/GaN Quantum Wells" Ph.D. thesis, University of Manchester (2015). 14

[80] J. Kim, S. Lee, J. Oh, J. Ryu, Y. Park, S.-H. Park, and E. Yoon, "Highly Polarized Photoluminescence from c-Plane InGaN/GaN Multiple Quantum Wells on Stripe-Shaped Cavity-Engineered Sapphire Substrate" Sci. Rep. **9**, 8282 (2019). 16

[81] D. Kundys, D. Sutherland, M. J. Davies, F. Oehler, J. Griffiths, P. Dawson, M. J. Kappers, C. J. Humphreys, S. Schulz, F. Tang, and R. A. Oliver, "A Study of the Optical and Polarisation Properties of InGaN/GaN Multiple Quantum Wells Grown on a-Plane and m-Plane GaN Substrates" Sci. Technol. Adv. Mat. **17**, 736 (2016). 16, 52, 53, 58

[82] F. Tang, T. Zhu, W. Y. Fu, F. Oehler, S. Zhang, J. T. Griffiths, C. Humphreys, T. L. Martin, P. A. Bagot, M. P. Moody, S. K. Patra, S. Schulz, P. Dawson, S. Church, J. Jacobs, and R. A. Oliver, "Insight into the Impact of Atomic- and Nano-Scale Indium Distributions on the Optical Properties of InGaN/GaN Quantum Well Structures Grown on m-Plane Freestanding GaN Substrates" J. Appl. Phys. **125**, 225704 (2019). 17

[83] S. Amloy, K. F. Karlsson, T. G. Andersson, and P. O. Holtz, "On the Polarized Emission from Exciton Complexes in GaN Quantum Dots" Appl. Phys. Lett. **100**, 021901 (2012). 17

[84] A. Lundskog, C.-W. Hsu, K. Fredrik Karlsson, S. Amloy, D. Nilsson, U. Forsberg, P. Olof Holtz, and E. Janzén, "Direct Generation of Linearly Polarized Photon Emission with Designated Orientations from Site-Controlled InGaN Quantum Dots" Light Sci. Appl. **3**, e139 (2014). 17, 52, 53, 58, 60

[85] C. H. Teng, L. Zhang, T. A. Hill, B. Demory, H. Deng, and P. C. Ku, "Elliptical Quantum Dots As On-Demand Single Photons Sources with Deterministic Polarization States" Appl. Phys. Lett. **107**, 191105 (2015). 17, 52, 53, 58, 60

[86] T. Wang, "Non-Polar InGaN Quantum Dots: Polarisation-Controlled Semiconductor Single-Photon Sources at On-Chip Temperatures" Ph.D. thesis, University of Oxford (2019). 19, 29

[87] R. M. Stevenson, R. J. Young, P. See, D. G. Gevaux, K. Cooper, P. Atkinson, I. Farrer, D. A. Ritchie, and A. J. Shields, "Magnetic-Field-Induced Reduction of the Exciton Polarization Splitting in InAs Quantum Dots" Phys. Rev. B **73**, 033306 (2006). 19

[88] S. Amloy, Y. T. Chen, K. F. Karlsson, K. H. Chen, H. C. Hsu, C. L. Hsiao, L. C. Chen, and P. O. Holtz, "Polarization-Resolved Fine-Structure Splitting of Zero-Dimensional $In_xGa_{1-X}N$ Excitons" Phys. Rev. B **83**, 201307 (2011). 19, 20, 52

[89] R. J. Young, R. M. Stevenson, A. J. Shields, P. Atkinson, K. Cooper, D. A. Ritchie, K. M. Groom, A. I. Tartakovskii, and M. S. Skolnick, "Inversion of Exciton Level Splitting in Quantum Dots" Phys. Rev. B **72**, 113305 (2005). 19, 58

[90] T. Wang, T. J. Puchtler, T. Zhu, J. C. Jarman, C. C. Kocher, R. A. Oliver, and R. A. Taylor, "Temperature-Dependent Fine Structure Splitting in InGaN Quantum Dots" Appl. Phys. Lett. **111**, 053101 (2017). 20

[91] L. Zhang, C.-H. Teng, P.-C. Ku, and H. Deng, "Charge-Tunable Indium Gallium Nitride Quantum Dots" Phys. Rev. B **93**, 085301 (2016). 20, 98

[92] P. Michler, ed., *Single Semiconductor Quantum Dots* (Springer, 2010). 22

[93] P. Michler, A. Kiraz, C. Becher, W. V. Schoenfeld, P. M. Petroff, L. Zhang, E. Hu, and A. Imamoğlu, "A Quantum Dot Single-Photon Turnstile Device" Science **290**, 2282 (2000). 22

[94] P. Gibart, "Metal Organic Vapour Phase Epitaxy of GaN and Lateral Overgrowth" Rep. Prog. Phys. **67**, 667 (2004). 23, 103

[95] S. Deshpande, J. Heo, A. Das, and P. Bhattacharya, "Electrically Driven Polarized Single-Photon Emission from an InGaN Quantum Dot in a GaN Nanowire" Nat. Commun. **4**, 1675 (2013). 23, 39, 52, 61, 63, 64

[96] T. Zhu, F. Oehler, B. Reid, R. M. Emery, R. A. Taylor, M. J. Kappers, and R. A. Oliver, "Non-Polar (11$\bar{2}$0) InGaN Quantum Dots with Short Exciton Lifetimes Grown by Metal-Organic Vapour Phase Epitaxy" Appl. Phys. Lett. **102**, 698 (2013). 23, 24, 25, 76, 103

[97] M. Holmes, S. Kako, K. Choi, P. Podemski, M. Arita, Y. Arakawa, and G. Qd, "Temperature Dependent Photoluminescence Excitation Spectroscopy of GaN Quantum Dots in Site Controlled GaN/AlGaN Nanowires" Jpn. J. Appl. Phys. **52**, 08LJ02 (2013). 24

[98] T. Jemsson, H. Machhadani, P. O. Holtz, and K. F. Karlsson, "Polarized Single Photon Emission and Photon Bunching from an InGaN Quantum Dot on a GaN Micropyramid" Nanotechnology **26**, 065702 (2015). 24, 52, 61

[99] T. Wang, T. J. Puchtler, T. Zhu, J. C. Jarman, R. A. Oliver, and R. A. Taylor, "High Temperature Performance of Non-Polar (11$\bar{2}$0) InGaN Quantum Dots Grown by a Quasi-Two-Temperature Method" Phys. Status Solidi B **254**, 1600724 (2017). 24, 26

[100] B. P. L. Reid, T. Zhu, T. J. Puchtler, L. J. Fletcher, C. C. S. Chan, R. A. Oliver, and R. A. Taylor, "Origins of Spectral Diffusion in the Micro-Photoluminescence of Single InGaN Quantum Dots" Jpn. J. Appl. Phys. **52**, 08JE01 (2013). 24, 49, 66, 102, 103

[101] N. Koguchi and K. Ishige, "Growth of GaAs Epitaxial Microcrystals on an S-Terminated GaAs Substrate by Successive Irradiation of Ga and As Molecular Beams" Jpn. J. Appl. Phys. **32**, 2052 (1993). 25

[102] M. Gurioli, Z. Wang, A. Rastelli, T. Kuroda, and S. Sanguinetti, "Droplet Epitaxy of Semiconductor Nanostructures for Quantum Photonic Devices" Nat. Mater. **18**, 799 (2019). 25, 103

[103] R. A. Oliver, G. A. D. Briggs, M. J. Kappers, C. J. Humphreys, S. Yasin, J. H. Rice, J. D. Smith, and R. A. Taylor, "InGaN Quantum Dots Grown by Metalorganic Vapor Phase Epitaxy Employing a Post-Growth Nitrogen Anneal" Appl. Phys. Lett. **83**, 755 (2003). 25

[104] H. Springbett, "Microscopy and Spectroscopy of Materials for Blue Single Photon Sources" Ph.D. thesis, University of Cambridge (2018). 25

[105] J. T. Griffiths, T. Zhu, F. Oehler, R. M. Emery, W. Y. Fu, B. P. L. Reid, R. A. Taylor, M. J. Kappers, C. J. Humphreys, and R. A. Oliver, "Growth of Non-Polar (11$\bar{2}$0) InGaN Quantum Dots by Metal Organic Vapour Phase Epitaxy Using a Two Temperature Method" APL Mater. **2**, 126101 (2014). 26

[106] A. F. Jarjour, A. M. Green, T. J. Parker, R. A. Taylor, R. A. Oliver, G. A. D. Briggs, M. J. Kappers, C. J. Humphreys, R. W. Martin, and I. M. Watson, "Two-Photon Absorption from Single InGaN/GaN Quantum Dots" Physica E **32**, 119 (2006). 28

[107] D. Collins, A. Jarjour, M. Hadjipanayi, R. Taylor, R. Oliver, M. Kappers, C. Humphreys, and A. Tahraoui, "Two-Photon Autocorrelation Measurements on a Single InGaN/GaN Quantum Dot" Nanotechnology **20**, 245702 (2009). 28

[108] W. Becker, *Advanced Time-Correlated Single Photon Counting Techniques* (Springer Berlin Heidelberg, 2005). 37, 114

[109] J. Kalden, C. Tessarek, K. Sebald, S. Figge, C. Kruse, D. Hommel, and J. Gutowski, "Electroluminescence from a Single InGaN Quantum Dot in the Green Spectral Region up to 150K" Nanotechnology **21**, 015204 (2010). 39

[110] T. Jemsson, H. Machhadani, K. F. Karlsson, C. W. Hsu, and P. O. Holtz, "Linearly Polarized Single Photon Antibunching from a Site-Controlled InGaN Quantum Dot" Appl. Phys. Lett. **105**, 081901 (2014). 39

[111] S. Deshpande, A. Das, and P. Bhattacharya, "Blue Single Photon Emission up to 200 K from an InGaN Quantum Dot in AlGaN Nanowire" Appl. Phys. Lett. **102**, 161114 (2013). 51, 52

[112] S. Deshpande and P. Bhattacharya, "An Electrically Driven Quantum Dot-In-Nanowire Visible Single Photon Source Operating up to 150 K" Appl. Phys. Lett. **103**, 241117 (2013). 40

[113] C. C. Kocher, T. J. Puchtler, J. C. Jarman, T. Zhu, T. Wang, L. Nuttall, R. A. Oliver, and R. A. Taylor, "Highly Polarized Electrically Driven Single-Photon Emission from a Non-Polar InGaN Quantum Dot" Appl. Phys. Lett. **111**, 251108 (2017). 40

[114] C. H. Wang, J. R. Chen, C. H. Chiu, H. C. Kuo, Y. Li, T. C. Lu, and S. C. Wang, "Temperature-Dependent Electroluminescence Efficiency in Blue InGaN–GaN Light-Emitting Diodes with Different Well Widths" IEEE Photonic. Tech. L. **22**, 236 (2010). 42

[115] P. Perlin, M. Osiński, P. G. Eliseev, V. A. Smagley, J. Mu, M. Banas, and P. Sartori, "Low-Temperature Study of Current and Electroluminescence in InGaN/AlGaN/GaN Double-Heterostructure Blue Light-Emitting Diodes" Appl. Phys. Lett. **69**, 1680 (1996). 42, 43

[116] Sze; A. M., *Semiconductor Devices* (John Wiley & Sons, Inc., 1985). 42, 43

[117] J. M. Shah, Y.-L. Li, T. Gessmann, and E. F. Schubert, "Experimental Analysis and Theoretical Model for Anomalously High Ideality Factors in AlGaN/GaN p-n Junction Diodes" J. Appl. Phys. **94**, 2627 (2003). 43

[118] R. Koester, D. Sager, W. A. Quitsch, O. Pfingsten, A. Poloczek, S. Blumenthal, G. Keller, W. Prost, G. Bacher, and F. J. Tegude, "High-Speed GaN/GaInN Nanowire Array Light-Emitting Diode on Silicon (111)" Nano Lett. **15**, 2318 (2015). 43

[119] P. G. Eliseev, P. Perlin, J. Furioli, P. Sartori, J. Mu, and M. Osiński, "Tunneling Current and Electroluminescence in InGaN: Zn,Si/AlGaN/GaN Blue Light Emitting Diodes" J. Electron. Mater. **26**, 311 (1997). 43, 44

[120] X. A. Cao, E. B. Stokes, P. M. Sandvik, S. F. LeBoeuf, J. Kretchmer, and D. Walker, "Diffusion and Tunneling Currents in GaN/InGaN Multiple Quantum Well Light-Emitting Diodes" IEEE Electr. Device L. **23**, 535 (2002). 43

[121] T. J. Badcock, M. Ali, T. Zhu, M. Pristovsek, R. A. Oliver, and A. J. Shields, "Radiative Recombination Mechanisms in Polar and Non-Polar InGaN/GaN Quantum Well LED Structures" Appl. Phys. Lett. **109**, 151110 (2016). 44

[122] S. K. Patra and S. Schulz, "Non-Polar InGaN/GaN Quantum Dots: Impact of Dot Size and Shape Anisotropies on Excitonic and Biexcitonic Properties" J. Phys. D. Appl. Phys. **50**, 25108 (2017). 46, 49, 51, 52, 93, 94, 98

[123] S. Karpov, "ABC-Model for Interpretation of Internal Quantum Efficiency and Its Droop in III-Nitride LEDs: A Review" Opt. Quant. Electron. **47**, 1293 (2015). 47

[124] Y. Yang, X. A. Cao, and C. Yan, "Investigation of the Nonthermal Mechanism of Efficiency Rolloff in InGaN Light-Emitting Diodes" IEEE T. Electron. Dev. **55**, 1771 (2008). 47

[125] J. Cho, E. F. Schubert, and J. K. Kim, "Efficiency Droop in Light-emitting Diodes: Challenges and Countermeasures" Laser Photonics Rev. **7**, 408 (2013). 47

[126] J. E. Avron, G. Bisker, D. Gershoni, N. H. Lindner, E. A. Meirom, and R. J. Warburton, "Entanglement on Demand Through Time Reordering" Phys. Rev. Lett. **100**, 120501 (2008). 49, 129

[127] D. P. Williams, A. D. Andreev, D. A. Faux, and E. P. O'Reilly, "Surface Integral Determination of Built-in Electric Fields and Analysis of Exciton Binding Energies in Nitride-Based Quantum Dots" Physica E **21**, 358 (2004). 51

[128] J. H. Rice, J. W. Robinson, J. H. Na, K. H. Lee, R. A. Taylor, D. P. Williams, E. P. O'Reilly, A. D. Andreev, Y. Arakawa, and S. Yasin, "Biexciton and Exciton Dynamics in Single InGaN Quantum Dots" Nanotechnology **16**, 1477 (2005). 51

[129] S. Amloy, E. S. Moskalenko, M. Eriksson, K. F. Karlsson, Y. T. Chen, K. H. Chen, H. C. Hsu, C. L. Hsiao, L. C. Chen, and P. O. Holtz, "Dynamic Characteristics of the Exciton and the Biexciton in a Single InGaN Quantum Dot" Appl. Phys. Lett. **101**, 061910 (2012). 51

[130] L. Zhang, L. K. Lee, C. H. Teng, T. A. Hill, P. C. Ku, and H. Deng, "How Much Better Are InGaN/GaN Nanodisks Than Quantum Wells - Oscillator Strength Enhancement and Changes in Optical Properties" Appl. Phys. Lett. **104**, 051116 (2014). 51

[131] S. Kremling, C. Tessarek, H. Dartsch, S. Figge, S. Höfling, L. Worschech, C. Kruse, D. Hommel, and A. Forchel, "Single Photon Emission from InGaN/GaN Quantum Dots up to 50 K" Appl. Phys. Lett. **100**, 061115 (2012). 51, 103

[132] J. H. Kim, Y. H. Ko, S. H. Gong, S. M. Ko, and Y. H. Cho, "Ultrafast Single Photon Emitting Quantum Photonic Structures Based on a Nano-Obelisk" Sci. Rep. **3**, 2150 (2013). 51

[133] S. Amloy, K. H. Yu, K. F. Karlsson, R. Farivar, T. G. Andersson, and P. O. Holtz, "Size Dependent Biexciton Binding Energies in GaN Quantum Dots" Appl. Phys. Lett. **99**, 251903 (2011). 51

[134] H. Jayakumar, A. Predojević, T. Kauten, T. Huber, G. S. Solomon, and G. Weihs, "Time-Bin Entangled Photons from a Quantum Dot" Nat. Commun. **5**, 4251 (2014). 52

[135] T. Heindel, A. Thoma, M. Von Helversen, M. Schmidt, A. Schlehahn, M. Gschrey, P. Schnauber, J. H. Schulze, A. Strittmatter, J. Beyer, S. Rodt, A. Carmele, A. Knorr, and S. Reitzenstein, "A Bright Triggered Twin-Photon Source in the Solid State" Nat. Commun. **8**, 14870 (2017). 52

[136] L. Zhang, C.-H. Teng, T. A. Hill, L.-K. Lee, P.-C. Ku, and H. Deng, "Single Photon Emission from Site-Controlled InGaN/GaN Quantum Dots" Appl. Phys. Lett. **103**, 192114 (2013). 52

[137] T. J. Puchtler, T. Wang, C. X. Ren, F. Tang, R. A. Oliver, R. A. Taylor, and T. Zhu, "Ultrafast, Polarized, Single-Photon Emission from m-Plane InGaN Quantum Dots on GaN Nanowires" Nano Lett. **16**, 7779 (2016). 52, 65, 66, 67, 91, 112

[138] M. Winkelnkemper, R. Seguin, S. Rodt, A. Schliwa, L. Reißmann, A. Strittmatter, A. Hoffmann, and D. Bimberg, "Polarized Emission Lines from a - and B -Type Excitonic Complexes in Single InGaN/GaN Quantum Dots" J. Appl. Phys. **101**, 113708 (2007). 52

[139] T. J. Badcock, P. Dawson, M. J. Kappers, C. McAleese, J. L. Hollander, C. F. Johnston, D. V. Sridhara Rao, A. M. Sanchez, and C. J. Humphreys, "Optical Polarization Anisotropy of GaN/AlGaN Multiple Quantum Well Structures Grown on R-Plane Sapphire Substrates" J. Appl. Phys. **105**, 123112 (2009). 52

[140] M. Winkelnkemper, R. Seguin, S. Rodt, A. Schliwa, L. Reißmann, A. Strittmatter, A. Hoffmann, and D. Bimberg, "Polarized Emission Lines from Single InGaN/GaN Quantum Dots: Role of the Valence-Band Structure of Wurtzite Group-III Nitrides" Physica E **40**, 2217 (2008). 52

[141] T. Wang, T. J. Puchtler, S. K. Patra, T. Zhu, J. C. Jarman, R. A. Oliver, S. Schulz, and R. A. Taylor, "Deterministic Optical Polarisation in Nitride Quantum Dots at Thermoelectrically Cooled Temperatures" Sci. Rep. **7**, 12067 (2017). 53, 59

[142] M. Holmes, S. Kako, K. Choi, M. Arita, and Y. Arakawa, "Spectral Diffusion and Its Influence on the Emission Linewidths of Site-Controlled GaN Nanowire Quantum Dots" Phys. Rev. B **92**, 115447 (2015). 55, 90

[143] A. Muller, W. Fang, J. Lawall, and G. S. Solomon, "Creating Polarization-Entangled Photon Pairs from a Semiconductor Quantum Dot Using the Optical Stark Effect" Phys. Rev. Lett. **103**, 217402 (2009). 58

[144] M. Reischle, G. J. Beirne, W.-M. Schulz, M. Eichfelder, R. Rossbach, M. Jetter, and P. Michler, "Electrically Pumped Single-Photon Emission in the Visible Spectral Range up to 80 K" Opt. Express **16**, 12771 (2008). 61, 63, 64

[145] S. K. Patra, T. Wang, T. J. Puchtler, T. Zhu, R. A. Oliver, R. A. Taylor, and S. Schulz, "Theoretical and Experimental Analysis of Radiative Recombination Lifetimes in Nonpolar InGaN/GaN Quantum Dots" Phys. Status Solidi B **254**, 1600675 (2017). 61, 65, 111

[146] T. M. Babinec, B. J. M. Hausmann, M. Khan, Y. Zhang, J. R. Maze, P. R. Hemmer, and M. Lončar, "A Diamond Nanowire Single-Photon Source" Nat. Nanotechnol. **5**, 195 (2010). 64

[147] M. Belloeil, B. Gayral, and B. Daudin, "Quantum Dot-like Behavior of Compositional Fluctuations in AlGaN Nanowires" Nano Lett. **16**, 960 (2016). 65

[148] W. Götz, N. M. Johnson, C. Chen, H. Liu, C. Kuo, and W. Imler, "Activation Energies of Si Donors in GaN" Appl. Phys. Lett. **68**, 3144 (1996). 65

[149] K. P. O'Donnell and X. Chen, "Temperature Dependence of Semiconductor Band Gaps" Appl. Phys. Lett. **58**, 2924 (1991). 66

[150] M. A. Reshchikov and H. Morkoç, "Luminescence Properties of Defects in GaN" J. Appl. Phys. **97**, 61301 (2005). 66

[151] A. S. Barker and M. Ilegems, "Infrared Lattice Vibrations and Free-Electron Dispersion in GaN" Phys. Rev. B **7**, 743 (1973). 66

[152] S. V. Deshpande, "III-Nitride Based Visible Single-Photon Sources" Ph.D. thesis, University of Michigan (2015). 66

[153] A. V. Kuhlmann, J. H. Prechtel, J. Houel, A. Ludwig, D. Reuter, A. D. Wieck, and R. J. Warburton, "Transform-Limited Single Photons from a Single Quantum Dot" Nat. Commun. **6** (2015). 66

[154] I. A. Ostapenko, G. Hönig, S. Rodt, A. Schliwa, A. Hoffmann, D. Bimberg, M.-R. Dachner, M. Richter, A. Knorr, S. Kako, and Y. Arakawa, "Exciton Acoustic-Phonon Coupling in Single GaN/AlN Quantum Dots" Phys. Rev. B **85**, 81303 (2012). 66

[155] K. Gao, I. Solovev, M. Holmes, M. Arita, Y. Arakawa, K. Gao, I. Solovev, and M. Holmes, "Nanosecond-Scale Spectral Diffusion in the Single Photon Emission of a GaN Quantum Dot Nanosecond-Scale Spectral Diffusion in the Single Photon Emission of a GaN Quantum Dot" AIP Adv. **7**, 125216 (2017). 66, 90, 104, 117

[156] K. Gao, H. Springbett, T. Zhu, R. A. Oliver, Y. Arakawa, and M. J. Holmes, "Spectral Diffusion Time Scales in InGaN/GaN Quantum Dots" Appl. Phys. Lett. **114**, 112109 (2019). 66, 105, 110, 117, 118, 120

[157] A. K. Nowak, S. L. Portalupi, V. Giesz, O. Gazzano, C. Dal Savio, P. F. Braun, K. Karrai, C. Arnold, L. Lanco, I. Sagnes, A. Lemaître, and P. Senellart, "Deterministic and Electrically Tunable Bright Single-Photon Source" Nat. Commun. **5**, 3240 (2014). 68

[158] W. Unrau, D. Quandt, J. H. Schulze, T. Heindel, T. D. Germann, O. Hitzemann, A. Strittmatter, S. Reitzenstein, U. W. Pohl, and D. Bimberg, "Electrically Driven Single Photon Source Based on a Site-Controlled Quantum Dot with Self-Aligned Current Injection" Appl. Phys. Lett. **101**, 211119 (2012). 69

[159] T. Heindel, "Elektrisch Gepumpte Quantenpunkt-Einzelphotonquellen Für Die Quantenkommunikation" Ph.D. thesis, Universität Würzburg (2013). 71

[160] A. Schlehahn, A. Thoma, P. Munnelly, M. Kamp, S. Höfling, T. Heindel, C. Schneider, and S. Reitzenstein, "An Electrically Driven Cavity-Enhanced Source of Indistinguishable Photons with 61% Overall Efficiency" APL Photonics **1**, 011301 (2016). 71, 73

[161] D. J. P. Ellis, A. J. Bennett, A. J. Shields, P. Atkinson, and D. A. Ritchie, "Electrically Addressing a Single Self-Assembled Quantum Dot" Appl. Phys. Lett. **88**, 133509 (2006). 73

[162] A. J. Bennett, R. B. Patel, A. J. Shields, K. Cooper, P. Atkinson, C. A. Nicoll, and D. A. Ritchie, "Indistinguishable Photons from a Diode" Appl. Phys. Lett. **92**, 193503 (2008). 73

[163] A. C. Dada, T. S. Santana, R. N. E. Malein, A. Koutroumanis, Y. Ma, J. M. Zajac, J. Y. Lim, J. D. Song, and B. D. Gerardot, "Indistinguishable Single Photons with Real-Time-Programmable Electronic Triggering" Optica **3**, 493 (2016). 73

[164] K. A. Fischer, K. Müller, K. G. Lagoudakis, and J. Vučković, "Dynamical Modeling of Pulsed Two-Photon Interference" New J. Phys. **18**, 113053 (2018). 73

[165] F. Liu, A. J. Brash, J. O'Hara, L. M. Martins, C. L. Phillips, R. J. Coles, B. Royall, E. Clarke, C. Bentham, N. Prtljaga, I. E. Itskevich, L. R. Wilson, M. S. Skolnick, and A. M. Fox, "High Purcell Factor Generation of Indistinguishable On-Chip Single Photons" Nat. Nanotechnol. **13**, 835 (2018). 73

[166] S. K. Patra and S. Schulz, "Electrostatic Built-in Fields in Wurtzite III-N Nanostructures: Impact of Growth Plane on Second-Order Piezoelectricity" Phys. Rev. B **96**, 155307 (2017). 76, 93, 95

[167] B. D. Gerardot, S. Seidl, P. A. Dalgarno, R. J. Warburton, D. Granados, J. M. Garcia, K. Kowalik, O. Krebs, K. Karrai, A. Badolato, and P. M. Petroff, "Manipulating Exciton Fine Structure in Quantum Dots with a Lateral Electric Field" Appl. Phys. Lett. **90**, 041101 (2007). 77, 83, 84

[168] H. Gotoh, H. Kamada, H. Ando, and J. Temmyo, "Lateral Electric-Field Effects on Excitonic Photoemissions in InGaAs Quantum Disks" Appl. Phys. Lett. **76**, 867 (2000). 77

[169] W. Heller, U. Bockelmann, and G. Abstreiter, "Electric-Field Effects on Excitons in Quantum Dots" Phys. Rev. B **57**, 6270 (1998). 77, 81, 83, 84, 89, 99

[170] K. Kowalik, O. Krebs, A. Lemaître, S. Laurent, P. Senellart, P. Voisin, and J. A. Gaj, "Influence of an In-Plane Electric Field on Exciton Fine Structure in InAs-GaAs Self-Assembled Quantum Dots" Appl. Phys. Lett. **86**, 041907 (2005). 77

[171] V. Stavarache, D. Reuter, A. D. Wieck, M. Schwab, D. R. Yakovlev, R. Oulton, and M. Bayer, "Control of Quantum Dot Excitons by Lateral Electric Fields" Appl. Phys. Lett. **89**, 123105 (2006). 77

[172] M. M. Vogel, S. M. Ulrich, R. Hafenbrak, P. Michler, L. Wang, A. Rastelli, and O. G. Schmidt, "Influence of Lateral Electric Fields on Multiexcitonic Transitions and Fine Structure of Single Quantum Dots" Appl. Phys. Lett. **91**, 051904 (2007). 77

[173] G. Bacher, H. Schömig, J. Seufert, M. Rambach, A. Forchel, A. A. Maksimov, V. D. Kulakovskii, T. Passow, D. Hommel, C. R. Becker, and L. W. Molenkamp, "Optical Spectroscopy on Non-Magnetic and Semimagnetic Single Quantum Dots in External Fields" Phys. Status Solidi B **229**, 415 (2002). 77

[174] J. Seufert, M. Obert, M. Rambach, G. Bacher, A. Forchel, T. Passow, K. Leonardi, and D. Hommel, "Manipulating Single Quantum Dot States in a Lateral Electric Field" Physica E **13**, 147 (2002). 77, 89

[175] J. W. Robinson, J. H. Rice, K. H. Lee, J. H. Na, R. A. Taylor, D. G. Hasko, R. a. Oliver, M. J. Kappers, C. J. Humphreys, and G. A. D. Briggs, "Quantum-Confined Stark Effect in a Single InGaN Quantum Dot Under a Lateral Electric Field" Appl. Phys. Lett. **86**, 213103 (2005). 77, 85, 86, 89, 91

[176] Y. Zhang, M. Sun, D. Piedra, M. Azize, X. Zhang, T. Fujishima, and T. Palacios, "GaN-on-Si Vertical Schottky and p-n Diodes" IEEE Electr. Device L. **35**, 618 (2014). 78

[177] N. Tanaka, K. Hasegawa, K. Yasunishi, N. Murakami, and T. Oka, "50 a Vertical GaN Schottky Barrier Diode on a Free-Standing GaN Substrate with Blocking Voltage of 790 V" Appl. Phys. Express **8**, 71001 (2015). 78

[178] Y. Cao, R. Chu, R. Li, M. Chen, R. Chang, and B. Hughes, "High-Voltage Vertical GaN Schottky Diode Enabled by Low-Carbon Metal-Organic Chemical Vapor Deposition Growth" Appl. Phys. Lett. **108**, 62103 (2016). 78

[179] Y. Xia, Q. Li, J. Kim, W. Bao, C. Gong, S. Yang, Y. Wang, and X. Zhang, "Room-Temperature Giant Stark Effect of Single Photon Emitter in Van Der Waals Material" Nano Lett. **19**, 7100 (2019). 79

[180] J. W. Robinson, "Time-Integrated and Time-Resolved Optical Studies of InGaN Quantum Dots" Ph.D. thesis, University of Oxford (2004). 81

[181] R. Oulton, J. J. Finley, A. D. Ashmore, I. S. Gregory, D. J. Mowbray, M. S. Skolnick, M. J. Steer, S. L. Liew, M. A. Migliorato, and A. J. Cullis, "Manipulation of the Homogeneous Linewidth of an Individual In(Ga)As Quantum Dot" Phys. Rev. B - Condens. Matter Mater. Phys. **66**, 1 (2002). 81

[182] T. T. Mnatsakanov, M. E. Levinshtein, L. I. Pomortseva, S. N. Yurkov, G. S. Simin, and M. A. Khan, "Carrier Mobility Model for GaN" Solid State Electron. **47**, 111 (2003). 81

[183] A. Akkaya, L. Esmer, B. B. Kantar, H. Çetin, and E. Ayyıldız, "Effect of Thermal Annealing on Electrical and Structural Properties of Ni/Au/n-GaN Schottky Contacts" Microelectron. Eng. **130**, 62 (2014). 81

[184] P. Reddy, B. Sarkar, F. Kaess, M. Gerhold, E. Kohn, R. Collazo, and Z. Sitar, "Defect-Free Ni/GaN Schottky Barrier Behavior with High Temperature Stability" Appl. Phys. Lett. **110**, 11603 (2017). 81

[185] J. Osvald, J. Kuzmik, G. Konstantinidis, P. Lobotka, and A. Georgakilas, "Temperature Dependence of GaN Schottky Diodes I–V Characteristics" Microelectron. Eng. **81**, 181 (2005). 81

[186] A. Kumar, M. Latzel, S. Christiansen, V. Kumar, and R. Singh, "Effect of Rapid Thermal Annealing on Barrier Height and 1/f Noise of Ni/GaN Schottky Barrier Diodes" Appl. Phys. Lett. **107**, 93502 (2015). 81

[187] T. Maeda, M. Okada, M. Ueno, Y. Yamamoto, T. Kimoto, M. Horita, and J. Suda, "Temperature Dependence of Barrier Height in Ni/n-GaN Schottky Barrier Diode" Appl. Phys. Express **10**, 51002 (2017). 81

[188] S. A. Empedocles and M. G. Bawendi, "Quantum-Confined Stark Effect in Single CdSe Nanocrystallite Quantum Dots" Science **278**, 2114 (1997). 86

[189] J. Seufert, M. Obert, M. Scheibner, N. A. Gippius, G. Bacher, A. Forchel, T. Passow, K. Leonardi, and D. Hommel, "Stark Effect and Polarizability in a Single CdSe/ZnSe Quantum Dot" Appl. Phys. Lett. **79**, 1033 (2001). 86

[190] A. F. Jarjour, "Optical Studies of Single InGaN/GaN Quantum Dots" Ph.D. thesis, University of Oxford (2007). 86, 110

[191] P. Pereyra Padilla, *The WKB Approximation* (Springer Berlin Heidelberg, 2012), p. 129. 90

[192] W. Heisenberg, "Über Den Anschaulichen Inhalt Der Quantentheoretischen Kinematik Und Mechanik" Zeitschrift für Phys. **43**, 98 (1927). 90

[193] V. Bougrov, M. E. Levinshtein, S. L. Rumyantsev, and A. Zubrilov, *Properties of Advanced Semiconductor Materials GaN, AlN, InN, BN, SiC, SiGe* (John Wiley Sons, Inc., New York, 2001). 90

[194] B. Arnaudov, T. Paskova, P. P. Paskov, B. Magnusson, E. Valcheva, B. Monemar, H. Lu, W. J. Schaff, H. Amano, and I. Akasaki, "Energy Position of Near-Band-Edge Emission Spectra of InN Epitaxial Layers with Different Doping Levels" Phys. Rev. B **69**, 115216 (2004). 90

[195] K. Sebald, H. Lohmeyer, J. Gutowski, T. Yamaguchi, and D. Hommel, "Optical Properties of Single InGaN Quantum Dots up to 150 K" Phys. Status Solidi C **3**, 3864 (2006). 91

[196] R. Seguin, S. Rodt, A. Strittmatter, L. Reißmann, T. Bartel, A. Hoffmann, D. Bimberg, E. Hahn, and D. Gerthsen, "Multi-Excitonic Complexes in Single InGaN Quantum Dots" Appl. Phys. Lett. **84**, 4023 (2004). 91

[197] R. J. Warburton, C. Schulhauser, D. Haft, C. Schäflein, K. Karrai, J. M. Garcia, W. Schoenfeld, and P. M. Petroff, "Giant Permanent Dipole Moments of Excitons in Semiconductor Nanostructures" Phys. Rev. B **65**, 1 (2002). 93

[198] A. F. Jarjour, R. A. Oliver, A. Tahraoui, M. J. Kappers, C. J. Humphreys, and R. A. Taylor, "Control of the Oscillator Strength of the Exciton in a Single InGaN-GaN Quantum Dot" Phys. Rev. Lett. **99**, 197403 (2007). 93

[199] J. J. Finley, M. Sabathil, R. Oulton, A. I. Tartakovskii, D. J. Mowbray, M. S. Skolnick, S. Liew, M. Migliorato, M. Hopkinson, and P. Vogl, "Systematic Reduction of the Permanent Exciton Dipole for Charged Excitons in Individual Self-Assembled InGaAs Quantum Dots" Physica E **21**, 199 (2004). 98

[200] M. Kaniber, M. F. Huck, K. Müller, E. C. Clark, F. Troiani, M. Bichler, H. J. Krenner, and J. J. Finley, "Electrical Control of the Exciton-Biexciton Splitting in Self-Assembled InGaAs Quantum Dots" Nanotechnology **22** (2011). 98

[201] M. J. Holmes, M. Arita, and Y. Arakawa, "III-Nitride Quantum Dots As Single Photon Emitters" Semicond. Sci. Tech. **34**, 033001 (2019). 98

[202] T. Saito and Y. Arakawa, "Electronic Structure of Piezoelectric $In_{0.2}Ga_{0.8}N$ Quantum Dots in GaN Calculated Using a Tight-Binding Method" Physica E **15**, 169 (2002). 98

[203] R. Bardoux, T. Guillet, P. Lefebvre, T. Taliercio, T. Bretagnon, S. Rousset, B. Gil, and F. Semond, "Photoluminescence of Single GaN/AlN Hexagonal Quantum Dots on Si(111): Spectral Diffusion Effects" Phys. Rev. B **74**, 195319 (2006). 99

[204] W. Bak, H. Noh, C. Stambaugh, Y. Arakawa, and W. Jhe, "Spectral Fluctuations of Excitonic Transitions of InGaAs Single Quantum Dots" Appl. Phys. Lett. **100**, 022105 (2012). 99

[205] L. Besombes, K. Kheng, L. Marsal, and H. Mariette, "Few-Particle Effects in Single CdTe Quantum Dots" Phys. Rev. B **65**, 1 (2002). 100

[206] M. J. Holmes, S. Kako, K. Choi, P. Podemski, M. Arita, and Y. Arakawa, "Probing the Excitonic States of Site-Controlled GaN Nanowire Quantum Dots" Nano Lett. **15**, 1047 (2015). 100

[207] O. Ménard, F. Cayrel, E. Collard, and D. Alquier, "Ni Based Planar Schottky Diodes on Gallium Nitride (GaN) Grown on Sapphire" Phys. Status Solidi C **7**, 112 (2010). 101

[208] R. Jozsa and N. Linden, "On the Role of Entanglement in Quantum-Computational Speed-Up" P. R. Soc. London **459**, 2011 (2003). 102

[209] J. L. O'Brien, "Optical Quantum Computing" Science **318**, 1567 (2007). 102

[210] A. Aspuru-Guzik and P. Walther, "Photonic Quantum Simulators" Nat. Phys. **8**, 285 (2012). 102

[211] H.-K. Lo, M. Curty, and K. Tamaki, "Secure Quantum Key Distribution" Nat. Photonics **8**, 595 (2014). 102

[212] S. Amloy, K. F. Karlsson, M. O. Eriksson, J. Palisaitis, P. O. Å. Persson, Y. T. Chen, K. H. Chen, H. C. Hsu, C. L. Hsiao, L. C. Chen, and P. O. Holtz, "Excitons and Biexcitons in InGaN Quantum Dot like Localization Centers." Nanotechnology **25**, 495702 (2014). 103

[213] M. Arita, F. Le Roux, M. J. Holmes, S. Kako, and Y. Arakawa, "Ultraclean Single Photon Emission from a GaN Quantum Dot" Nano Lett. **17**, 2902 (2017). 103

[214] Ž. Gačević, M. Holmes, E. Chernysheva, M. Müller, A. Torres-Pardo, P. Veit, F. Bertram, J. Christen, J. M. González Calbet, Y. Arakawa, E. Calleja, and S. Lazić, "Emission of Linearly Polarized Single Photons from Quantum Dots Contained in Nonpolar, Semipolar, and Polar Sections of Pencil-like InGaN/GaN Nanowires" ACS Photonics **4**, 657 (2017). 103

[215] H. Amano, "Development of GaN-Based Blue LEDs and Metalorganic Vapor Phase Epitaxy of GaN and Related Materials" Prog. Cryst. Growth Ch. **62**, 126 (2016). 103

[216] D. Sutherland, F. Oehler, T. Zhu, J. T. Griffiths, T. J. Badcock, P. Dawson, R. M. Emery, M. J. Kappers, C. J. Humphreys, and R. A. Oliver, "An Investigation into Defect Reduction Techniques for Growth of Non-Polar GaN on Sapphire" Phys. Status Solidi C **11**, 541 (2014). 103

[217] C. Kindel, G. Callsen, S. Kako, T. Kawano, H. Oishi, G. Hönig, A. Schliwa, A. Hoffmann, and Y. Arakawa, "Spectral Diffusion in Nitride Quantum Dots: Emission Energy Dependent Linewidths Broadening Via Giant Built-in Dipole Moments" Phys. Status Solidi RRL **8**, 408 (2014). 103

[218] P. Palinginis, S. Tavenner, M. Lonergan, and H. Wang, "Spectral Hole Burning and Zero Phonon Linewidth in Semiconductor Nanocrystals" Phys. Rev. B **67**, 201307 (2003). 103

[219] X. Brokmann, M. Bawendi, L. Coolen, and J.-P. Hermier, "Photon-Correlation Fourier Spectroscopy" Opt. Express **14**, 6333 (2006). 103

[220] L. Coolen, X. Brokmann, P. Spinicelli, and J.-P. Hermier, "Emission Characterization of a Single CdSe-ZnS Nanocrystal with High Temporal and Spectral Resolution by Photon-Correlation Fourier Spectroscopy" Phys. Rev. Lett. **100**, 27403 (2008). 103

[221] A. Zumbusch, L. Fleury, R. Brown, J. Bernard, and M. Orrit, "Probing Individual Two-Level Systems in a Polymer by Correlation of Single Molecule Fluorescence" Phys. Rev. Lett. **70**, 3584 (1993). 104

[222] G. Sallen, A. Tribu, T. Aichele, R. Andre, L. Besombes, C. Bougerol, M. Richard, S. Tatarenko, K. Kheng, J.-P. P. Poizat, R. André, L. Besombes, C. Bougerol, M. Richard, S. Tatarenko, K. Kheng, and J.-P. P. Poizat, "Subnanosecond Spectral Diffusion Measurement Using Photon Correlation" Nat. Photonics **4**, 696 (2010). 104

[223] G. Hönig, G. Callsen, A. Schliwa, S. Kalinowski, C. Kindel, S. Kako, Y. Arakawa, D. Bimberg, and A. Hoffmann, "Manifestation of Unconventional Biexciton States in Quantum Dots" Nat. Commun. **5**, 5721 (2014). 105

[224] M. Häberlen, T. J. Badcock, M. A. Moram, J. L. Hollander, M. J. Kappers, P. Dawson, C. J. Humphreys, and R. A. Oliver, "Low Temperature Photoluminescence and Cathodoluminescence Studies of Nonpolar GaN Grown Using Epitaxial Lateral Overgrowth" J. Appl. Phys. **108**, 033523 (2010). 107

[225] A. M. Berhane, K. Y. Jeong, C. Bradac, M. Walsh, D. Englund, M. Toth, and I. Aharonovich, "Photophysics of GaN Single-Photon Emitters in the Visible Spectral Range" Phys. Rev. B **97**, 165202 (2018). 109

[226] C. Santori, D. Fattal, J. Vučković, G. S. Solomon, E. Waks, and Y. Yamamoto, "Submicrosecond Correlations in Photoluminescence from InAs Quantum Dots" Phys. Rev. B **69**, 205324 (2004). 110

[227] R. Brouri, A. Beveratos, J.-P. Poizat, and P. Grangier, "Photon Antibunching in the Fluorescence of Individual Color Centers in Diamond" Opt. Lett. **25**, 1294 (2000). 112

[228] A. J. Bennett, J. P. Lee, D. J. Ellis, I. Farrer, D. A. Ritchie, and A. J. Shields, "A Semiconductor Photon-Sorter" Nat. Nanotechnol. **11**, 857 (2016). 120

[229] G. Callsen, A. Carmele, G. Hönig, C. Kindel, J. Brunnmeier, M. R. Wagner, E. Stock, J. S. Reparaz, A. Schliwa, S. Reitzenstein, A. Knorr, A. Hoffmann, S. Kako, and Y. Arakawa, "Steering Photon Statistics in Single Quantum Dots: From One- to Two-Photon Emission" Phys. Rev. B **87**, 245314 (2013). 120

[230] G. Ballesteros, R. Proux, C. Bonato, and B. Gerardot, "readPTU: A Python Library to Analyse Time Tagged Time Resolved Data" J. Instrum. **14**, T06011 (2019). 122

[231] H. P. Springbett, K. Gao, J. Jarman, T. Zhu, M. Holmes, Y. Arakawa, and R. A. Oliver, "Improvement of Single Photon Emission from InGaN QDs Embedded in Porous Micropillars" Appl. Phys. Lett. **113**, 101107 (2018). 129